Title
Scalar and Spinor Excitations in a Ferromagnetic Bose-Einstein Condensate

Author
Marti, George Edward

Publication Date
2014

Peer reviewed|Thesis/dissertation

Scalar and Spinor Excitations in a Ferromagnetic Bose-Einstein Condensate

by

George Edward Marti

A dissertation submitted in partial satisfaction of the
requirements for the degree of
Doctor of Philosophy

in

Physics

in the

GRADUATE DIVISION
of the
UNIVERSITY OF CALIFORNIA, BERKELEY

Committee in charge:
Professor Dan M. Stamper-Kurn, Chair
Professor Holger Müller
Professor Tanja Ćuk

Fall 2014

Scalar and Spinor Excitations in a Ferromagnetic Bose-Einstein Condensate

Abstract

Scalar and Spinor Excitations in a Ferromagnetic
Bose-Einstein Condensate

by

George Edward Marti
Doctor of Philosophy in Physics

University of California, Berkeley

Professor Dan M. Stamper-Kurn, Chair

At low temperatures, the thermodynamic properties of a many-body system are determined by the low energy excursions from the ground state. In quantum degenerate rubidium, the low energy excitations are phonons—phase and density modes—and magnons—spin modes. This thesis reports on the construction of an ultracold rubidium apparatus and techniques to create and image phonons and magnons. We propose and study matter wave interferometry of phonons in a ring trap as a potential compact rotation sensor. Precision measurements of magnons allow us to determine the magnon dispersion relation, including a gap induced by magnetic dipole-dipole interactions.

To my family, for their unconditional support

Contents

List of Figures

Acknowledgments

When I joined the Stamper-Kurn group as an undergraduate at Berkeley, I was inspired by the first-rate researchers who, despite their busy research lives, managed to have time to answer my trivial questions, teach me how to solder properly, and chat about life from the point of view of a scientist. Deep Gupta, Mukund Vengalattore, Toni Öttl, Tom Purdy, Kevin Moore, and Lorraine Sadler were role models on how to pursue science while training younger students. I owe a debt of gratitude in particular to Kevin and Mukund, who helped with my graduate school and fellowship applications. I also owe Mukund a case of beer.

Between my undergraduate and graduate studies at Berkeley, I spent a year doing science with *puces à atomes* in Jakob Reichel's group at the Laboratoire Kastler Brossel in Paris. I found scientists who were dedicated and, true to Jakob's advertisement, had a good sense of humor. Perhaps the group's devotion to science was only matched by its obsession with coffee, a trait that I am proud to have acquired. I miss the late night dinners and afternoon espresso with Yves Colombe, Romain Long, Jürgen Volz, and fellow members of the group.

The Berkeley physics community is a wonderful place to grow as a researcher and as a graduate student. On numerous occasions, professors were very giving and lent me their time just to chat about science and life. I thank, among others, Holger Müller, Hartmut Häffner, and Hitoshi Murayama. Michael Solarz deserves special recognition for his continuous enthusiasm and willingness to build whatever last-minute parts our experiment constantly required. I cannot tell whether Anne Takizawa is an angel in disguise or simply an amazing human being, but I am forever thankful to her for helping my graduate career run smoothly.

My graduate studies were supported by the Chancellor's Fellowship and the Fannie and John Hertz Foundation Fellowship. I am particularly grateful to the Hertz Foundation for guidance and for introducing me to a phenomenal community through numerous workshops, retreats, and lunches. It is typically rare for a graduate student to gain exposure outside his or her tiny subfield, but through the Hertz community I made good friends with scientists with a diverse range of interests.

Graduate school would not have been as enjoyable as it was without all my terrific colleagues in the Stamper-Kurn group, including Kater Murch, Sabrina Leslie, Jennie Guzman, Dan Brooks, Thierry Botter, Nathan Brahms, Gyu-Boong Jo, Friedhelm Serwane, Andre Wenz, Vincent Klinkhamer, Sydney Schreppler, Claire Thomas, Nicolas Spethmann, Maryrose Barrios, Tom Barter, Jonathan Kohler, Zephy Leung, Justin Gerber, Severin Daiß, and everyone I neglected to include by name here. Jennie deserves special mention, not just because of our late night gossiping, but because it was through her experimental prowess that she taught us exactly how to get a spinor condensate experiment working. On the "E4" team, I enjoyed working many hours with Toni Öttl, who taught us how to build an experiment[1], Enrico Vogt, Andrew MacRae, Gabe Dunn, Sean Lourette, Holger Kadau, Fang Fang, and Eric Copenhaver. I have spent more hours working with Ryan Olf than with anyone else, and his constant good humor and optimism helped us get through the difficult years of experimental frustration. I am proud that we finally got to do science with our machine.

[1]The secret is brass, epoxy, elbow grease, and good coffee.

Of course, I owe Dan Stamper-Kurn singularly special recognition for making an indelible mark on my development as a scientist. While I may never achieve his deep insight or keep pace with his expectations, he has taught me to question my claims and keep true to the spirit that science is curiosity mixed with skepticism.

Most of all, I would like to thank Misa Sugino, my constant companion for all the years in Berkeley. Through the frustration of graduate school, the late nights in lab, the unreasonable time spent writing this thesis, and the countless times I was late to everything, she supported and encouraged me.

Chapter 1

Introduction

My doctoral project's initial purpose was to explore trapped atom interferometry by improving on the magnetic ring trap developed in Gupta, *et al.* [1]. In an ideal realization, the ring would serve as an unterminated waveguide in which atoms could coherently propagate "forever." However, the ring trap demonstrated in Gupta, *et al.* had large angular perturbations that would have compromised its application in atom interferometry.

Our experiment was intended as a 'second generation' machine that would use ultracold lithium and a microfabricated magnetic ring trap. We expected that the microfabricated trap would produce smoother potentials and that lithium, because of its relatively low mass and high recoil energy, would be less sensitive to remaining imperfections of the potential. However, even after a monumental effort by Tom Purdy and Ryan Olf, we were unable to produce a sufficient number of samples of the new trap (Fig. 1.1).

Compounding our problems, a critical issue arose with the magnetic transport system that conveyed atoms to the ring trap. The transport had to guide atoms through a 9 mm gap in a holding arm designed to support the microfabricated ring trap. Unfortunately, the transport was misaligned with, and crashed atoms into, the holding arm.

With too few microfabricated samples and a transport system that needed to be redesigned, we decided to abandon the original plan. Without the trap, we had no clear way to create a quantum degenerate gas. For a backup plan, I purchased a far too cheap 1.5 W, 532 nm laser that we hoped could produce an optically plugged Bose-Einstein condensate (BEC) [2]. The poor spatial mode and low power of the laser jeopardized that attempt. Ultimately, we implemented a hybrid trap that combined a magnetic trap and an attractive light potential and finally allowed us to create a BEC [3]. While most of our experimental setup is similar to many others, I focus on new or interesting aspects of our apparatus in Ch. 2.

In search of an alternative idea, we built a bichromatic optical ring trap as a substitute for the magnetic ring trap for which we had long hoped. It was far easier to implement this bichromatic optical trap, with an attractive light potential to pull atoms into a disk and a repulsive light potential to push atoms away from the core, than to implement the aforementioned microfabricated trap. Experiments with phonon interferometry are described in Ch. 3.

One side project with the optical ring trap involved rotating atoms by dynamically

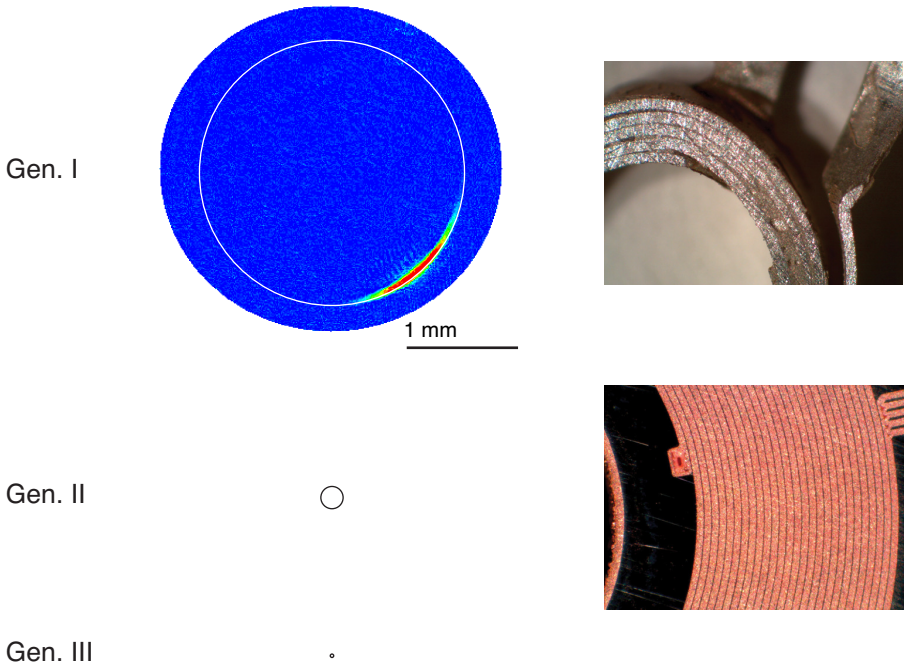

Figure 1.1: Three generations of ring traps. Gen. I refers to the original circular waveguide used in [1] with a 1 mm radius. Our plan was to develop a second generation experiment with much smoother current carrying wires and reduce the radius to 100 μm. Photos on the right show an edge of the current carrying structures. The ring trap implemented in this thesis was all-optical and tiny, with a 16 μm radius.

deforming the magnetic field (Sec. 3.6). In the process of testing this idea, we created a spin vortex as demonstrated in Ref. 4 and began to think about spinor physics. Spinors are a topic with which the Stamper-Kurn group has a great of deal experience; we were able to get this spinor setup up and running quickly, largely by doing exactly what Jennie Guzman told us to do [5]. Our main innovation with this spinor machine was to develop a new imaging technique that allowed us to take high signal-to-noise images of the spin density. Experimental details for our spinor setup are discussed in Ch. 4.

I find clean and simple experiments compelling, and spinor condensates afford many such possibilities. While looking for new physics with spinor condensates, we realized that magnons, the simplest magnetic excitations, had never been measured in a spinor condensate. [1] We decided to measure the dispersion relation and other properties of magnons. The experiment was simple and immediately yielded excellent agreement with theory. As happens in these situations, we found ourselves measuring more and more carefully until we reached a precision that finally disagreed with theory. It remains to be seen whether the fault is with theory or with a subtle experimental error. This adventure is discussed in Ch. 5.

[1] This point was brought up by Hitoshi Murayama who was then thinking about the number and type of gapless excitations that can be found in systems with multiply broken symmetry, like a spinor condensate [6].

Chapter 2

Experimental Apparatus

2.1 Overview

The bulk of the experimental apparatus (Fig. 2.1) is devoted to bringing rubidium atoms to quantum degeneracy along the circuitous path shown in Fig. 2.2. Each experimental cycle requires 20-40 seconds to cool atoms from above room temperature to below a microkelvin through a combination of laser cooling and forced evaporative cooling. These details are well described in a number of previous publications, most notably Ref. 7 for laser cooling, magnetic trapping, and evaporative cooling, and Ref. 3 for optical trapping, evaporative cooling in an optical trap, and oven design. In addition, the optical lattice experiment at Berkeley was built in parallel with ours and shares many details [5].

All alkali atom BEC experiments use a magneto-optical trap (MOT) to rapidly collect and cool atoms from a slow source[1]. We use a Zeeman slower designed to slow rubid-

[1]Exceptions in other systems include atomic hydrogen [8], metastable helium [9], and solid-state BECs

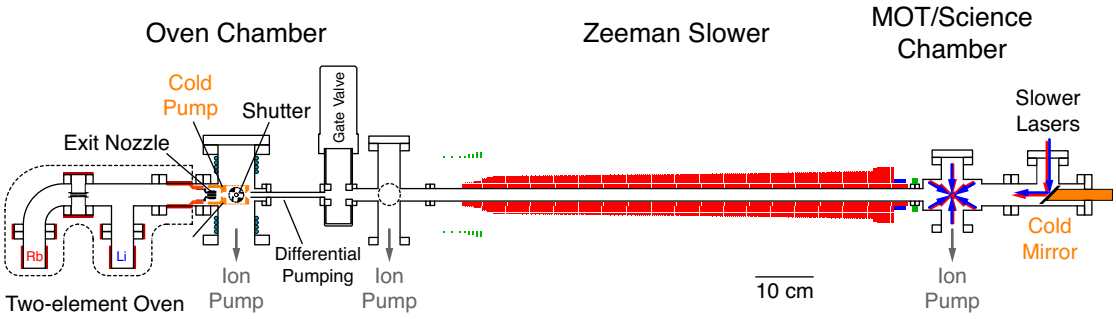

Figure 2.1: Schematic of the vacuum chamber. Simultaneous atomic beams of rubidium and lithium are generated from the diffusive oven through a common nozzle (left). The beam passes through a differential pumping section and enters the Zeeman slower, where it is slowed by scattering photons from lasers that oppose the atomic beam. Slow atomic beams exit the Zeeman slower and are captured by the MOT. The atoms are evaporatively cooled in a magnetic and then optical trap to reach quantum degeneracy. The schematic is to scale, including each individual winding of the Zeeman slower.

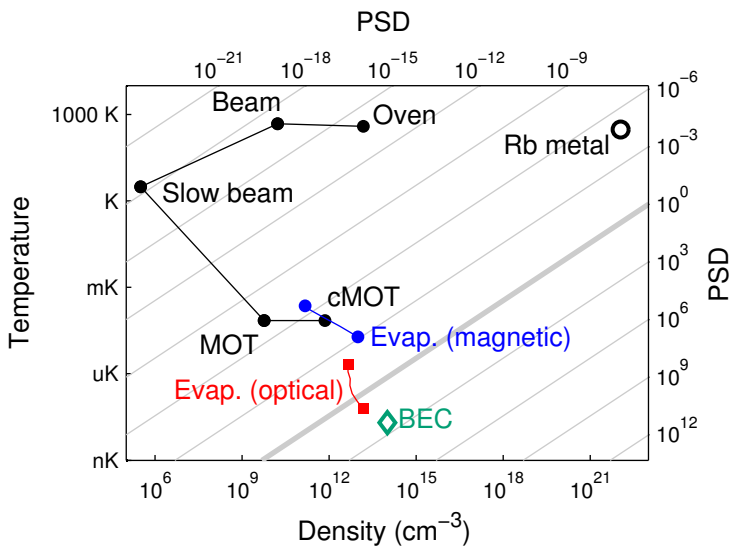

Figure 2.2: Atoms are cooled to quantum degeneracy by a circuitous path through phase space. Calculated phase space densities assume an ideal gas; they are incorrect for the rubidium metal (open black circle) and BEC (open green diamond). Beam refers to the atomic beam immediately in front of the nozzle. The phase space values in the optical trap were for marginal conditions in our original setup.

ium and lithium simultaneously [10] as a source of slow atoms for the MOT. Once we have collected atoms in the MOT and compressed it, we trap the atoms in a magnetic spherical quadrupole trap and begin forced evaporation [7]. Microwaves tuned near the 6.8 GHz hyperfine frequency of rubidium remove the hottest atoms and cool the magnetically trapped sample through forced evaporation. At a phase space density of 10^{-3}, atoms are captured by an optical dipole trap [3, 5] and continue to evaporate to create a Bose-Einstein condensate (BEC).

2.2 Diffusive Oven

Before we can laser cool the atoms, we must introduce them to the UHV chamber. Some care must be taken when combining a bright source of high vapor pressure atoms, like rubidium, with the stringent low-pressure requirements of an ultracold atom experiment. Like many other experiments, our solution is to use a relatively high pressure diffusive oven to emit a beam of alkali atoms, slow them with a Zeeman slower, and capture them in a magneto-optical trap (MOT). This solution allows us to physically separate the high pressure region, with 10^{-3} torr of rubidium, from the $<10^{-11}$ torr science chamber.

The two-element diffusive oven is based on a design on the MIT sodium-lithium oven [11, 12]. In general, we want a density of around 10^{13} cm^{-3} (3–5 $\times$ 10^{-4} torr) in the oven to generate a bright atomic beam. The chief design challenge is that rubidium and lithium reach this vapor pressure at very different temperatures, 115°C and 450°C respectively. Our design separates the oven into a lower temperature rubidium chamber

that feeds into a higher temperature lithium chamber, where the two elements mix and exit through the same nozzle. Details can be found in Ryan Olf's thesis.

2.2.1 Nozzle

We generate bright, collimated beams of rubidium—and occasionally lithium—with a diffusive oven and nozzle. A reservoir is heated to create a substantial pressure of the alkali atoms. A small fraction of the atoms leave as an atomic beam when they reach the nozzle, a series of small tubes at the end of the oven. While most of these details are well documented in the literature [11, 13, 3, 14], the geometry and flux is an important design parameter and our use of a bundle of nozzles is slightly different from previous groups.

The dynamics of gas flowing through a chamber depends on whether a particle is more likely to encounter another particle or a wall of the vessel. The two limiting cases are the molecular flow regime, where the mean free path is greater than the size of the chamber, and viscous flow, where the mean free path is smaller than the size of the chamber. The flow in the UHV chamber is well within the molecular flow regime. In the diffusive oven, the mean free path is about a centimeter and therefore in the viscous regime, but the nozzle itself is small enough that molecular flow estimates are valid.

The conductance and flux of an atomic beam through a bundle of small tubes, like we use, is the same as for a single tube with the same open area and aspect ratio. The exception is that the smaller tubes can be operated at a higher pressure before flux diminishes: the flux is proportional to density until the mean free path is on the same order as the length of the tube, which occurs at a higher density for shorter tubes.

To estimate the beam flux, we need to know the phase-space density of a classical, ideal gas with number density n_0, mass m, and temperature T (k_B is the Boltzmann constant).

$$n(\vec{x},\vec{p}) = n_0 \left(\frac{1}{2\pi m k_B T}\right)^{3/2} e^{-|\vec{p}|^2/2mk_BT}$$

The number of atoms exiting through a tube (length L, radius r, area $A = \pi r^2$, and half-angle $\theta_{\text{nozzle}} = r/L$) in a time t for a momentum class $\vec{p}$ is proportional to the number of atoms in the volume a distance $|p|t/m$ of the aperture. A little geometry shows this volume is $(A|p|t/m)\cos\theta$, where θ is the angle between the tube axis and $\vec{p}$.

$$\begin{aligned}
N &= \int d\vec{p}\, d\vec{x}\; H(|\vec{p}\,t/m - \vec{x}|)\, n(\vec{x},\vec{p}) \\
&= \int_0^\infty p^2\, dp \int_0^{\theta_{\text{nozzle}}} d\theta \int_0^{2\pi} d\phi\, n_0 \left(A\cos\theta\,\frac{pt}{m}\right)\left(\frac{1}{2\pi m k_B T}\right)^{3/2} e^{-p^2/2mk_BT} \\
&= n_0 A \sqrt{\frac{k_B T}{2\pi m}}(1-\cos\theta_{\text{nozzle}}) \\
&\approx \frac{1}{8} n_0 A t \bar{v}\, \theta^2_{\text{nozzle}} \qquad\qquad \bar{v} = \sqrt{\frac{8k_BT}{\pi m}}
\end{aligned}$$

H is the step function. It is common to define the conductance as $C = \dot{N}/n_0$, with units of volume per time, which does not depend on the particle density in the molecular flow

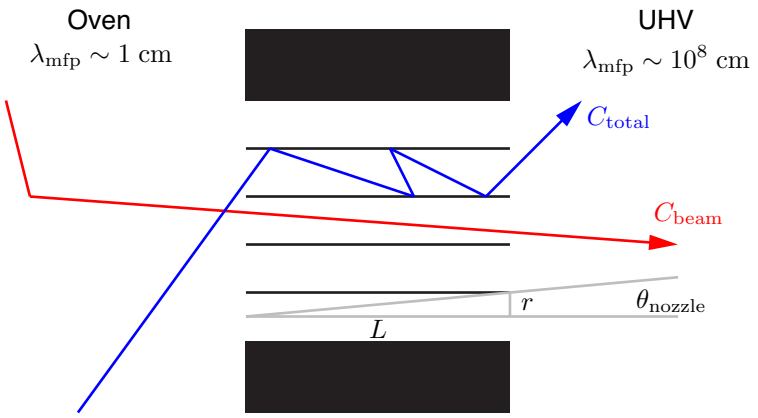

Figure 2.3: Schematic of flow through the diffusive oven nozzle. Atoms that pass through the nozzle without touching the walls form a tightly collimated beam with flux $C_{\mathrm{beam}} n_0$. Most atoms that leave the nozzle do so after multiple bounces on the wall. The flux C_{total} is higher, but the flux is less directed. These two conductances are limiting case of the true angular distribution function of the beam.

regime [15].

$$C_{\mathrm{beam}} = \frac{1}{8} A \bar{v}\, \theta_{\mathrm{nozzle}}^2 \tag{2.1}$$

The conductance towards the MOT, $C_{\mathrm{MOT}} = A\bar{v}\theta_{\mathrm{MOT}}^2/8$, depends on the half-angle θ_{MOT}. For many tubes in parallel, the conductances add and we can treat A as the total area of the nozzle, summed over the individual tubes.

The total flux through the nozzle must include trajectories where atoms make multiple bounces (see Fig. 2.3). Fortunately, a calculation of the flux in this regime has been conducted for several geometries, including long cylindrical tubes [15]. For N_{tubes} tubes with total area $A = N_{\mathrm{tubes}}\pi r^2$,

$$C_{\mathrm{total}} = N_{\mathrm{tubes}} \frac{2\pi r^3}{3L} \bar{v} \approx \frac{2}{3} A \bar{v}\, \theta_{\mathrm{nozzle}} \tag{2.2}$$

This type of flow scales rather differently than the flux in the beam we calculated above: the conductance scales with $A^{3/2}$ (for fixed length) or θ_{nozzle} (for fixed area).

Armed with these formulae, we can make a few statements about the desired design of the nozzle. We might expect that, for fixed nozzle area, we want to have a highly collimated beam by keeping θ_{nozzle} small. In fact, the fraction of the flux in the beam *decreases* as we more tightly collimate the beam as $C_{\mathrm{beam}}/C_{\mathrm{total}} \sim \theta_{\mathrm{nozzle}}$. However, the fraction of atoms headed towards the MOT, $C_{\mathrm{MOT}}/C_{\mathrm{total}} \sim \theta_{\mathrm{MOT}}^2/\theta_{\mathrm{nozzle}}$, *increases* with a tighter collimation as long as $\theta_{\mathrm{nozzle}} > \theta_{\mathrm{MOT}}$. As common sense suggests, we want to keep θ_{nozzle} small but still larger than θ_{MOT}. If $\theta_{\mathrm{nozzle}} < \theta_{\mathrm{MOT}}$, the fraction of atoms headed towards the MOT decreases and the oven becomes less efficient.

Initially, we loaded the oven with rubidium and lithium and used a nozzle consisting of hundreds of tubes with an inner diameter of 160 μm. With this setup, we operated simultaneous ^{87}Rb and ^{7}Li MOTs [10]. For the experiments described in Ch. 3–5, we instead used an oven loaded with only rubidium and a nozzle of 14 tubes with $r = 0.5$ mm, $L = 1$ cm,

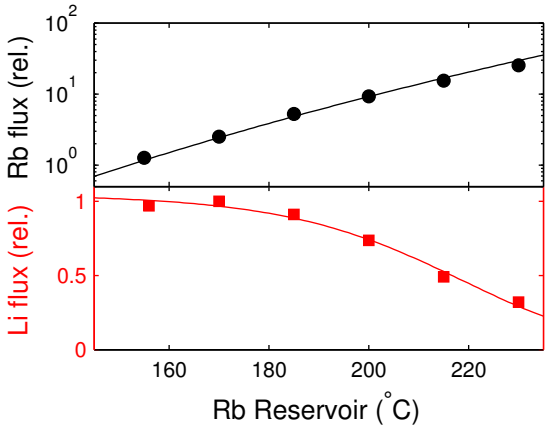

Figure 2.4: Depletion of the lithium atomic beam by rubidium. (top) The rubidium beam flux greatly increases with reservoir temperature, as measured by fluorescence of the atomic beam in the MOT chamber. At high rubidium density, collisions in the nozzle reduce the forward flux once the mean free path approaches the nozzle length. The solid line is proportional to the vapor pressure of rubidium. (bottom) The lithium flux, as measured by the relative MOT loading rate, decreases for increasing rubidium pressure above 180°C. The line is a guide to the eye. The lithium density and reservoir temperature are held constant.

and $A = 10$ mm^2 at a temperature of 200°C. This geometry should have a collimation of $\theta_{\mathrm{MOT}} = 1/100$ and $\theta_{\mathrm{nozzle}} = 1/20$. We expect $C_{\mathrm{beam}} = 10^{-3}$ L/s, $C_{\mathrm{MOT}} = 4 \times 10^{-5}$ L/s, and $C_{\mathrm{total}} = 10^{-1}$ L/s. We operate the rubidium reservoir at 115°C at an expected density of 10^{13} cm^{-3} [16]. The flux should be 4×10^{11} s^{-1} towards the MOT and 10^{15} s^{-1} in total, with a lifetime of 1 year of continuous operation for a 5 g ampoule of rubidium. These calculations are consistent with our experience.

At higher pressures, the nozzle is no longer in the molecular flow regime. Assuming a rubidium-rubidium cross section of $\sigma = 14 \times 10^{-14}$ cm^2 at room temperature [17, 18], the mean free path is $\lambda_{\mathrm{mfp}} = (n\sigma)^{-1} \approx 1$ cm is on the order of the length of the tube. For higher pressures, when $r < \lambda_{\mathrm{mfp}} < L$, we enter the Knudsen regime where flow is between the usual molecular and viscous flow limits. A rough estimate is that the effective length of the nozzle is reduced to λ_{mfp} and collimation to $\theta_{\mathrm{nozzle}} = r/\lambda_{\mathrm{mfp}}$. Thus we expect diminishing returns when increasing the reservoir temperature. The effect is particularly problematic in the rubidium and lithium oven, where we observe a decrease in lithium flux for increasing rubidium density (Fig. 2.4).

2.2.2 Differential Pumping

The two-element oven suffered from high pressures of hydrogen, most likely due to hydrogen dissolved in the lithium [19]. In our original design, the high load of hydrogen from the oven increased the main chamber pressure. We added a differential pumping stage (shown in Fig. 2.5) to decrease the pressure of hydrogen.

Differential pumping works by restricting the flow between two chamber and aggressively pumping the lower pressure side. For a restriction with conductance C_{tube} and

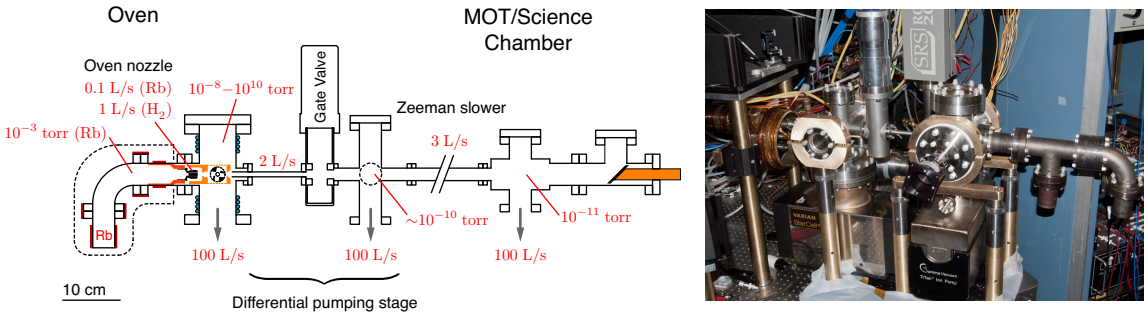

Figure 2.5: Estimated conductance and pressures. Unless otherwise noted, conductance, pumping speed, and pressures are for hydrogen. Not listed is the enormous pumping speed of the cold surfaces for rubidium (orange). For more details, see the complete diagram in Fig. 2.1. (Right) The two-element oven and differential pumping stage with a glimpse of the Zeeman slower to the left.

pumping speed C_{pump}, the ratio of pressures between the two chambers is $C_{\text{tube}}/C_{\text{pump}}$, where we assume the entire gas load originates in the first chamber and $C_{\text{tube}} \gg C_{\text{pump}}$. For instance, between the oven and the Zeeman slower, we added a tube with a 5 mm radius and 130 mm length, which has an estimated conductance of 3 L/s for hydrogen, and an ion pump with approximately 100 L/s pumping speed for hydrogen. We would expect that the pressures of the two chambers has a ratio of 30. By repeating this scheme with three constrictions with three pumps, we can maintain a very low pressure for the science chamber even with a rough vacuum in the oven.

2.2.3 Cold catcher

Nearly all ($1 - C_{\text{beam}}/C_{\text{total}} \approx 99\%$) of the rubidium emitted by the nozzle exits at large angles. Over the course of several years, several grams of rubidium flow into the oven chamber. We pump the rubidium with a cold surface, a contraption of aluminum and copper that we cool to below $-10°$C. The low temperatures reduces the rubidium partial pressure from 3×10^{-7} torr at room temperature to below 10^{-8} torr [16]. The lower pressure allows the ion pump to last longer. Regardless, we find that the ion pump is damaged by rubidium over a couple years of operation.

Once the oven inevitably runs out of rubidium, one must take care opening the chamber to atmosphere with a large quantity of rubidium present. Humidity causes the rubidium to melt and potentially catch on fire. After several designs, we settled on a cold catcher assembly with a removable cup (Fig. 2.6), inspired by the cavity QED experiment [20]. The cup surrounds the nozzle and captures nearly all of the rubidium. Four grooves on the front of the cup allow us to unscrew the cup and immediately place it in mineral oil before a fire can start. The rest of the chamber is coated in a thin layer of rubidium that can be removed by spraying it with methanol.

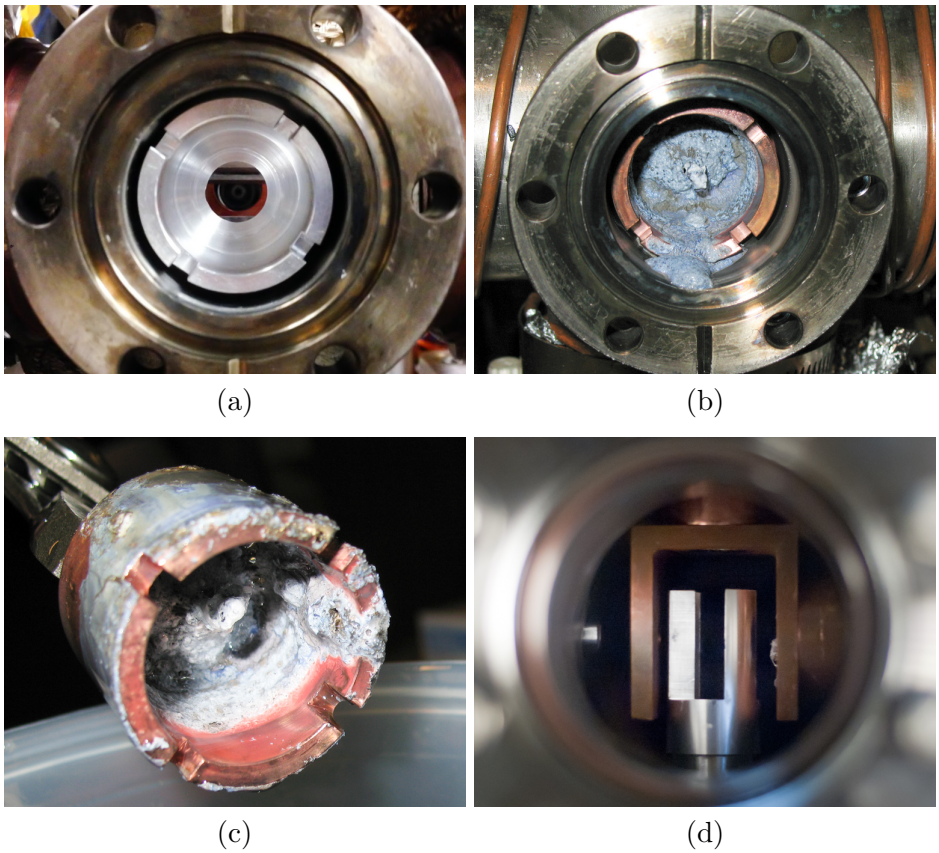

Figure 2.6: Cold catcher cup, (a) empty and (b-c) very full. Most of the rubidium atoms (>99%) that leave the oven sticks to this cup. It can be removed by unscrewing it with a tool that slips into the four grooves around the cup. When exposed to air, the rubidium changes color, heats up, and flows, which makes the cold catcher cup runneth over. (d) The shutter assembly seen from the top. The cold catcher cup is visible to the right.

2.3 Two-element Zeeman slower

The MOT is incredibly efficient at capturing a dilute source of ∼1 K temperature atoms and producing a dense, sub-millikelvin ensemble. The purpose of the Zeeman slower is to reduce the speed of the hot atomic beam, with a mean speed of around 300 m/s, to below the 30 m/s capture velocity of the MOT. A good discussion of Zeeman slowers can be found in Ref. 21, 22, 23. The design parameters for our slower can be found in Ryan Olf's thesis and Ref. 10. The following discussion will briefly introduce the main concepts and present data characterizing our slower.

Atoms are slowed by spontaneously scattering light from an opposing laser. For each scattering event, an atom changes its momentum by $\hbar k$ ($k = \omega/c$ is the laser wavenumber) when it absorbs a photon from the laser, and has no net momentum change when it spontaneously emits the photon in a random direction. However, an atom's random reemission of light causes transverse heating and the atomic beam to bloom.

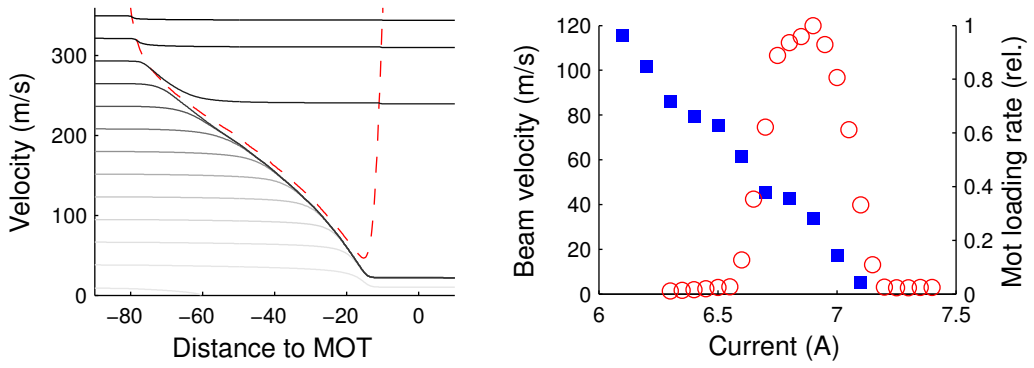

Figure 2.7: Simulated and measured atomic beam velocity. (a) Simulations of the classical trajectory of the forward beam velocity with position (black lines). Fainter lines represent lower relative flux. The red dashed line marks the resonant velocity in Eq. 2.4. Without heating, the atomic trajectories are compressed to a few linewidths below the resonant velocity (Eq. 2.4). (b) Measured beam velocities and MOT loading rate as a function of slower current. The peak magnetic field B_{peak} increases with current, which decreases the final velocity. When the beam velocity falls below 60 m/s, the MOT loading rate abrurptly increases. The slower laser detuning is fixed at -900 MHz.

The maximum deceleration occurs when an atom reduces its velocity by $\hbar k/m$ per scattering event at the maximum scatterings rate $\Gamma/2$ ($\Gamma = 2\pi \times 6$ MHz is the atomic linewidth for rubidium and lithium).

$$a_{\max} = \frac{\hbar k \Gamma}{2m} \approx \begin{cases} 10^5 \text{ m/s}^2 & {}^{87}\text{Rb} \\ 10^6 \text{ m/s}^2 & {}^{7}\text{Li} \end{cases} \tag{2.3}$$

To maintain the maximum scattering rate at modest laser powers, an atom must remain close to atomic resonance. A deceleration of only $\Gamma/k \approx 5$ m/s will Doppler shift an atom by a linewidth, far less than the ∼300 m/s needed to decelerate a large fraction of the rubidium beam. The Zeeman slower solves this problem by countering the decreasing Doppler frequency with an increasing Zeeman shift through a position-dependent magnetic field. An atom is resonant with the laser (detuning Δ from atomic resonance, with $\Delta < 0$) when it satisfies $\Delta = \mu B(x) + kv$, where $\mu = \mu_B$ is the magnetic moment difference between the ground and optically excited states. Rewriting this, at each position in the slower, there is a resonant velocity.

$$v_{\text{res}} = \frac{\Delta - \mu B(x)}{k} \tag{2.4}$$

In our slower, the magnetic field ramps from approximately 400 G to 600 G over 60 cm to reduce the rubidium velocity by 200 m/s.

From the above description, it may appear that a slower needs precise tuning, since the changing Doppler shift needs to match the magnetic field profile. In reality, the slower is self-correcting and robust. If the magnetic field gradient is a little larger or smaller than expected, then the local velocity will follow Eq. 2.4. If an atom is faster than average

(for its position), it will be closer to resonance and experience a stronger opposing force. Simulated trajectories and final beam velocities are shown in Fig. 2.7.

Even with small errors, the final velocity is approximately $v_{\text{final}} = (\Delta + \mu B_{\text{peak}})/k$, as long as the deviations are not too sudden. If we assume that the atoms have a velocity offset from Eq. 2.4, then the acceleration $(\mu/k)\, dB/dx$ must remain below $a_{\max}$ from Eq. 2.3. Ryan Olf designed the slower to be wound with 16 layers of thin wire to prevent jumps in dB/dx and maintain a acceleration of approximately $0.7a_{\max}$. A higher acceleration is desirable because of the higher capture velocity and less transverse blooming. Further details of the slower, and its performance with simultaneously slowing rubidium and lithium, can be found in Ref. 10.

2.4 MOT/Science chamber

A slow atomic beam from the Zeeman slower is captured in the MOT, transferred to a conservative trap, and cooled through forced evaporation. All of these steps occur in overlapping traps in the middle of the MOT/Science chamber (Fig. 2.8). Much of the infrastructure serves to diagnose or assist in the production of the BEC as well as for manipulation and "science" stage of the experiment. For instance, the same bias and gradient coils are used for the whole experiment, though we switch from high-current current sources during evaporation to low-noise laser current sources for experiments with spinors. The microwave antenna used for forced evaporation is also used for microwave dressing and coherent manipulation of the condensate, and the low magnification side imaging system for diagnosing the evaporation profile also counts the condensate number.

2.4.1 Magnetic trap

The spherical quadrupole magnetic field is generated with a pair of coils (Fig. 2.8). These coils are used to power the MOT, magnetic trap, and gradient cancellation for spinor condensates (Sec. 4.4.2).

The compressed MOT stage and transfer to the magnetic trap are very similar to Ref. 7. After compression, the magnetic field gradient ramps down while the lasers optically pump the atoms to the $F = 1$ states. We then block all the lasers and jump the magnetic field gradient to 40 G/cm in 1 ms, slightly greater than the 30 G/cm needed to confine atoms against gravity. The gradient is ramped to its maximum value of 175 G/cm over 2 seconds to adiabatically compress the gas and increase the collision rate. At a steady state gradient of 175 G/cm, the water-cooled coils reach a temperature of 50°C, well within safe operating conditions.

2.4.2 Microwaves and evaporation

Many of the tricks we play with rubidium involve shuffling the internal state between the ground state $F = 1$ and $F = 2$ hyperfine manifolds. For instance, atoms in a particular $F = 1$ spin state can be removed or imaged by transferring them to $F = 2$ with a brief pulse of microwaves (Sec. 4.2.3). During magnetic trapping, we evaporatively cool the sample with microwaves to remove the hottest atoms.

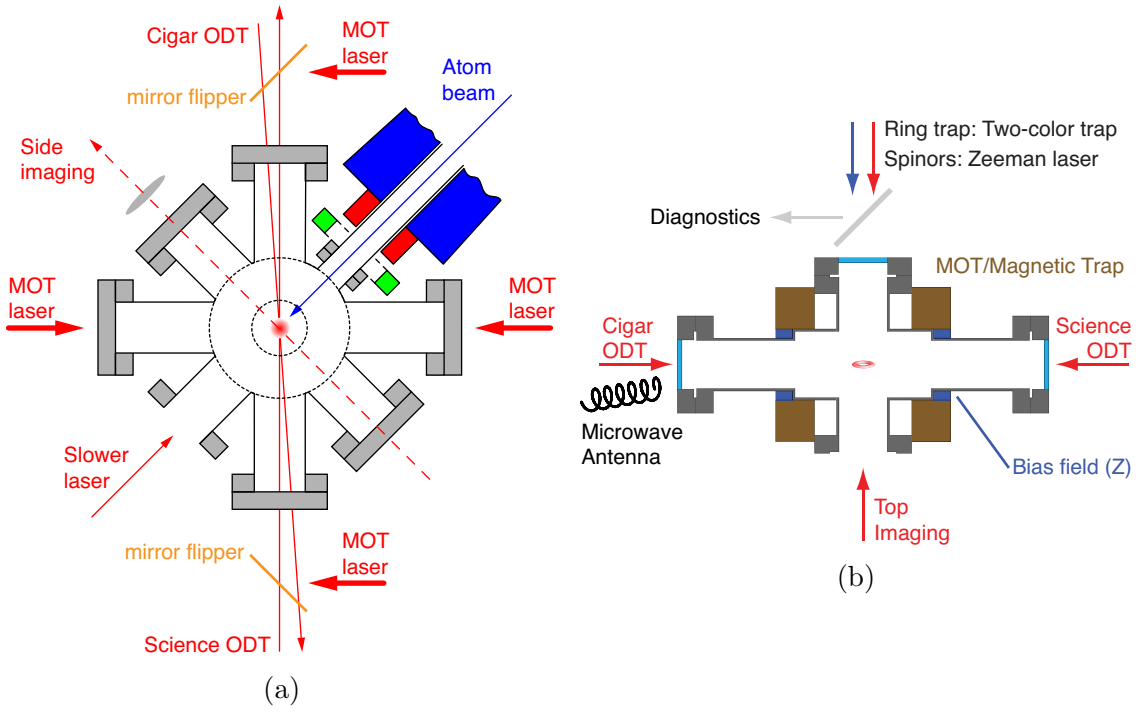

Figure 2.8: MOT/Science chamber layout. (a) Top view shows the four MOT lasers and optical dipole traps (ODT). The mirror flippers reflect the MOT lasers during the beginning of the sequence and move out of the way once the atoms are magnetically trapped. (b) Side view shows the microwave antenna and vertical optics. Not shown are the vertical MOT lasers.

Forced evaporation works by removing those atoms with several times the average energy. Since each lost atom carries a disproportionate amount of energy, their loss cools the remaining atoms. Typically our evaporation process works by removing atoms with an energy $\eta k_B T$, where $\eta = 6 - 10$.

In the magnetic trap, atoms are magnetically trapped in the $|F = 1, m_F = -1\rangle$ hyperfine state. Detuned microwaves on the $|F = 1, m_F = -1\rangle \rightarrow |F = 2, m_F = -2\rangle$ transition selectively eject atoms on the edge of the trap. For a detuning $\Delta < 0$, atoms with a potential energy $E = \hbar|\Delta|/3$ are removed[2]. Over 11 seconds, microwaves are swept from a detuning of 115 MHz to 20 MHz from the zero-field splitting (6.835 GHz), which removes atoms with a potential energy of $\hbar\Delta/(3k_B) = 1.8$ mK to 320 μK. During this ramp the gas is cooled from its initial temperature of 300 μK to 40 μK, with a final η of 8.

The microwaves for this ramp are generated by mixing a frequency-swept RF source with a 7.000 GHz dielectric resonantor (DRO). The resulting frequency is amplified by a 40 dB microwave amplifier capable of an output power of 3 W. As discussed in Sec. 4.3.1, the microwaves are too noisy for coherent manipulation but sufficient for evaporative cooling. For coherent manipulation, a switch connects a low noise signal generator to the amplifier.

[2]The final state $|F = 2, m_F = -2\rangle$ has twice the magnetic moment and a potential energy $-2E$, hence the factor of 3

The microwave antenna is a helical antenna with six turns. We wind the antenna with a circumference of λ and a spacing of $\lambda/4$ between the turns, where $\lambda = c/(6.8\text{ GHz}) = 4.4$ cm. There is a large copper backplate placed $\lambda/8$ from the first winding, which acts like a mirror and doubles the effective length. The antenna was constructed by our machinist, Michael Solarz, who tightly wound the coil around a bar of the appropriate radius. We extended the length of the by coil by hand while monitoring the transmitted power with a half-wave dipole antenna.

The antenna is placed 40 cm from the atoms because of space constraints. The power at the atoms is acceptable but not huge, reaching a peak Rabi frequency of 4.7 kHz on the $|F = 1, m_F = 0\rangle \rightarrow |F = 2, m_F = 0\rangle$ transition (Fig. 4.13).

2.4.3 Optical Dipole Trap

Our first BEC was trapped with an 830 nm optical dipole trap (ODT) with a marginal amount of optical power. When we upgraded to a much more powerful 1064 nm fiber laser, we decided to use two optical traps. First, we loaded a "cooling" trap (50 μm waist, up to 9 W of power) from the magnetic trap. This trap evaporatively cooled the gas to just above the critical condensation temperature. Then, atoms are transferred to a "science" trap, with an adjustable trap geometry (Fig. 2.8). For most experiments in this thesis, the science trap was a surfboard potential with a focus of 10 μm against gravity and 400 μm transverse to gravity.

The two paths for the cigar and side laser go through tandem AOMs. The cigar trap is derived from the +1 order of an AOM. The 0 order travels through a second AOM, that diffracts the -1 order towards a fiber coupler for the science trap. As we decrease the power to the cigar trap during optical evaporation, we increase the power in the science trap. The two traps must be aligned within approximately 30 μm. Typically this alignment remains stable for many months.

The optical trapping lasers have up to several watts of power and need to be sent into a beam dump. A small fraction of the light is measured with a photodiode either immediately before or after the atoms. The photodiode current is stabilized with a home-built PI loop to control the intensity during evaporation ramps and reduce noise in the trapping light. For the science trap, we reached lifetimes greater than 40 seconds with a Hamamatsu S11499 photodiode and an SR570 current preamplifier. The Hamamatsu photodiode has comparatively good responsivity at 1064 nm with low capacitance.

2.5 Laser cooling optics

To cool and image the atoms, we need five frequencies as shown in Fig. 2.9. All rubidium cooling light is referenced to a single master laser, originally an external cavity diode laser (Newfocus Vortex) but more recently replaced with a much more stable distributed feedback laser (Eagleyard). That laser is electronically locked to a rubidium vapor cell with FM saturation absorption spectroscopy, similar to a Pound-Drever-Hall lock. For convenience, the laser is locked to a crossover peak exactly halfway between the $F = 2 \rightarrow F' = 1$ and $F = 2 \rightarrow F' = 3$ transitions. Two additional lasers, for the slower and repump, are

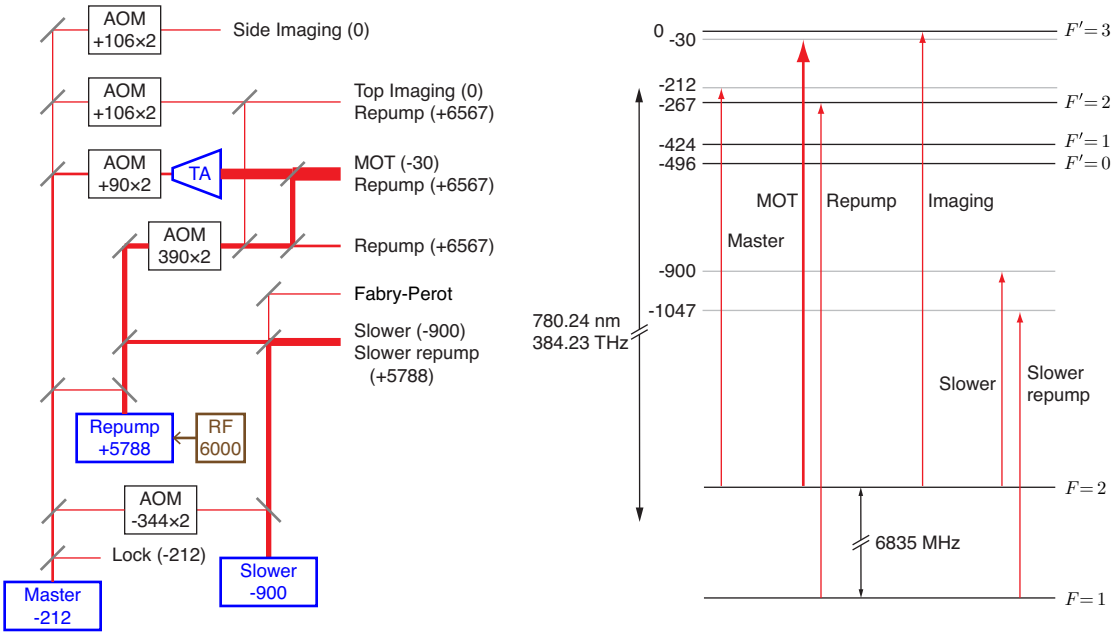

Figure 2.9: Laser scheme for cooling and imaging rubidium. (left) Blue boxes are lasers, the number indicates the detuning from the D2, $|F = 2\rangle \rightarrow |F' = 3\rangle$ transition. The master laser is a distributed Bragg reflector (formerly an external cavity diode laser), locked to an atomic resonance with electronic feedback to saturation absorption spectroscopy. The repump and slower lasers injection-locked free-running diodes lasers with no external cavity. Acousto-optic modulators (AOMs) show the frequency shift they apply; double-passed AOMs are denoted with a $\times 2$. The tapered amplifier (TA) increases the power for the MOT light. The Fabry-Pérot interferometer monitors the frequencies of the repump and slower lasers to check the injection locks. All light is coupled into single mode, polarization maintaining fibers. (right) Laser frequencies with respect to the rubidium level structure.

injection locked[3] A rough layout of the optics is shown in Fig. 2.10.

We employ an unusual trick to generate the repump light, which is detuned 6.5 GHz from the probe [24]. We directly modulate the repump laser with 6 GHz microwaves from a 1W amplifier. Nearly all of the power is reflected, but enough enters to give ∼10% power into the sidebands. When light from the master laser is injected, a sideband can be phase locked to the master rather than the carrier. Once locked, the carrier is now 6 GHz offset from the master. The correct sideband can be selected by tuning the current of the repump laser.

[3] An injection locked laser is a free running 'slave' diode, without an external cavity, injected with a few hundred microwatts from a master laser. When tuned correctly, the slave laser will phase lock to the master laser.

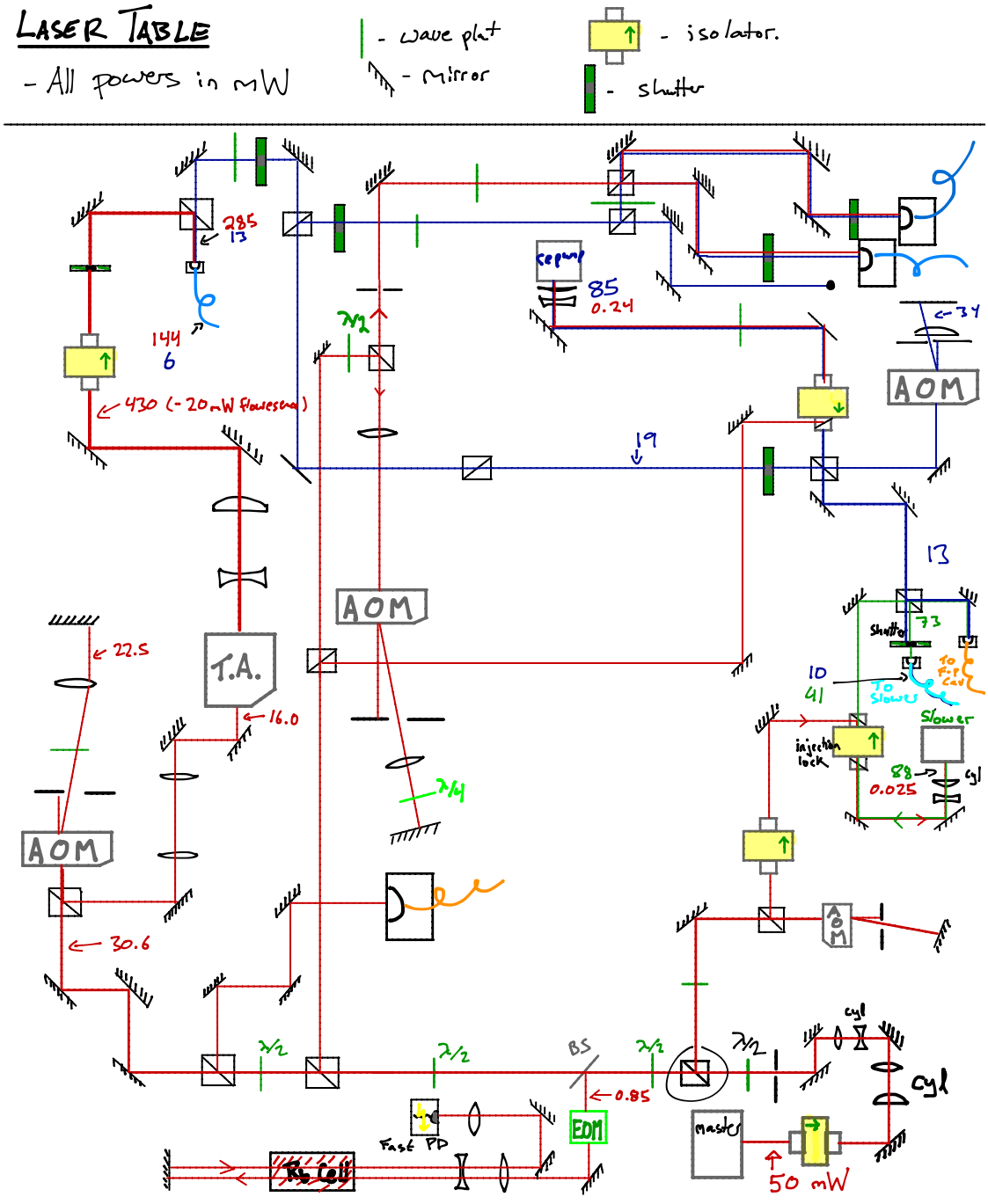

Figure 2.10: Schematic by Andrew MacRae.

Chapter 3

Phonons in an Optical Ring Trap

3.1 Background and motivation

A main motivation of our lab was to perform precision measurements of rotation by circulating atoms through an extended yet smooth magnetic ring-shaped potential. One pressing question was how to manage losses and phase shifts caused from atom-atom collisions might deteriorate the signal or bias the interferometer. When we abandoned the plan for a magnetic ring trap, an all-optical ring trap seemed like an appropriate substitute. The new trap was necessarily tiny, with a radius of 16 μm, but easily filled with a BEC.

Rotation sensing in the optical ring trap operates in a regime where the sensitivity to rotation is low, because of the small enclosed area of the ring and low atom number, but the collisional shift is huge. At low density, an experiment can detect rotation by placing atoms in a coherent superposition of rotating and counter-rotating wavepackets. This would not work in our system because the atoms would experience deleteriously large collisional shifts and scattering into other modes. For instance, an atom traveling faster than the speed of sound will scatter in a distance $d = (n\sigma)^{-1} = 30$ μm, where $n = 10^{14}$ cm^{-3} is the condensate density and $\sigma = 4 \times 10^{-12}$ cm^2 is the s-wave scattering cross section.

Many-body physics provides a hint on an alternative approach to rotation sensing. In a dense system, an atom moving through the condensate is not a solution to the many-body problem, and so we should not be surprised if it scatters and decays quickly. Instead, we should have longer lived oscillations by using a small population of elementary excitations, the low-energy solutions with well-defined energy and momentum. We chose to use phonons that propagate around the ring as the basis for our rotation sensor. It is the trapped BEC itself that guides phonons around the ring. Unfortunately, the experimental realization presented here was far too noisy to measure rotation, so we instead characterized the system by analyzing a large number of experimental repetitions for rotation noise.

Phonons can also be used to measure rotation in ordinary matter. The effect was first noticed by twisting a wine glass about its stem. Without rotation, ringing the rim of the glass creates a clean and long-lived tone[1] The standing waves can be decomposed into degenerate counter-propagating waves. When the glass is twirled, that degeneracy is broken and a clear beat note can be heard [25]. A slight complication is that the beat note occurs

[1]You must use a higher quality wine glass than I own to witness this effect.

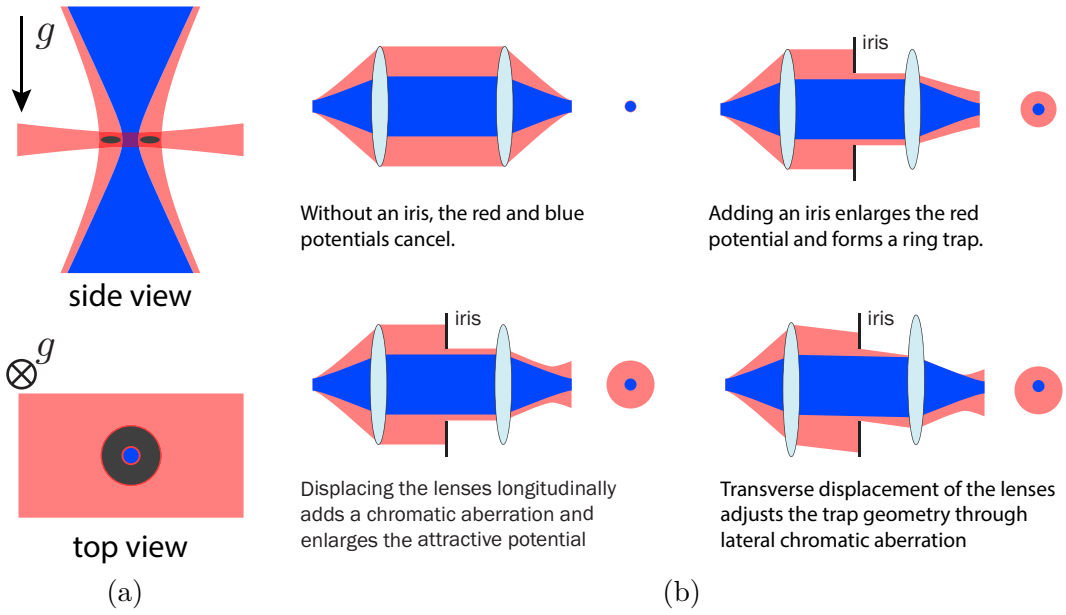

Figure 3.1: Ring trap laser scheme. (a) The trap potential is formed by crossing three laser beams. A horizontal red-detuned light sheet confines atoms against gravity (the "surfboard" trap). The annular potential is created by two lasers that propagate parallel to gravity, a red-detuned round laser beam that confines atoms into a disk and a blue-detuned tightly focused laser beam that repels atoms from the center. (b) Adjusting the annular potential. In the final iteration of the ring trap, the two beams that form the annular potential are delivered by the same large area mode fiber. At the fiber tip, the two wavelengths have nearly identical mode areas. To increase the width of the attractive potential, an iris clips in the beam in the Fourier plane. Lateral and longitudinal chromatic aberrations can be controlled by displacing two lenses.

at a frequency lower than the rotation rate because the sound is partially dragged by the rotating material—an effect absent in superfluids, which are stationary in the inertial frame. Devices with much higher quality resonators, known as hemispherical resonator gyros, are frequently used in spacecraft rotation sensing [26].

In this chapter, we will proceed by describing how we create and image an all-optical ring trap, study schemes to create and detect sound waves, and analyze our data for noise in extracting a rotation signal.

3.2 Dichromatic ring trap

The ring trap light is focused onto the atoms by the same objective used to image the atoms (Thorlabs AC508-200-B). Imaging and ring trap light is separated with a large, non-polarizing 50:50 beamsplitter.

Initially the ring trap light was reflected with a pellicle beamsplitter, a fragile stretched membrane made of nitrocellulose. The pellicle is so thin that there is no ghosting or beam deflection, but unfortunately it acts like an enormous sail that bends and deforms

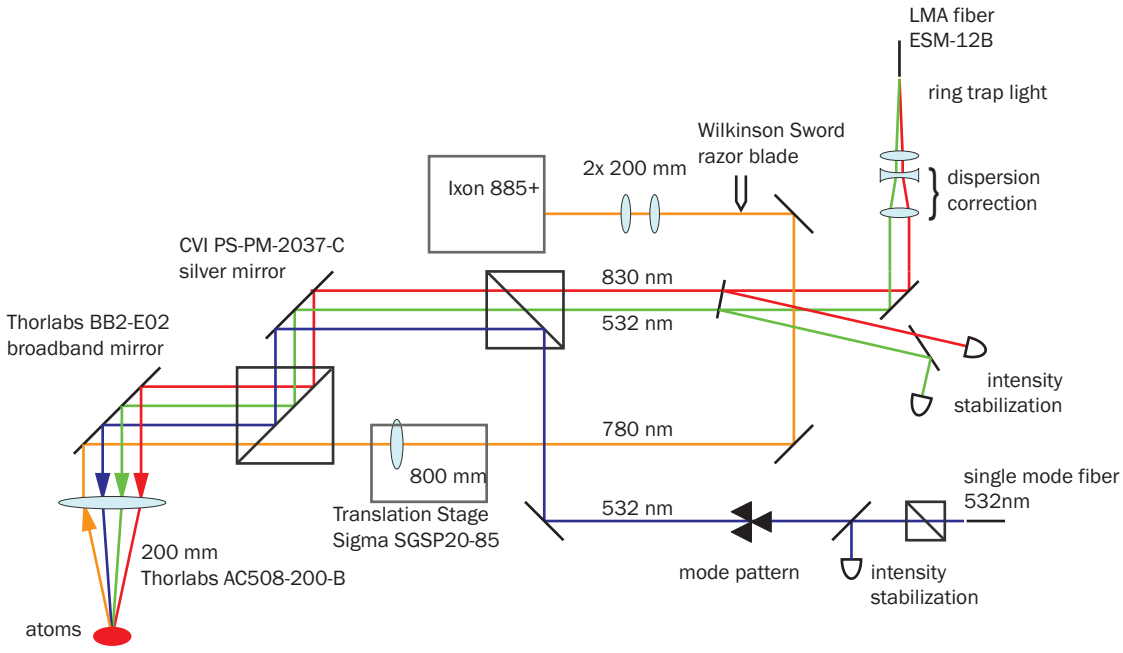

Figure 3.2: Final version of the ring trap optical setup. One objective collimates the imaging light and focuses the two annular potential lasers and azimuthal lasers. The alignment is very stable because most of the optical drift is common mode. We can diagnose and quickly align the potential by deflecting the light onto a CCD camera with a mirror between the objective and atoms. We use frame transfer mode on the camera by imaging the atoms onto the same plane as a razor blade, which is imaged onto the camera.

with changing air currents. This motion can distort the trap and heat the atoms. We eventually replaced it with a large, broadband polarizing cube. Regardless, we trudged forward for a month or two with this setup and observed the ring trap shortly after midnight on March 3, 2011, 42 days after creating a BEC. As can be seen in Fig. 3.3a, there is a hole in the atomic density but the ring is unacceptably lumpy.

The first ring trap setup used independent PM (polarization-maintaining single mode) fibers delivering the attractive (830nm) and repulsive (532nm) light. In order to create a sufficiently round potential, both paths needed cylindrical optics to match the relative astigmatisms, to which the ring trap is particularly sensitive. Long term drift between the paths limited stability. Regardless, we could create a smooth potential and start measuring the phonon modes.

At the suggestion of Gyu-Boong Jo, we installed a large area mode photonic crystal fiber (Thorlabs ESM-12B) to improve stability. These 'endlessly single mode' fibers are single mode for wavelengths from 532 nm to beyond 2000 nm! The mode waist is nearly constant for the wavelengths of interest, which implies that the shorter wavelengths has a larger divergence angle.

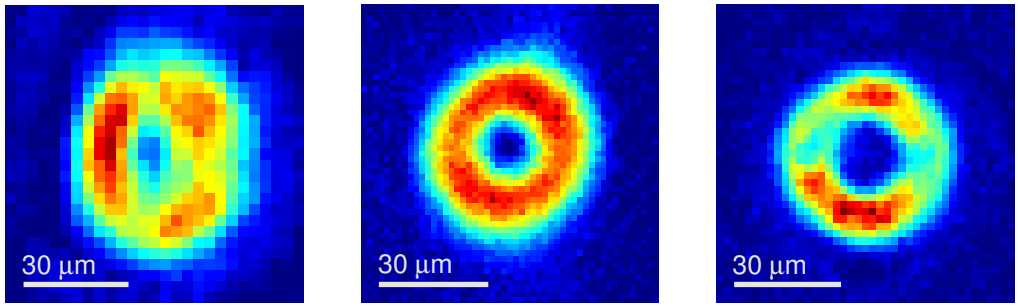

(a) (b) (c)

Figure 3.3: *In situ* images of the ring trap. (a) Our first ring trap. The potential is nonuniform but there is a clear hole in the atomic density. (b) Improving the dichromatic setup greatly helped reduce the inhomogeneity. The red and blue lasers were launched from separate fibers and passed through an independent set of cylindrical optics before combining. The alignment was finicky and had a tendency to drift. (c) Long-term stability was improved by using a single fiber launcher for the two traps. However, we had to defocus the red (attractive) laser to increase the size of the disk, which unfortunately increased the corrugations on the trap (see Fig. 3.1b). All images are 80×80 μm

3.3 Imaging phonons

The phonons used in this chapter have long wavelengths, on the order of 15–50 μm and well within the resolution of a typical imaging system. We employ high-sensitivity *in situ* imaging of the ring trap to observe the evolution of phonon modes. In principle, the phonons could by imaged after a time of flight expansion, but our momentum space resolution is insufficient to image such low momentum modes.

In situ imaging of a condensate is difficult because the high optical density of a BEC makes it too opaque to gather quantitative information [27]. We reduce the optical density with a two step scheme. First, we excite a small fraction (20–25%, typically 10^4 atoms) of the condensate from the $|F = 1, m_F = -1\rangle$ state to the $F = 2$ state by applying a weak, off-resonant repump pulse on the $F = 1 \rightarrow F' = 2$ transition of the D2 line. The repump laser propagates along the thin axis of the trap. For the repump to uniformly excite the condensate, it must pass through the condensate with minimal absorption. This is achieved by detuning the repump by 4–6 linewidths. Then, an imaging pulse at saturation intensity, resonant on the cycling ($F = 2 \rightarrow F' = 3$) D2 transition, illuminates the atoms and is imaged onto a CCD camera. At saturation intensity we have the best signal-to-noise in absorption imaging (Sec. A.3). In Sec. 4.2.3 we employ a more advanced version of this scheme to image spin as well as density. Fig. 3.4 shows a benchmarking of the imaging on the classic Thomas-Fermi of atoms in an anisotropic harmonic trap (our "surfboard" trap).

Phonon dynamics can be monitored with an azimuthal Fourier transform of the condensate density. The Fourier transform measures the coefficient A_n of $\cos n\phi$ and $\sin n\phi$

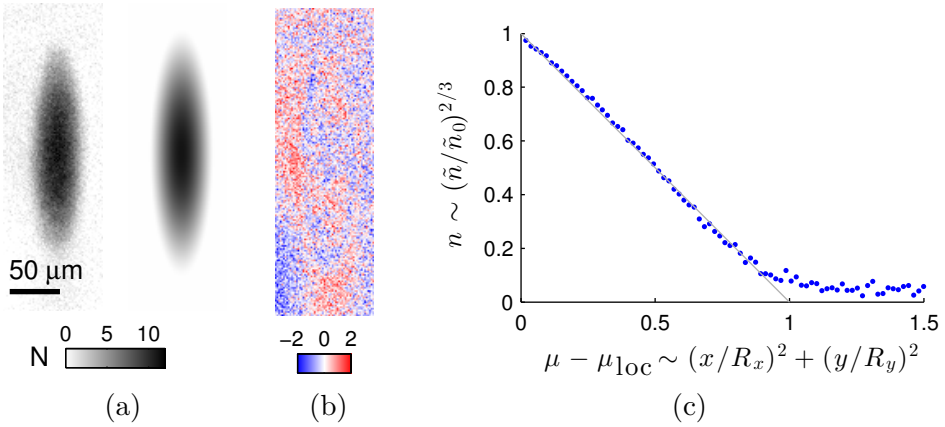

Figure 3.4: Imaging atoms in the surfboard trap. (a) Image (left) and least-squares fit (right) to a Thomas-Fermi profile $\tilde{n} = \tilde{n}_0 (1 - x^2/R_x^2 - y^2/R_y^2)^{3/2}$ of 2×10^4 atoms, approximately 5% of the sample. The scalebar is the number of atoms per 1.6 μm $\times$ 1.6 μm pixel. (b) Residuals may be due to the imaging resolution, anharmonicity of the trap, or nonlinearity in the fit. (c) Density vs chemical potential for a BEC. We integrate the in-plane density $n \propto \tilde{n}^{2/3}$ along elliptical rings of constant local chemical potential $\mu_{\rm local} = \mu - \frac{1}{2}m(\omega_x^2 x^2 + \omega_y y^2)$. When plotted in this way, we observe a linear behavior is because of the nonlinear equation of state $p = gn^2/2$ (in general, $\tilde{n} \propto \mu_{\rm local}^{(\alpha+1)/(2\alpha-2)}$ for a system with $p \propto n^\alpha$). The wings are most likely due to 2-5% thermal atoms, which exhibit a different equation of state, though imaging aberrations distorting the edge of the condensate might contribute.

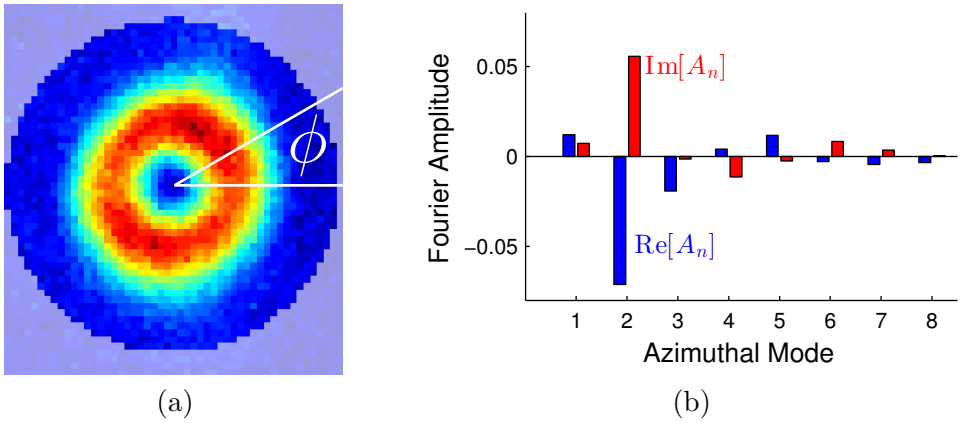

Figure 3.5: Azimuthal Fourier transform of the *in situ* column density. (a) An image of the ring is fit to determine the center. The azimuthal phase ϕ represents the angle around this point. (b) Real (blue) and imaginary (red) components of A_n as a function of mode number.

density modulations (Fig. 3.5).

$$A_n = \frac{\sum_{r<r_c} \tilde{n}(x,y) e^{in\phi(x,y)}}{\sum_{r<r_c} \tilde{n}(x,y)} \tag{3.1}$$

A sudden change in the optical potential excites phonons. For each evolution time, we create, image, and destroy one condensate. A series of images from these independent realization lets us assemble the dynamical evolution of the density in time and space, from which we calculate the time varying quantity $A_n(t)$. In general, the behavior looks like a damped harmonic oscillator, $A_n(t) = A_{n,0} + A_n e^{-\Gamma t}\cos\omega t$. The static component $A_{n,0}$ is due to corrugations in the ring potential, while the oscillating part is the amplitude of a standing wave of phonons with eigenfrequency ω.

3.4 Radial and azimuthal mode spectroscopy

3.4.1 Sound in a quantum degenerate gas

In the mean-field approximation, the energy functional of a scalar Bose-Einstein condensate is

$$E[\psi] = \int dV\, \psi^* \left(-\frac{\hbar^2}{2m}\nabla^2 + V + g\psi^*\psi\right)\psi.$$

Our condensates are well approximated by the Thomas-Fermi approximation, which assumes that the kinetic energy contribution to the ground-state energy is negligible compared to the potential and interaction terms. It can be useful to derive thermodynamic quantities for a fixed density $n = \psi^*\psi$ with a uniform potential.

$$E = \frac{1}{2}gn^2V$$

Since the energy varies nonlinearly with particle density, most thermodynamic properties have different scalings than a classical ideal gas. In particular, we are interested in the change of energy with particle number (chemical potential μ) and with volume (pressure p).

$$\mu = \frac{dE}{dN} = \frac{d}{dN}\left(\frac{gN^2}{2V}\right) = gn \qquad p = \frac{dE}{dV} = \frac{1}{2}gn^2$$

From these simple formulae, we can predict the speed of sound c.

$$\frac{1}{mc^2} = \frac{dp}{dn} = \mu \quad \Rightarrow \quad c = \sqrt{\frac{\mu}{m}} \tag{3.2}$$

For a typical rubidium condensate, $g = h \times 7.72$ Hz μm^3, $n = 10^{14}$ cm^{-3} = 100 μm^{-3}, and $c = 2$ mm/s. Unlike in an ideal gas, the speed of sound is independent of the temperature and mean thermal velocity. In the limit of long-wavelength and low-amplitude excitations, that sound propagates according to a wave equation of a density perturbation δn through an inhomogeneous sample with density n [28, 29, 30].

$$\frac{\partial^2}{\partial t^2}\delta n = \vec{\nabla}\cdot\left(c^2\vec{\nabla}\delta n\right) \tag{3.3}$$

In a ring trap, we expect separation between radial, azimuthal, and out-of-plane modes. Of particular interest are the lowest azimuthal modes, which are 'guided' around

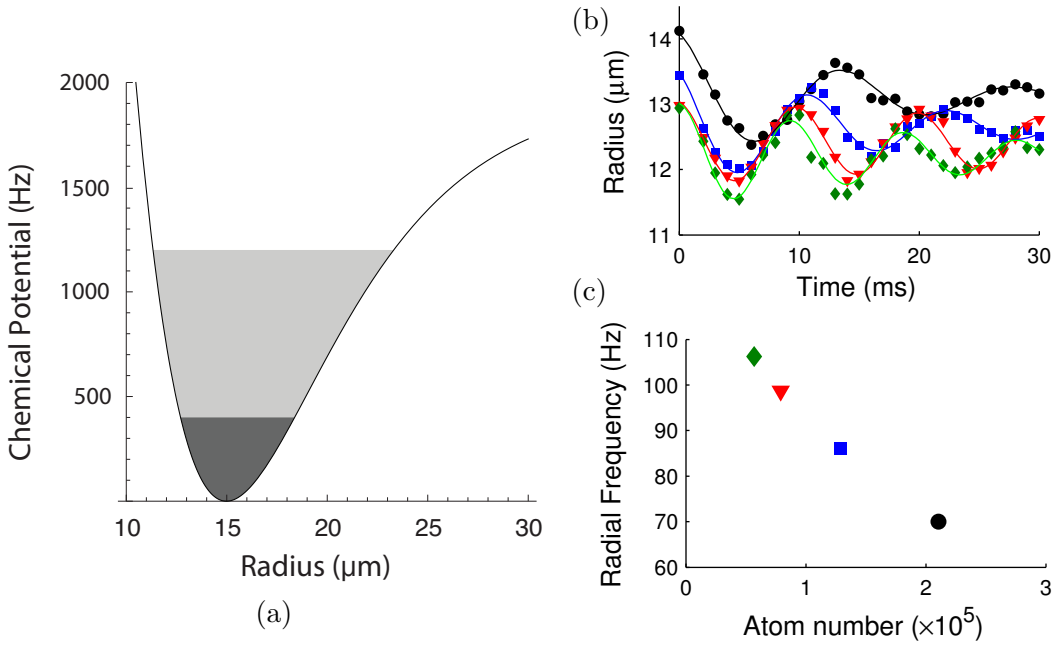

Figure 3.6: Radial mode spectroscopy. (a) As the atom number and chemical potential increase, the condensate explores the anharmonic regions of the trap. (b-c) Radial excitation frequencies are substantially suppressed at the highest atom numbers. Note that the equilibrium radius increases along with decreasing trap frequency for larger atom numbers.

the ring. We can summarize the role of the radial structure for these modes by introducing an effective channel chemical potential $\mu_{\rm ch} = \mu/a$ and channel speed of sound $c_{\rm ch} = c/\sqrt{a}$, which we assume to be constant for the lowest frequency modes. For harmonic confinement, $a = 2$, but in our trap we find $a \approx 1.8$. The new wave equation is one-dimensional and a function of the azimuthal coordinate ϕ.

$$\frac{\partial^2}{\partial t^2}\delta n = \frac{\mu}{amr^2}\frac{\partial^2}{\partial \phi^2}\delta n$$

The solutions are doubly degenerate modes labelled by an azimuthal mode number n.

$$\omega = \frac{nc_{\rm ch}}{r} \qquad c_{\rm ch} = \sqrt{\frac{\mu}{am}}$$

Later, we will see the impact of frequency splitting due to trap perturbations and trap rotations, which will introduce couplings between otherwise degenerate modes.

3.4.2 Radial excitations

The trap frequencies of a harmonically trapped sample are independent of the sample density or amplitude of the oscillation. Anharmonicity of the trapping potential will cause the frequency to depend on the amplitude of oscillation. Even the low amplitude

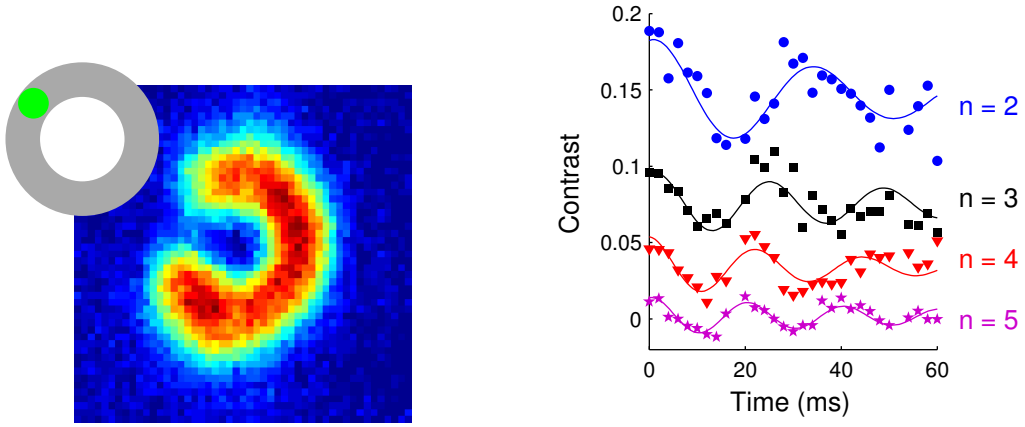

(a) (b)

Figure 3.7: First measurement of sound in the ring. (a) A focused blue-detuned 'poke' laser beam (532 nm wavelength) can completely exclude atoms from one portion of the ring. The angular size of the perturbation is 1/7 of the ring, which allows us to drive the first seven azimuthal modes. In general, the laser intensity is reduced to ∼10% of the chemical potential and only slightly perturbs the trap intensity. (b) The laser is suddenly turned off, exciting a superposition of azimuthal sound waves. The contrast of each mode Re$[A_n]$ oscillates with a frequency that increases with n.

.

oscillations of a BEC can also experience a shift when the extent of the condensate explores the anharmonic region. We study the anharmonicity of the trap by measuring the radial trap frequency as a function of atom number, where larger atom numbers correspond to a larger condensate (Fig. 3.6). In the dichromatic trap, we excite radial modes by suddenly increasing the intensity of the red-detuned laser, which reduces the equilibrium radius of the trap.

3.4.3 Azimuthal excitations

Elongated condensates act as waveguides for phonons. When the wavelength of the phonon is longer than the transverse size of the condensates, the transverse modes are effectively frozen out. For a perfectly smooth ring, azimuthal modes are doubly degenerate with an eigenfrequency proportional to the mode number n. Even though the ring has substantial perturbations, we find that the mode spectrum follows this expected linear scaling.

Suddenly changing the azimuthal potential excites phonons. Our first and simplest approach was to focus a blue-detuned (repulsive) laser onto the edge of the condensate. In a typical sequence, we condense atoms in the ring trap with the perturbing laser reducing the local chemical potential by 10–20%. Suddenly extinguishing the laser light excites sound waves in the now nearly uniform trap (Fig. 3.7). In the initial data, we observed that the frequency qualitatively increased with mode number n, but the data lacked quantitative confirmation of the mode structure. We tried to drive a single mode by resonantly oscillating

the perturbing laser light at an eigenfrequency, but the short lifetime of the modes limited the usefulness of that approach.

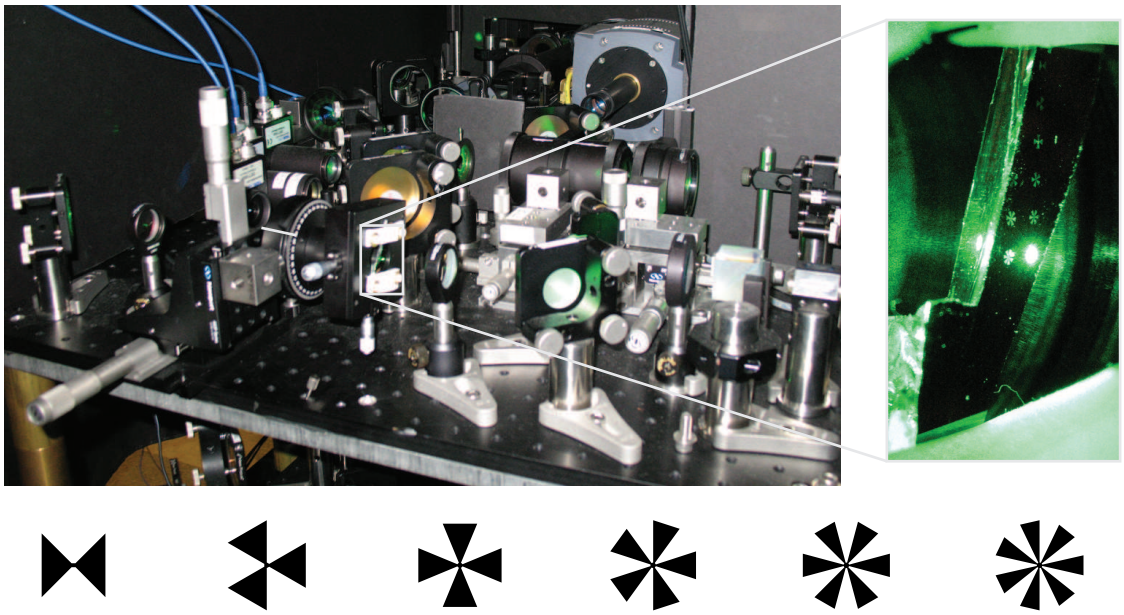

Figure 3.8: Propeller patterns to excite specific sound modes. (Top) Photo of ring trap setup. The zoomed in photo shows the mask illuminated by a 532nm laser. These masks allow us to excite specific phonon modes. (Bottom) The six patterns to excite modes $n = 2$–7.

What we needed was a method to excite individual modes with high specificity. We accomplished this by focusing 'propeller' patterns onto the atoms (Fig. 3.8). The patterns are chrome masks, each with a diameter of 400 μm, manufactured by the Berkeley Microfabrication Laboratory. A laser illuminates one pattern and is is optically imaged onto the condensate with a magnification of 1/10. To control the mode angle, the patterns are mounted on a 2D translation stage, which is mounted on a rotation stage and a second 2D translation stage. The first translation stage centers the chosen pattern onto the rotation stage's axis. The second translation stage aligns the pattern to the ring trap. It is necessary to center the pattern carefully, as slight misalignments can drive phonon modes $n \pm 1$.

With the new setup we were able to drive primarily one azimuthal mode. Fig. 3.9a shows the response of modes $n = 2$–6 when the ring is modulated with the $n = 3$ pattern. We observe a slight excitation in the $n = 2$ and 4 modes, most likely because the propeller pattern is slightly off-center. These data also show that the imaging scheme is highly selective when reading excitations: we do not detect oscillations at the eigenfrequency of the $n = 3$ mode in other A_n channels. We find similar results for all modes (Fig. 3.9b).

We can measure the phonon dispersion relation in the ring trap. In general, measuring the phonon dispersion relation with ultracold atoms requires a detailed knowledge of the density of the sample to properly establish the boundary conditions. The unterminated waveguide created by the ring trap makes this understanding more straightforward because the boundary condition is periodic. We investigate the phonon dispersion relation by driv-

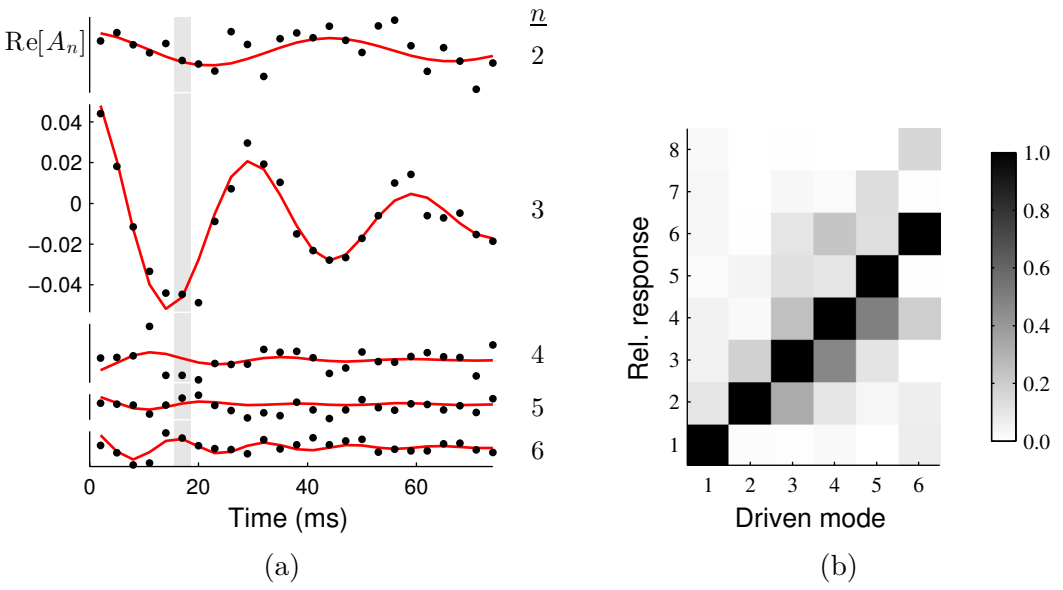

Figure 3.9: Oscillations of the $n = 3$ mode. (a) The $n = 3$ mode is driven with a laser beam masked by a propeller of the same order. Each experimental run consists of creating a condensate and imaging the sample after a specific evolution time, after which the sample is destroyed. Each time step involves a new condensate and evolution time. From each image we calculate the population for each column of data, denoted by the gray bar. (b) For each azimuthal mode, we measure the relative response for all modes as normalized to the peak response. The response is chiefly in the same mode as the drive, though we do measure non-negligble excitation for neighboring modes, most likely due to centering errors of the mask. The $n = 1$ dipole mode is excited by suddenly applying a gradient.

ing and imaging the first seven azimuthal modes. For modes 2 through 6, we observe the linear dispersion relation (Fig. 3.10).

The frequency of the $n = 7$ is far below the linear extrapolation. This is because the wavelength of the mode is on the order of the radial extent of the sample. Equivalently, the eigenfrequency is close to the first radial mode. The simple phonon waveguide model is altered because the $n = 7$ mode can propagate through the lower density outer edge of the trap, where the speed of sound is lower and effective circumference longer. Even higher mode numbers should be confined to the outer edge of the trap, similar to whispering gallery modes.

The phonons damp fairly quickly, with a quality factor $Q = \pi f/\Gamma$ of about 6 and roughly independent of mode number. It is likely that Landau damping is limiting the phonon lifetime, whereby phonons damp by scattering off of thermal atoms. In the limit $\hbar\omega \ll \mu \ll k_B T$, a spatially homogeneous condensate also has a quality factor that is independent of mode number [31].

$$Q = \frac{4}{3\pi}\frac{\hbar c}{k_B T a} \approx 35$$

This prediction is six times higher than the measured value. Our system is in a different

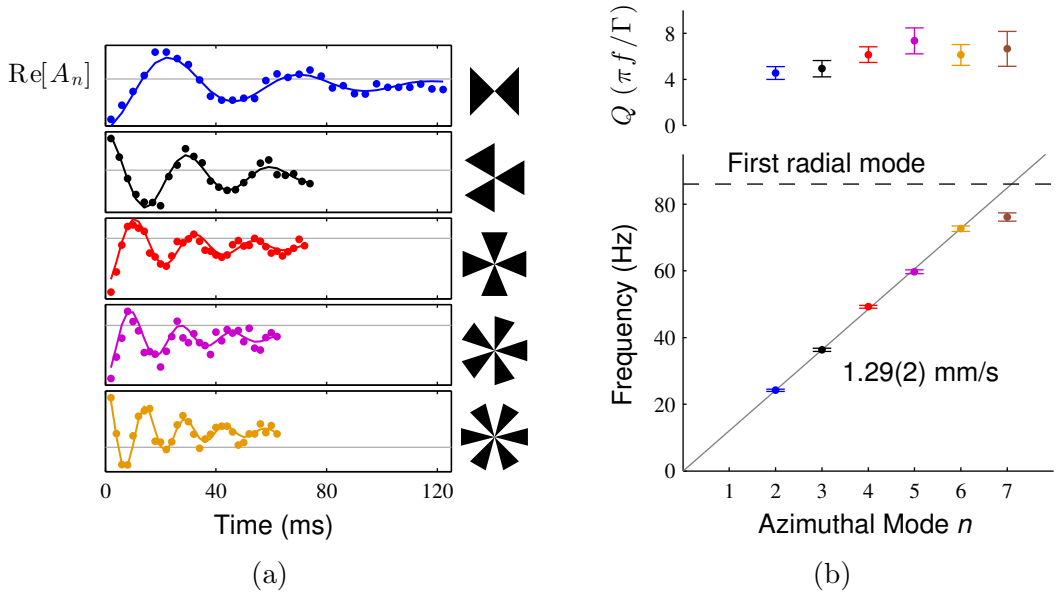

Figure 3.10: Phonon dispersion relation. (a) Oscillations for phonons modes driven by each propeller mask. (b) We see the expected linear dispersion relation of sound. The error indicated in the channel speed of sound of 1.29(2) mm/s is only statistical; the systematic error from the uncertain magnification of the imaging system and ring radius of the system is much larger (around 10%).

regime, with a nearly identical temperature and chemical potential of 30 nK, and the unusual geometry may contribute to the damping. We later observed vortices in the annular region created during condensation, which is likely to increase the damping rate.

The images used to extract the oscillating A_n components can also show the eigenmodes (Fig. 3.11). Our sequence of images establishes a record of atom column density as a function of two spatial coordinates and time, $\tilde{n}(x, y, t)$. We determine the overall oscillation frequency ω, phase ϕ, and damping rate Γ from fits to A_n, extracted using the entire image. We fit the model $\tilde{n}(x, y, t) = a(x, y)e^{-\Gamma t}\cos(\omega t + \phi) + b(x, y)$ to find the amplitude $a(x, y)$ on each pixel. The value of $a(x, y)$ can be positive or negative, depending on whether it is in-phase or out-of-phase with the arbitrary choice of phase of Re$[A_n]$. Once we have determined the form of the eigenmode, we could in principle extract the amplitude of the phonon mode with higher signal-to-noise than A_n.

An important element of control is the orientation of the standing wave. By rotating the propeller mask used to excite phonons, we can change the orientation of phonons in the ring trap. In Fig. 3.12, we rotate the $n = 3$ pattern and find that the orientation of the measured phonons rotates three times faster than the change in angle of the pattern. The importance of varying the excitation angle is that it allows us to look for small frequency splittings between nominally degenerate modes and look for a rotation signal in the data. Fig. 3.12 is a small selection of our dataset of 2800 images taken of modes $n = 1$–6 at a total of 93 orientations of the masks. The next two sections are based on this studying dataset.

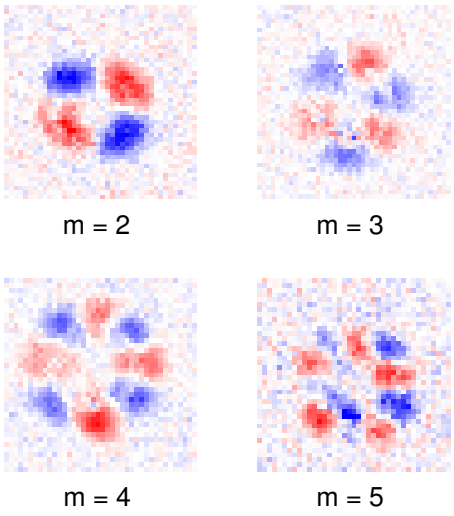

Figure 3.11: Phonon eigenmodes. Each pixel is fit to an oscillating sinusoid based on the frequency, phase, and damping rate extracted from A_n. Red and blue regions correspond to in-phase and out-of-phase amplitude with respect to our choice of phase of $\mathrm{Re}[A_n]$.

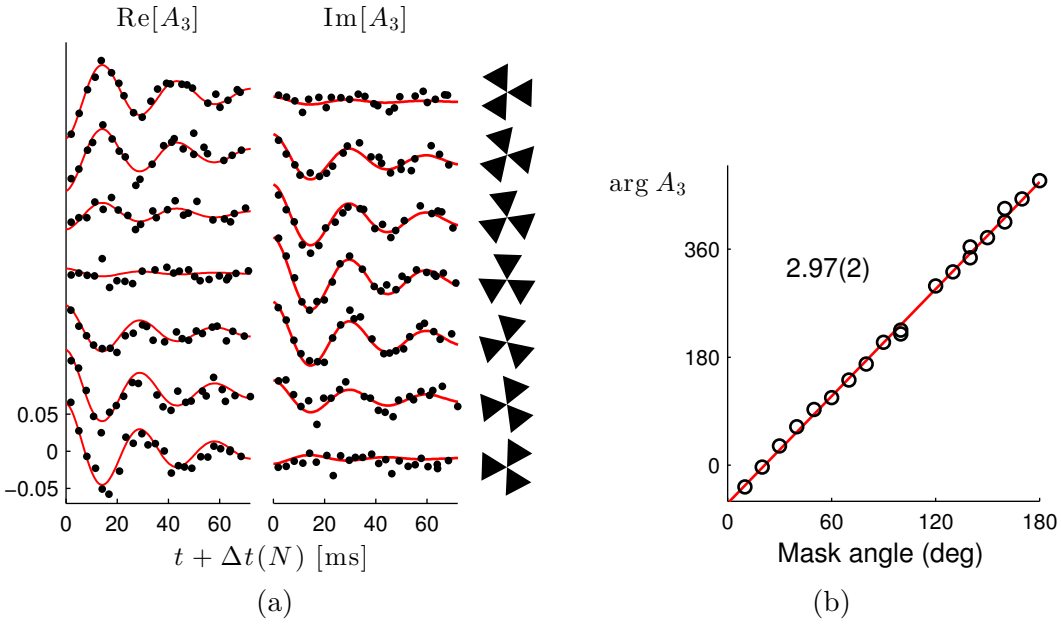

Figure 3.12: Phonon standing waves excited at many angles. (a) We rotate the axis of the phonon by rotating the optical mask used to excite them. Fitting oscillations to the real and imaginary components of A_n indicate the change in angle. We use a large set of phonon data at many angles and for modes $n = 1$–6 to extract the frequency splitting and noise in rotation rates. (b) The phonon axis, as measured by $\arg A_3$, rotates 3 times faster than the mask angle.

3.4.4 Frequency splitting from imperfections

In a perfectly smooth ring trap, there are two degenerate modes for each azimuthal mode n. An inhomogeneous potential can introduce a frequency splitting between the two modes. In particular, the degeneracy between the two modes is lifted by a perturbing potential of the form $V(\theta) = \cos(2n\theta + \theta_0)$. For example, to change the dipole frequencies of a trapped particle (an $n = 1$ oscillation), one must change the relative trap curvature, an $n = 2$ perturbation ($V \propto x^2 - y^2 \sim \cos 2\theta$). Without loss of generality, we assume that the ring is perfectly smooth except for a small $V_{2n} \cos 2n\theta$ perturbation, where small means $V_{2n} \ll \mu$. We start with the sound equation in an inhomogeneous medium [29].

$$-\omega^2 \delta n = \frac{1}{r^2}\frac{\partial}{\partial \phi}\left(c_{\mathrm{ch}}^2 \frac{\partial}{\partial \phi}\delta n\right) \qquad c_{\mathrm{ch}}^2 = \frac{\mu - V_{2n}\cos n\phi}{am}$$

Inserting the eigenstates $\cos n\phi$ and $\sin n\phi$ does not exactly solve the above equation. Instead, we will calculate the frequency shifts with first order degenerate perturbation theory and reduce the differential equation to a matrix equation. For weak perturbations, the solution should involve only superpositions of the doubly degenerate states with azimuthal number n. Our ansatz then involves the sine and cosine standing wave modes with amplitudes labelled by x and y.

$$\delta n = x f_1 + y f_2 \qquad f_1 = \cos n\phi \qquad f_2 = \sin n\phi$$

The eigenvalue problem is

$$-\omega^2 \begin{pmatrix} x \\ y \end{pmatrix} = \left(\mathcal{D}_{ij}\right) \begin{pmatrix} x \\ y \end{pmatrix}$$

where

$$\mathcal{D}_{ij} = \int d\phi\, f_j \frac{1}{r^2}\frac{\partial}{\partial \phi}\left(c_{\mathrm{ch}}^2 \frac{\partial}{\partial \phi} f_i\right).$$

Our choice of basis makes $\mathcal{D}$ diagonal.

$$\left(\mathcal{D}_{ij}\right) = \begin{pmatrix} -\omega_0^2\left(1 + \frac{V_{2n}}{2\mu}\right) & 0 \\ 0 & -\omega_0^2\left(1 - \frac{V_{2n}}{2\mu}\right) \end{pmatrix} \qquad \omega_0^2 = \frac{\mu n^2}{amr^2}$$

$$\omega_\pm = \omega_0\sqrt{1 \pm \frac{V_{2n}}{2\mu}} \approx \omega_0 + \frac{V_{2n} n}{4r\sqrt{a\mu m}}$$

Interactions suppress the frequency splitting because μ shows up in the denominator.

To compare to experiment, we measure V_{2n}/h from images of the condensate column density, $V_{2n} = \mu A_{2n}$, and directly probe $\Delta f_n = \Delta\omega_m/\pi$ by exciting standing sound waves at many angles (Fig. 3.13). Since these two quantities have the same units, the suppression must depend on a dimensionless parameter of the condensate, which in this case is the ratio of the healing length $\xi = \hbar/\sqrt{2m\mu}$ to the radius r.

$$\frac{\Delta f_n}{n} = \frac{V_{2n}}{h}\frac{\xi}{r\sqrt{2a}}$$

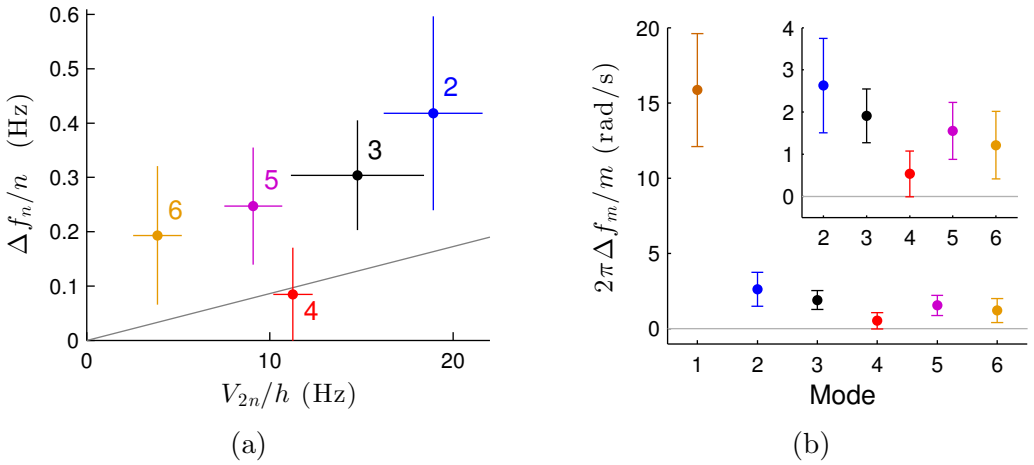

Figure 3.13: Phonon frequency splitting. (a) The frequency splitting Δf_n between the two otherwise degenerate azimuthal modes is greatly suppressed by interactions. The trap perturbations are estimated from $V_{2n} = A_{2n}\mu$, where the constant offset of A_{2n} is from images without oscillating phonons. The gray line is the prediction $\Delta f_n/n = (V_{2n}/h)(\xi/1.9r)$ (b) A large frequency splitting can suppress the phonons from being sensitive to rotations. As we will see, the frequency splitting (in units of rad/s per mode number) is less than the noise and does not decrease sensitivity.

We expect a suppression by $\xi/(1.9r) \approx 10^{-2}$. The measured suppression is around 1/50, not quite as strong as estimated but still quite substantial. It is likely that there are systematic errors in the estimates of V_{2n}.

What does this suppression represent? If we sent a dilute wavepacket of atoms around the ring, they would experience $\approx h \times 10$ Hz $= k_B \times 0.5$ nK perturbations as they propagate. Yet phonons propagating around the ring have frequency shifts of only 0.2 Hz! In addition, dilute wavepackets have mean-field shifts that cause an *increased* shift with density, an error that is absent with phonons. We see that using phonons rather than dilute atomic wavepackets can be a good strategy for minimizing errors from imperfect ring traps. In chapter 5, we will see that magnons traveling through a condensate provide greater suppression.

The uncertainty of the frequency splitting is determined by a statistical resampling technique known as jackknifing. Of the N sets of phonons and different orientations for each azimuthal mode, we fit *all but one* orientation to a model for the frequency splitting to determine Δf^i, the frequency splitting with the i^{th} run excluded. The key assumption of resampling is that the distribution of Δf^i is related to the true distribution of the Δf. The estimate of the standard error of Δf looks similar to a variance.

$$\mathrm{SE}_{\Delta f} = \sqrt{\frac{N-1}{N}\sum_{i=1}^{N}\left(\Delta f^i - \overline{\Delta f}\right)^2}$$

In the next section, we are particularly interested in using the standing wave of phonons to measure rotation. A large frequency splitting can pin the modes and limit rota-

tional sensitivity. In our setup, we find that the frequency splitting for higher order modes is sufficiently small compared to the large noise in the rotation signal (Fig. 3.13b). Improvements to the rotational sensitivity would require improved smoothness of the potential to decrease the splitting.

3.5 Phonon rotation sensor

A traditional atom interferometer measures the phase shift accrued by an atom along distinct paths [32]. For large densities (roughly, $> 10^{10}$ cm^{-3}) atoms will forward scatter and add a density-dependent phase shift. At even higher densities, atoms can scatter into other modes and deplete the population of the wavepackets. With our parameters, the scattering distance $l = (n\sigma)^{-1} = 30$ μm is only one third the distance around the ring circumference. In other words, we cannot employ a "traditional" atom interferometry approach of propagating a wavepacket of atoms through a high density ring trap.

Why is this a problem? Other experiments effectively integrate over a volume of many cubic centimeters in order to have a sufficiently high atom flux without the harmful effects of atom interactions [33, 34]. However, interesting physics can occur on far shorter scales, and a device that averages over less than a cubic millimeter could search for short-range gravity or help with material characterization. A dilute sample confined to a small volume will have too few atoms to make a competitive measurement. Instead, we must take a fundamentally different approach to atom interferometry. Many-body physics provides a solution.

Elementary excitations are the solutions to the many-body problem with well-defined momentum and energy. At high densities, elementary excitations may appear quite distinct from single-particle states. In this section, we propose and test an interferometer with phonons, the lowest-energy excitations of a scalar superfluid, in a regime where a conventional atom interferometer does not work.

3.5.1 Why a phonon rotation sensor is like a Foucault pendulum

The condensate is a superfluid, so the ground state must be stationary in the inertial (non-rotating) frame. Sound waves then must also be stationary in this frame. Thus, in a lab frame rotating at a rate Ω, the $\cos n\phi$ mode appears as a $\sin n\phi$ mode after a time t such that $\Omega t = 1/n$. In other words, the phonons create a mark of angular size $1/n$, and we can detect rotation by observing the mark precess in the lab frame. Higher order modes should, in principle, lead to a more sensitive sensor.

In the inertial frame, the wave equation for δn includes the time-dependent changes of the speed of sound [35].

$$\frac{\partial^2 \delta n}{\partial t^2} - \frac{1}{c^2}\frac{\partial (c^2)}{\partial t}\frac{\partial \delta n}{\partial t} = \frac{1}{r^2}\frac{\partial (c^2)}{\partial \phi}\frac{\partial \delta n}{\partial \phi} + \frac{c^2}{r^2}\frac{\partial^2 \delta n}{\partial \phi^2} \tag{3.4}$$

The inhomogeneous speed of sound $c^2 = (\mu - V_{2n}\cos(2n\theta - 2n\Omega t))/m$ rotates with the optical trap. It is simpler to work in the rotating frame, where we replace $\theta \to \theta + \Omega t$ and

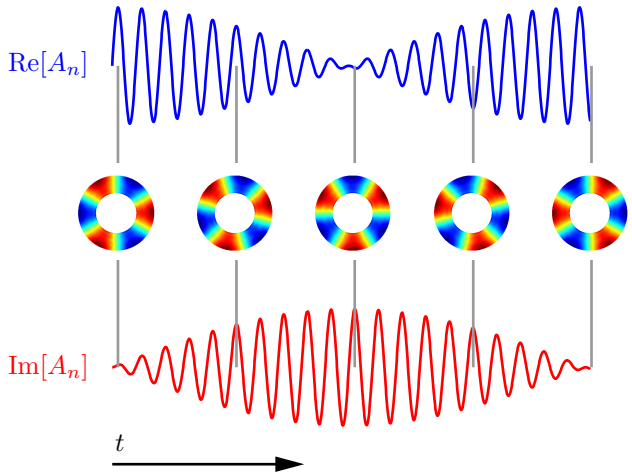

Figure 3.14

$\partial_t \to \partial_t + \Omega\partial_\phi$. In this frame c is stationary ($\partial_t c^2 = 0$).

$$\frac{\partial^2\delta n}{\partial t^2} + \Omega\left(2\frac{\partial\delta n}{\partial\phi} - \frac{1}{c^2}\frac{\partial(c^2)}{\partial\phi}\right)\frac{\partial\delta n}{\partial t} = \left(\frac{1}{r^2} + \frac{\Omega^2}{c^2}\right)\frac{\partial(c^2)}{\partial\phi}\frac{\partial\delta n}{\partial\phi} + \left(\frac{c^2}{r^2} - \Omega^2\right)\frac{\partial^2\delta n}{\partial\phi^2} \tag{3.5}$$

As before, we use our ansatz $\delta n = x\cos n\phi + y\sin n\phi$, where x and y are slowly varying functions of time. This is accomplished with perturbation theory by multiplying the above equation by $\int d\phi\, f_j\mathcal{D}[f_i]$. The new terms in $\partial\delta n/\partial t$ contribute off-diagonal components that couple x and y.

Neglecting terms on the order of Ω^2, the equation of motion of x and y are identical to an anharmonic, rotating harmonic oscillator.

$$\begin{aligned}\ddot{x} &= 2n\Omega\dot{y} + (\omega_0 + \delta)^2 x\\ \ddot{y} &= -2n\Omega\dot{x} + (\omega_0 - \delta)^2 y.\end{aligned}$$

We can solve this by reducing it to a 4×4 first-order equation.

$$\begin{pmatrix}\ddot{x}\\ \ddot{y}\\ \dot{x}\\ \dot{y}\end{pmatrix} = \begin{pmatrix}0 & 2\Omega & (\omega+\delta)^2 & 0\\ -2\Omega & 0 & 0 & (\omega-\delta)^2\\ 1 & 0 & 0 & 0\\ 0 & 1 & 0 & 0\end{pmatrix}\begin{pmatrix}\dot{x}\\ \dot{y}\\ x\\ y\end{pmatrix}$$

In the limit, $\Omega, \delta \ll \omega$, we solve for the eigenvectors to zeroth order and the eigenvalues to first order. What we want to know is the response of the system when kicked along an eigenaxis. Linearity will let us combine those solutions for an arbitrary kick. Solving the above equation to the appropriate orders, define $A_{\sigma\nu}$ as the response along the ν axis to a

system kicked along the σ axis.

$$\begin{aligned}
A_{xx} &= \cos(\omega t)\cos(\Omega' t) - \frac{\delta}{\Omega'}\sin(\omega t)\sin(\Omega' t) \qquad \Omega' = \sqrt{\Omega^2 + \delta^2} \\
A_{xy} &= \frac{\Omega}{\Omega'}\cos(\omega t)\sin(\Omega' t) \\
A_{yx} &= -\frac{\Omega}{\Omega'}\cos(\omega t)\sin(\Omega' t) \\
A_{yy} &= \cos(\omega t)\cos(\Omega' t) + \frac{\delta}{\Omega'}\sin(\omega t)\sin(\Omega' t)
\end{aligned} \tag{3.6}$$

An alternative and instructive derivation is to use Hamiltonians and solve it "quantum mechanically". We start with the classical Lagrangian of a two-dimensional rotating anisotropic harmonic oscillator.

$$\begin{aligned}
L &= \frac{m}{2}\left|\dot{\vec{r}} + \vec{\Omega}\times\vec{r}\right|^2 - U(r) \\
&= \frac{m}{2}\left[(\dot{x} - \Omega y)^2 + (\dot{y} + \Omega x)^2 - (\omega+\delta)^2 x^2 - (\omega-\delta)^2 y^2\right]
\end{aligned}$$

As we know, to convert to a Hamiltonian, we define the canonical momenta $p_i = dL/d\dot{x}_i$ and use $H = \sum_i \dot{x}_i p_i - L$.

$$H = \frac{p_x^2}{2m} + \frac{p_y^2}{2m} + \Omega(p_x y - p_y x) + \frac{m}{2}(\omega+\delta)^2 x^2 + \frac{m}{2}(\omega-\delta)^2 y^2$$

Let's switch to quantum mechanics by replacing x_i and p_i with operators and define annihilation and creation operators for each.

$$\begin{aligned}
x &= \sqrt{\tfrac{\hbar}{2m(\omega+\delta)}}(a_x^\dagger + a_x) \quad p_x = i\sqrt{\tfrac{\hbar m(\omega+\delta)}{2}}(a_x^\dagger - a_x) \\
y &= \sqrt{\tfrac{\hbar}{2m(\omega-\delta)}}(a_y^\dagger + a_y) \quad p_y = i\sqrt{\tfrac{\hbar m(\omega-\delta)}{2}}(a_x^\dagger - a_x)
\end{aligned}$$

If we substitue these into the Hamiltonian and expand to first order (neglect Ω^2, δ^2, and $\Omega\delta$) and drop the zero-point term, we find the following simple form.

$$H = \hbar\omega(a_x^\dagger a_x + a_y^\dagger a_y) + \hbar\delta(a_x^\dagger a_x - a_y^\dagger a_y) + i\hbar\Omega(a_x^\dagger a_y - a_y^\dagger a_x) \tag{3.7}$$

It is tempting to create a two-level system between, for instance, $|0,1\rangle$ and $|1,0\rangle$ states in the $|n_x, n_y\rangle$ basis, but in this basis $\langle x\rangle$ and $\langle y\rangle$ are exactly zero. Instead, we need to see an oscillation by beating the two-level system $|1,0\rangle, |0,1\rangle$ with the ground state $|0,0\rangle$, simulating a coherent state. To recover the classic equations, we work in the three-state basis.

$$\begin{pmatrix} a \\ b \\ c \end{pmatrix} \Leftrightarrow a|1,0\rangle + b|0,1\rangle + c|0,0\rangle$$

$$H \Leftrightarrow \begin{pmatrix} \omega+\delta & -i\hbar\Omega & 0 \\ i\hbar\Omega & \omega-\delta & 0 \\ 0 & 0 & 0 \end{pmatrix} \qquad x \propto \begin{pmatrix} 0 & 0 & 1 \\ 0 & 0 & 0 \\ 1 & 0 & 0 \end{pmatrix} \qquad y \propto \begin{pmatrix} 0 & 0 & 0 \\ 0 & 0 & 1 \\ 0 & 1 & 0 \end{pmatrix}$$

An initial 'kick' in the x direction is equivalent to the initial state $|1,0\rangle + |0,0\rangle$.

$$\psi(t=0) \Leftrightarrow \frac{1}{\sqrt{2}} \begin{pmatrix} 1 \\ 0 \\ 1 \end{pmatrix} \qquad \psi(t) \Leftrightarrow \frac{1}{\sqrt{2}} \begin{pmatrix} e^{i\omega t}\left(\cos(\Omega' t) - i\frac{\delta}{\Omega'}\sin\Omega' t\right) \\ e^{i\omega t}\frac{\Omega}{\Omega'}\sin\Omega' t \\ 1 \end{pmatrix}$$

We can then recover Eq. 3.6 by identifying $A_{xx} = \langle\psi(t)|x|\psi(t)\rangle$ and $A_{xy} = \langle\psi(t)|y|\psi(t)\rangle$.

3.5.2 Experimental measurement of rotation noise

We use the previously mentioned large dataset of phonon excitations for the $n =$ 1–6 modes at many angles (reproduced in Fig. 3.15a). Ideally we would apply a rotation and measure it with the phonon sensor, such as the Earth's rotation rate of 7×10^{-5} rad/s. Unfortunately, as we will see, the fundamental noise limit of our device is only several rad/s, and all measured rotation signals are consistent with zero. Instead, we characterize the noise in extracting the rotation signal and find that the noise of the higher order modes ($n \geq 4$) is consistent with atom shot noise.

We extract the rotation noise by fitting a small subsample of the data, oscillations at one angle (e.g., gray region of Fig. 3.15a), to a model where the only free parameters are the rotation rate and oscillation amplitude. The phonon frequency, frequency splitting, eigenaxes, etc., are fixed to parameters determined by the rest of the dataset from all orientations *except* for the one being fit for rotations (i.e., all other rows of Fig. 3.15a). In effect, we are treating the rest of the dataset as a calibration of the sensor (all orientation but one), and use the selected subsample (one orientation angle) to measure rotation. This process is repeated for each orientation, which provides a distribution of rotation rates while sampling all of the data. From the distribution of measured rotation rates, we estimate our error in measuring the rotation rate by assuming a Gaussian distribution (Fig. 3.15b, top). The rotation noise has a standard deviation of a few rad/s.

The fundamental noise limit in our scheme is set by the atomic shot noise. As we have a finite number of atoms, there is a fundamental noise in measuring A_m and in turn extracting the rotation rate Ω. In a smooth ring without phonons, half of the atoms in the sample contribute to each of the real and imaginary components of A_m, and so we expect the atom shot noise to be of order $N^{-1/2}$, where N is the total atom number. Our assumption of atom shot noise is that the variance of the column density on pixel i is equal to the column density (var $\tilde{n}_i = \tilde{n}_i$). (The "rule" for propagating variances is that, if c is a constant, var $(cx) = c^2$ var x)

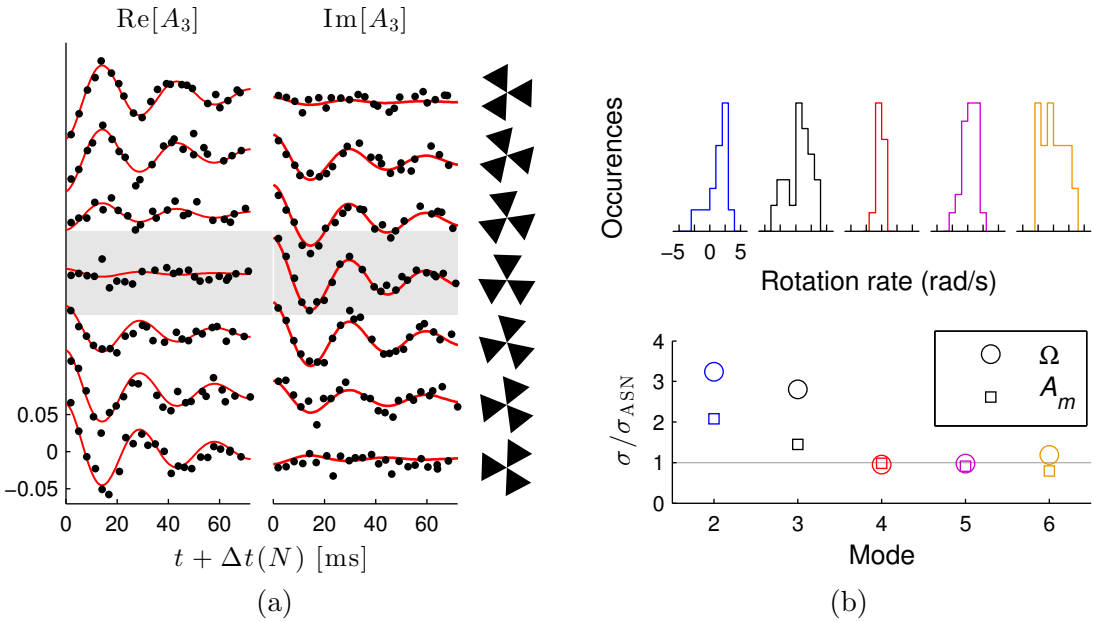

Figure 3.15: Noise of the rotation signal. (a) For each angle of the propeller pattern, we fit our model for a rotation and amplitude. The properties of the oscillator (eigenfrequency, frequency splitting, splitting axes, etc.) are fixed from a fit to all data excluding the angle being tested. (b, top) A histogram of the extracted rotation is centered around zero and has a deviation of a few rad/s. (b, bottom) For higher order modes, both the noise in the amplitude and rotation match atom shot noise for our setup.

$$\begin{aligned}
\mathrm{Re}[A_n] &= \frac{\sum_i \tilde{n}_i \cos n\phi_i}{\sum_i \tilde{n}_i} \\
\mathrm{var}\ \mathrm{Re}[A_n] &\approx \frac{\sum_i \mathrm{var}\ \tilde{n}_i \cos^2 n\phi_i}{\left(\sum_i \tilde{n}_i\right)^2} \\
&= \frac{\sum_i \frac{1}{2}\tilde{n}_i}{\left(\sum_i \tilde{n}_i\right)^2} \\
&= \frac{1}{2N}
\end{aligned}$$

The real and imaginary components of A_n have the same noise. Let us assume that the phonon is excited such that the initial amplitude falls entirely along $\mathrm{Re}[A_n]$. For short times and small rotations, the signature of rotation is contained in the imaginary component. Without perturbations in the ring, the imaginary component has a simple form, proportional to the normalized fraction $A_n(0)$ of atoms participating.

$$\mathrm{Im}[A_n(t)] = A_n(0)e^{-\Gamma t}\cos\omega t \sin n\Omega t$$

For each iteration of the experiment, we can calculate the atom shot noise limited uncer-

tainty in Ω for data taken at a particular time.

$$\begin{aligned}\Delta\Omega(t) &= \frac{\text{std Im}[A_n]}{|\partial \,\text{Im}[A_n]/\partial\Omega|_{\Omega=0}} \\ &= \frac{(2N)^{-1/2}}{A_n(0)nte^{-\Gamma t}\,|\cos\omega t|}\end{aligned}$$

In our data, we sample M times uniformly between $t = 0$ and $t = 2/\Gamma$ to $3/\Gamma$. Remember, if we have data with uncertainties $\Delta x_1, \Delta x_2, \ldots$, the averaged uncertainty is $\Delta x = \left(\sum_i \Delta x_i^{-2}\right)^{-1/2}$. We assume that $\omega \gg \Gamma$.

$$\begin{aligned}\Delta\Omega_{\text{ASN}} &= \left[\frac{\Gamma}{a}\int_0^{a/\Gamma} \frac{M}{\Delta\Omega(t)^2}\right]^{-1/2} \\ &= \left[\frac{M\Gamma}{a}\int_0^{a/\Gamma} dt\, 2N A_n(0)^2 n^2 t^2 e^{-2\Gamma t}\cos^2\omega t\right]^{-1/2} \\ &\approx \frac{\Gamma}{A_n(0)n\sqrt{NM}}\sqrt{\frac{8a}{\int_0^{2a} du\, u^2 e^{-u}}} \\ &= \frac{\Gamma}{A_n(0)n\sqrt{NM}} \times \begin{cases} 3.5 & a = 1 \\ 3.2 & a = 2 \\ 3.6 & a = 3 \end{cases}\end{aligned}$$

This compact formula for $\Delta\Omega_{\text{ASN}}$ allows us to benchmark our sensor without the messy and occasionally biased business of propagating errors through the many stages of analysis. In Fig. 3.15b, we plot the measured noise in A_n and Ω divided by the atom shot noise estimates from the above analysis. For modes 4–6, we are right at the atom shot noise limit. The lowest order modes have an excess of noise, which we believe is due to stability errors in the trap potential that cause artifacts or drifts in the mechanical properties. It is also possible that thermal noise can contribute to A_n for the lowest modes.

Comparing to atom shot noise gives us clear directions to improve the experiment. In particular, since we are already at the atom shot noise limit, improving imaging and ring smoothness would not immediately help. At first glance, it appears as if a larger ring will not help either. In reality, a larger ring would allow us to increase the atom number at constant chemical potential and increase n at a fixed wavelength. For example, in a ring trap with a millimeter radius and several 3×10^5 atom number, as demonstrated in Ref. [1], a phonon with a 6 μm wavelength would correspond to a $n = 1000$ azimuthal mode. If the phonon lifetime were increased to 1 second, with $A_n(0) = 0.1$, the single-shot sensitivity would reach the Earth's rotation rate.

3.6 Future: Spin-orbit coupling

Ideally, we would measure a nonzero rotation with the interferometer. We considered rotating the optical table during the experiment, but an optical table rotating at a

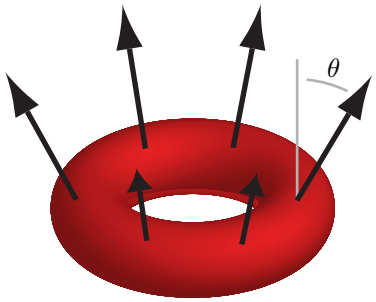

Figure 3.16: Spin-orbit coupling scheme in the ring trap. An inhomogeneous magnetic field can couple spin and rotation, creating an effective Hamiltonian analogous to a charged particle in a magnetic field.

rad/s would be dangerous. Instead, spin-orbit coupling could create an effective rotating frame in which the condensate ground state had circulation. One approach is Fig. 3.16, where the atoms move in the presence of an inhomogeneous magnetic field.

As a magnetic neutral particle moves through an inhomogeneous field, it must constantly readjust the orientation of its spin to reflect its surroundings. This constant readjustment can make the trajectory bend, as if it were a neutral particle in a rotating frame or a charged particle in a magnetic field. We start with a wavefunction with a scalar component $\psi(x)$ and spatially-dependent spin rotation $R(x)|m_z\rangle$ oriented along the local magnetic field.

$$|\Psi\rangle = \psi(\vec{x})R(\vec{x})|m_z\rangle$$

We want to derive an adiabatic Hamiltonian that acts only on the scalar component and allow the spin component to separate.

$$H|\Psi\rangle \rightarrow R\left(H_{\text{adiabatic}}|\psi\rangle\right)|m_z\rangle \qquad H_{\text{adiabatic}} = \langle m_z|R^\dagger H R|m_z\rangle$$

The kinetic energy of the Hamiltonian is $-\frac{h^2\nabla^2}{2m}$.

$$\begin{aligned}
-\frac{\hbar^2}{2m}\nabla^2(\psi R|m_z\rangle) &= -\frac{\hbar^2}{2m}\left[(\nabla^2\psi)R + 2\vec{\nabla}\psi\cdot\vec{\nabla}R + \psi\nabla^2 R\right]|m_z\rangle \\
&= \frac{1}{2m}R\left[(-i\hbar\vec{\nabla} - i\hbar R^\dagger\vec{\nabla}R)^2\psi\right]|m_z\rangle \\
&= R\left[\frac{\left(\vec{p}-\vec{A}\right)^2}{2m} + \Phi\right]\psi|m_z\rangle \qquad \begin{array}{l}\vec{A} = i\hbar R^\dagger\vec{\nabla}R \\ \Phi = 0\end{array}
\end{aligned}$$

This derivation most likely contains an error in Φ, as previous papers find a nonzero value [36, 37]. The terms $\vec{A}$ and Φ are tensors in spin space. The critical assumptions is that there are no spin-flips because the spin energy $\vec{\mu}\cdot\vec{B}$ is large compared to the kinetic

energy. In this assumptions, only the diagonal components of $\vec{A}$ and Φ matter.

$$H_{\text{adiabatic}} = \frac{\left(\vec{p} - \vec{A}\right)^2}{2m} + \Phi + g_F m_F \mu_B |\vec{B}| \tag{3.8}$$

$$\vec{A} = i\hbar \langle m_z | R^\dagger \vec{\nabla} R | m_z \rangle \tag{3.9}$$

It is easiest to calculate $\vec{A}$ in terms of the local Euler angles such that

$$R(\alpha, \beta, \gamma) = e^{-iS_z\gamma/\hbar} e^{-iS_y\beta/\hbar} e^{-iS_z\alpha/\hbar}.$$

Let us assume the particle has a pure spin projection m_F along the local field.

$$\vec{A} = m_F \left(\vec{\nabla}\alpha + \cos\beta \, \vec{\nabla}\gamma \right)$$

As with classical electromagnetism, physical observables depend not on $\vec{A}$ but on its curl. The Hamiltonian is the same as for a charged particle in an effective magnetic field (with units of momentum)

$$\vec{B}_{\text{eff}} = 2m_F (\vec{\nabla}\beta \times \vec{\nabla}\gamma) \sin\beta.$$

Note that the angle α has dropped out. This due to the gauge invariance of $\vec{A}$.

For the particular setup shown in Fig. 3.16, we assume that the atoms are confined tightly in the radial and axial directions and only the azimuthal dynamics are possible, so $\vec{p} = \frac{1}{r}\hat{\phi} L_z = (-i\hbar/r)\partial/\partial\phi$. In this geometry, $\alpha = \gamma = \phi$ is the azimuthal angle (we are free to chose α). Ignoring Φ, the kinetic energy is particularly simple.

$$H = \frac{(L_z - m_F(1 + \cos\beta))^2}{2mr^2}$$

The trap deformation is cylindrically symmetric, so the angular momentum projection $J_z = L_z + F_z$ is conserved, where $F_z = m_F(1 + \cos\beta)$ is the projection of the internal spin of the atom. In a superfluid, this defines the ground state flow of the condensate.

$$\Omega = \frac{\hbar}{mr^2} m_F (1 + \cos\beta)^2.$$

A ring with a 16 μm radius and $m_F = -1$ would rotate at 3 rad/s. Note that the magnetic moment of the state is irrelevant. This could be experimentally tested by comparing the motion of atoms in the $|F = 1, m_F = -1\rangle$ and $|F = 2, m_F = +1\rangle$ states, which have the same magnetic moment but should rotate in opposite directions.

We tried was to bring the magnetic field zero through the ring to adiabatically bring β from 0 to π, which would introduce $2\hbar$ of rotation. This process transfers angular momentum to the atoms and leaves them in a uniform bias field. However, the large magnetic field gradients required for careful positioning of the field excessively heated the sample. A similar procedure successfully wrote vortices by inverting a DC magnetic trap [38] and by resonantly oscillating the inhomogeneous magnetic field [39].

In the process, we began to be interested in spin physics, starting with spin vortices as described in Ryan Olf's thesis. While we abandoned spin-orbit coupling, the following chapters discuss our foray in spinor condensates and magnetic excitations.

Chapter 4

Spinors: Imaging and Control

4.1 Introduction to the physics of spinors

4.1.1 Why spinors: magnetism and emergence

In the Landau theory of phase transitions, broken symmetries dictate the low temperature properties of a material. We start by looking for symmetries of the Hamiltonian that a low temperature state might break. For instance, a superfluid breaks phase symmetry while a ferromagnet breaks rotational symmetry, though examples may become endlessly more complicated. The broken symmetry is characterized by an order parameter (phase for a superfluid, magnetization for a ferromagnet). Once identified, we see whether a mean-field wavefunction can lower the free energy by breaking the symmetry. If so, we may be in luck! If we indeed have identified the correct broken symmetry, we immediately know about two important classes of excitations: Nambu-Goldstone bosons and topological excitations.

Nambu-Goldstone bosons are (usually) gapless modes that consist of fluctuations of the order parameter along the broken symmetry. At very low temperature, these may be the only excitations that can be thermally excited. Thus, by understanding the spectrum of Nambu-Goldstone bosons, we can predict the low temperature thermodynamics and transport properties of a material. Experimentally, these properties may be more important in "understanding" a material than the details of the ground state.

Topological excitations, on the other hand, are energetically costly excitations that involve the 'warping' of the order parameter. These excitations are important because they are long-lived, since by definition they cannot be removed by local changes. Examples include vortices in a superfluid and skyrmions in a ferromagnet[1].

Ultracold spinor gases are a successful example of this approach. The physics governing the system is so simple it may be calculated from first principles. For instance, the ground state phases and locations of the phase boundaries can be calculated. Several basic phases have been experimentally observed, including ferromagnetic and polar in the $F = 1$ condensate studied here, while more subtle phases involving dipolar interactions are yet to be discovered.

[1] It is an interesting side note that these can wreak havok in some systems; we did not realize that some of our measurements were plagued by vortices created during condensation until we developed tools to measure them. While this would have been an important observation in 1999, by 2013 is was an annoyance!

It is through the phenomenon of emergence that ultracold gases can teach us about magnetic materials. I should emphasize that understanding *why* an ultracold gas of bosons is a ferromagnet does not inform us *why* a piece of iron is a ferromagnet. The microscopic physics the lead to magnetism is distinct in these two cases. Similarities emerge on a larger scale. Because both ultracold rubidium and a room temperature chunk of iron are ferromagnets, we can immediately predict that both contain magnons with a quadratic dispersion relation. Therefore, the density of states must scale in the same way and the two systems should have the same power law scaling of specific heat and other thermodynamic properties, though the actual values will differ by many orders of magnitude. This is the success of emergence and universality: we discover that two system may share macroscopic properties even when those systems may appear unrelated at the microscopic level.

A good introduction to this approach can be found in Ref. 40.

4.1.2 The Hamiltonian

Before we develop a qualitative understanding of the physics, it can be helpful to start off with the Hamiltonian. It is helpful to split the Hamiltonian into single particle terms and spin-independent and -dependent interactions.

$$H = H_{\text{single particle}} + H_{\text{spin-indepedent interactions}} + H_{\text{spin-dependent interactions}} \tag{4.1}$$

$$H_{\text{single particle}} = \int d\vec{r} \sum_{\alpha} \left[-\psi_\alpha^\dagger \frac{\hbar^2}{2m} \nabla^2 \psi_\alpha + \psi_\alpha^\dagger V_\alpha(\vec{r}) \psi_\alpha + g \psi_\alpha^\dagger \vec{F}_{\alpha\beta} \psi_\beta \cdot \vec{B} \right]$$

$$H_{\text{spin-indepedent interactions}} = \int d\vec{r} \sum_{\alpha\beta} \frac{c_0}{2} \psi_\alpha^\dagger \psi_\beta^\dagger \psi_\beta \psi_\alpha \qquad c_0 = \frac{4\pi\hbar^2(a_0 + 2a_2)}{3m}$$

$$H_{\text{spin-depedent interactions}} = \int d\vec{r} \sum_{\alpha\beta\alpha'\beta'} \frac{c_2}{2} \psi_\alpha^\dagger \psi_\beta^\dagger \vec{F}_{\alpha\beta} \cdot F_{\alpha'\beta'} \psi_{\beta'} \psi_{\alpha'} \qquad c_2 = \frac{4\pi\hbar^2(a_2 - a_0)}{3m}$$

4.1.3 Ground states and separation of scales

For the $F = 1$ states of ^{87}Rb, the spin-independent terms are much larger than the spin-dependent terms with $c_0 \approx 200\, c_2$: $c_0 = h \times 7.80$ Hz μm^3 and $c_2 = -h \times 0.036$ Hz μm^3.

It is conceptually helpful to understand the ground state in terms of a separation of scales, much like a Born-Oppenheimer approximation. We will solve the problem of ground-state behavior as well as dynamics by (1) solving the ground-state density profile n_{tot} for $c_2 = 0$ and then (2) solve for the spin dynamics or ground state given a fixed density profile.

The spin-independent Hamiltonian has three terms: a kinetic energy, a potential energy, and an interaction energy. The potential energy is minimized when the extent of the wavefunction is minimized, while the interaction and kinetic energies are minimized by increasing the extent of the wavefunction. Unless all three are of the same energy, we expect the density distribution to be set by competition between potential and kinetic energy (Gaussian ground state) or between potential and interaction energy (Thomas-Fermi ground

state). Our system exists in the latter regime and we can safely ignore kinetic energy when calculating the ground state distribution. This makes the Hamiltonian especially simple as every remaining term is diagonal in the position-space basis.

$$E_{TF} = V(\vec{r})n(\vec{r}) + \frac{1}{2}c_0 n(\vec{r})^2 + \frac{1}{2}c_2 n(\vec{r})^2\langle\vec{F}^2\rangle + q\langle F_z\rangle^2 n(\vec{r})$$

We can directly solve for $n(\vec{r})$. By convention, we solve for $\mu = \partial E_{TF}/\partial n(\vec{r})$. For $c_2 = 0$ and $q = 0$

$$n(x) = \frac{\mu - V(x)}{c_0}$$

The next step is to fix this density distribution and calculate the ground state spin density. This can be done by minimizing the mean-field functional

$$E_{MF}[n] = n\left(\frac{1}{2}c_2 n\langle F\rangle^2 + q\langle F_z\rangle\right).$$

In the $F = 1$ states of ^{87}Rb, $c_2 < 0$. Neglecting the linear Zeeman shift, it is straightforward to solve for the ground state magnetization.

$$\psi[n] = \begin{cases} (0,1,0) & q > 2|c_2|n \\ \frac{1}{2}(e^{-i\phi}, \sqrt{2}, e^{i\phi}) & 2|c_2|n > q > 0 \\ (1,0,0) \text{ or } (0,0,1) & 0 > q \end{cases}$$

We can see how symmetry plays a key role in these cases. The Hamiltonian satisfies cylindrically symmetry, and so the ground states must as well. For $q > 2c_2 n$, the ground state $(0,1,0)$ is singly degenerate and cylindrically symmetric. For $2c_2 n > q$, there are multiply degenerate ground states. Rotation about the z axis might not preserve the state, but it will connect it to degenerate states. This is an example of a broken symmetry, where the ground state breaks a symmetry of the Hamiltonian and therefore must be part a degenerate subspace. It is worth emphasizing that the magnetization is typically constrained in a real experiment, and the above wavefunctions may be inaccessible to the system.

4.1.4 Dynamics

For the spin-dependent term, we start with

$$H_S = \frac{c_2}{2}\sum_{\alpha\,\alpha'\,\beta\,\beta'}(\psi^\dagger_\alpha \vec{F}_{\alpha\beta}\psi_\beta)\cdot(\psi^\dagger_{\alpha'}\vec{F}_{\alpha'\beta'}\psi_{\beta'}).$$

It is easiest to calculate in the spherical basis, where $\psi = (\psi_+, \psi_0, \psi_-)$.

$$F_+ = \sqrt{2}\begin{pmatrix} 0 & 1 & 0 \\ 0 & 0 & 1 \\ 0 & 0 & 0 \end{pmatrix} \qquad F_- = \sqrt{2}\begin{pmatrix} 0 & 0 & 0 \\ 1 & 0 & 0 \\ 0 & 1 & 0 \end{pmatrix} \qquad F_z = \begin{pmatrix} 1 & 0 & 0 \\ 0 & 0 & 0 \\ 0 & 0 & -1 \end{pmatrix}$$

$$\psi^\dagger F_+\psi = \sqrt{2}\left(\psi^\dagger_+\psi_0 + \psi^\dagger_0\psi_-\right) \qquad \psi^\dagger F_-\psi = \sqrt{2}\left(\psi^\dagger_0\psi_+ + \psi^\dagger_-\psi_0\right) \qquad \psi^\dagger F_z\psi = \psi^\dagger_+\psi_+ - \psi^\dagger_-\psi_-$$

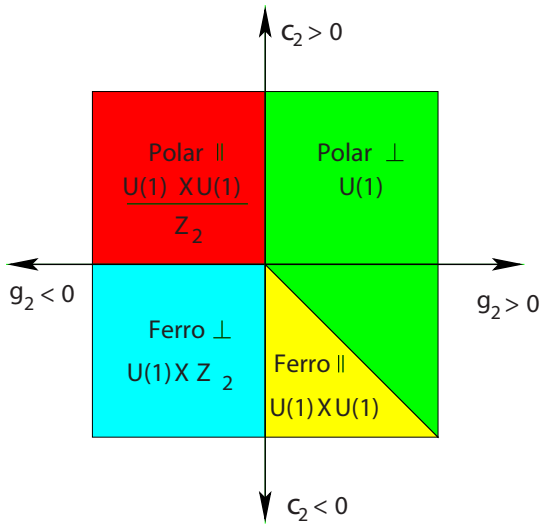

Figure 4.1: Mean-field phase diagram of a spinor condensate in the presence of a magnetic field. The symmetry classification is labelled for each phase. The experiments in this thesis are performed in the longitudinal ferromagnetic phase. The figure is from Ref. 41.

In there spherical basis, $\vec{F}\cdot\vec{F} = F_zF_z + \frac{1}{2}(F_+F_- + F_-F_+)$.

$$H_S = \frac{c_2}{2}\left(\psi_+^\dagger\psi_+^\dagger\psi_+\psi_+ + \psi_-^\dagger\psi_-^\dagger\psi_-\psi_- - 2\psi_+^\dagger\psi_-^\dagger\psi_+\psi_- + 2\psi_+^\dagger\psi_0^\dagger\psi_+\psi_0 + 2\psi_0^\dagger\psi_-^\dagger\psi_0\psi_- + 2\psi_+^\dagger\psi_-^\dagger\psi_0\psi_0 + 2\psi_0^\dagger\psi_0^\dagger\psi_+\psi_-\right) \tag{4.2}$$

The first line of Eq. 4.2 contains the spin-conserving terms, which encompass the various ways that components of the wave function can acquire phase shifts from the presence of other components. The second line includes the spin-changing terms that allow for two $m_F = 0$ atoms to coherently scatter into an $m_F = +1$ and $m_F = -1$ atom. During a quench experiment, this term allows the system to evolve from the polar state to the ferromagnetic state [42].

Oftentimes we are most interested in dynamics where the $|m_F = +1\rangle$ state is negligbly populated. The scattering length between $m_F = -1 \leftrightarrow m_F = -1$ and $m_F = -1 \leftrightarrow m_F = 0$ is identical but differs from $m_F = 0 \leftrightarrow m_F = 0$.

$$\begin{aligned} H_{int} =& \frac{c_0 + c_2}{2}\left(\psi_+^\dagger\psi_+^\dagger\psi_+\psi_+ + 2\psi_+^\dagger\psi_0^\dagger\psi_+\psi_0\right) + \frac{c_0}{2}\psi_0^\dagger\psi_0^\dagger\psi_0\psi_0 \\ =& \frac{c_0 + c_2}{2}\left(\psi_+^\dagger\psi_+ + \psi_0^\dagger\psi_0\right)^2 - \frac{c_2}{2}\psi_0^\dagger\psi_0^\dagger\psi_0\psi_0 \end{aligned}$$

From Eq. 4.2, we can calculate the Schrödinger equation $i\hbar\dot{\psi}_\alpha = \partial H/\partial\psi_\alpha^\dagger$.

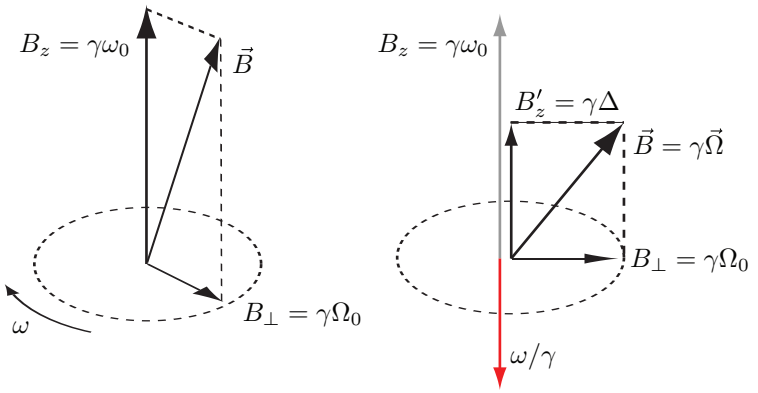

Figure 4.2: Rotating frame diagram for a spin-1/2 particle. They gyromagnetic ratio $\gamma = \mu/\hbar$ is the ratio between magnetic fields and frequencies. The laboratory frame with a field rotating at frequency ω (left) is equivalent to a rotating frame (right) where the z component of the magnetic field is reduced by ω/γ. The Rabi frequency vector $\vec{\Omega} = (\mathrm{Re}[\Omega_0], \mathrm{Im}[\Omega_0], \Delta)$ can generally point in any direction, though it is common to let Ω_0 point along the y axis.

$$\begin{aligned} i\hbar\dot{\psi}_{+1} = & -\frac{\hbar^2}{2m}\nabla^2\psi_{+1} + c_0\left(\psi^\dagger_{+1}\psi_{+1} + \psi^\dagger_0\psi_0 + \psi^\dagger_{-1}\psi_{-1}\right)\psi_{+1} \\ & + c_2\left[\left(\psi^\dagger_{+1}\psi_{+1} + \psi^\dagger_0\psi_0 - \psi^\dagger_{-1}\psi_{-1}\right)\psi_{+1} + \psi^\dagger_{-1}\psi_0\psi_0\right] \qquad (4.3a) \\ i\hbar\dot{\psi}_0 = & -\frac{\hbar^2}{2m}\nabla^2\psi_0 + c_0\left(\psi^\dagger_{+1}\psi_{+1} + \psi^\dagger_0\psi_0 + \psi^\dagger_{-1}\psi_{-1}\right)\psi_0 \\ & + c_2\left[\left(\psi^\dagger_{+1}\psi_{+1} + \psi^\dagger_{-1}\psi_{-1}\right)\psi_0 + 2\psi^\dagger_0\psi_{+1}\psi_{-1}\right] \qquad (4.3b) \\ i\hbar\dot{\psi}_{-1} = & -\frac{\hbar^2}{2m}\nabla^2\psi_{-1} + c_0\left(\psi^\dagger_{+1}\psi_{+1} + \psi^\dagger_0\psi_0 + \psi^\dagger_{-1}\psi_{-1}\right)\psi_{-1} \\ & + c_2\left[\left(\psi^\dagger_{-1}\psi_{-1} + \psi^\dagger_0\psi_0 - \psi^\dagger_{+1}\psi_{+1}\right)\psi_{-1} + \psi^\dagger_{+1}\psi_0\psi_0\right] \qquad (4.3c) \end{aligned}$$

In Sec. 5.1.1, we will linearize this set of equations for a ferromagnetic spinor condensate and find two classes of excitations, phonons and magnons.

4.1.5 Two- and three-level Rabi spectroscopy

It is helpful to introduce basic Rabi spectroscopyhere. If we have an isolated two-level atom, the Hamiltonian depends on the energy difference $\hbar\omega_0$ between the two states: $H_{\text{isolated}} = \frac{1}{2}\hbar\omega_0\sigma_z$. An applied transverse field can change the eigenstates of the atom, but in most cases the magnitude of the applied field we can experimentally realize is much smaller than ω_0. The experimental solution is to resonantly oscillate the transverse field at a frequency ω near ω_0.

$$H = \frac{1}{2}\hbar\omega_0\sigma_z + \hbar\Omega_0\left(\sigma_x\cos\omega t + \sigma_y\sin\omega t\right)$$

The solutions to this time-dependent Hamiltonian are well known [43]. In summary, we can turn this into a time-independent problem by "boosting" into the rotating frame as defined by the unitary operator $R = e^{i\sigma_z \omega t/2}$. In this frame, we define $|\psi_R\rangle = R|\psi\rangle$ and $H_R = RHR^\dagger + i\hbar \dot{R} R^\dagger$. See Fig. 4.2 for a graphical depiction.

$$H_R = \frac{\hbar}{2}\begin{pmatrix} \Delta & \Omega_0 \\ \Omega_0^* & -\Delta \end{pmatrix} \qquad \Delta = \omega - \omega_0 \qquad R = \begin{pmatrix} e^{i\omega t/2} & 0 \\ 0 & e^{-i\omega t/2} \end{pmatrix}$$

In general, the parameter ω is a known precise frequency referenced to a laboratory time source, whereas ω_0 and Ω_0 need to be determined experimentally.

S=1 representation

Rotations of a spin-1 object are slightly more complicated than the usual spin-1/2 case. In most situations we deal with rotations of a fully magnetized spin. In the $|m_F\rangle$ basis, rotations about the y axis are described by the Wigner d-matrix.

$$e^{i\theta F_y/\hbar} = \begin{pmatrix} \frac{1}{2}(1+\cos\theta) & -\frac{1}{\sqrt{2}}\sin\theta & \frac{1}{2}(1-\cos\theta) \\ \frac{1}{\sqrt{2}}\sin\theta & \cos\theta & -\frac{1}{\sqrt{2}}\sin\theta \\ \frac{1}{2}(1-\cos\theta) & \frac{1}{\sqrt{2}}\sin\theta & \frac{1}{2}(1+\cos\theta) \end{pmatrix}$$

$$R(\phi,\theta,\gamma)\begin{pmatrix} 1 \\ 0 \\ 0 \end{pmatrix} = e^{-i\gamma}\begin{pmatrix} e^{-i\phi}\frac{1}{2}(1+\cos\theta) \\ \frac{1}{\sqrt{2}}\sin\theta \\ e^{i\phi}\frac{1}{2}(1-\cos\theta) \end{pmatrix} \qquad R(\phi,\theta,\gamma)\begin{pmatrix} 0 \\ 1 \\ 0 \end{pmatrix} = \begin{pmatrix} -e^{-i\phi}\frac{1}{\sqrt{2}}\sin\theta \\ \cos\theta \\ e^{i\phi}\frac{1}{\sqrt{2}}\sin\theta \end{pmatrix}$$

When calibrating a Rabi frequency, it is most convenient to monitor the difference between $m_F = +1$ and $m_F = -1$ populations. In Stern-Gerlach imaging (Sec. 4.2.1) and ASSISI (Sec. 4.2.3), we measure $N_{m_F} = N_0|\langle m_F|\psi\rangle|^2$

$$\langle F_z\rangle = \frac{N_{+1} - N_{-1}}{N_{+1} + N_0 + N_{-1}} = \cos\theta$$

The three populations N_{m_F} provided redundant information for a fully magnetized sample. In ASSISI, this redundancy can calibrate that the microwave pulse power for the $m_F = 0$ populations with the relation $N_0^2 = 4N_{+1}N_{-1}$.

4.2 Imaging

Nearly everything we learn from an ultracold atom experiment involves shining a laser into one viewport of a vacuum chamber and examining the light that leaves through another viewport. We learn about the evolution or distribution of atomic spins by coupling the spin to the atoms' position (Stern-Gerlach imaging), to a phase shift of light (dispersive imaging), or to the absorption light (absorptive spin-sensitive imaging). In this section I will describe these three main techniques we use to image atomic spin, momentum, and position. The main result is absorptive spin-sensitive *in situ* imaging (ASSISI), a new technique we developed to obtain multiple high signal-to-noise images of spin dynamics.

4.2.1 Stern-Gerlach Time-of-Flight Imaging

The simplest and most common form of spin imaging is to separate spins with a Stern-Gerlach experiment during free expansion (time-of-flight). Like the classic Stern-Gerlach experiment [44], atoms in a magnetic field gradient will feel a force depending on the projection of their spin states. For a distribution of particles $n(x, p, \vec{F})$ in position-momentum-spin space, a time-of-flight expansion in a weak magnetic field gradient leads to a convolution of those coordinates ($\langle P_{m_F} \rangle$ is the projection of the spin along the m_F and we will neglect coherences).

$$n(x) = \sum_{m_F} \int dx'\, dp\, n(x', p, \vec{F})\, \delta\left(x - x' - \frac{pt}{m} - \frac{g\mu_B m_F \langle P_{m_F} \rangle B' t^2}{\hbar m}\right)$$

This technique is easy to implement and robust. It is a powerful diagnostic of the overall dynamics because it probes all m_F populations, not just the overall magnetization. However, it can lack spatial resolution because it relies on a time-of-flight separation, during which small features are blurred during the expansion due to dispersion or collisions. While blurring due to dispersion can be remedied by applying a large gradient, a more fundamental problem is that the measurement is destructive (with a few exceptions, e.g. Ref. 45).

Regardless, this is a favorite quick-and-dirty technique that is fairly robust against many experimental mistakes. We used it to first observe microwave and RF resonances, as an initial calibration of the magnetic field and gradients, and to debug the other imaging techniques.

4.2.2 Polarization contrast imaging and its limitations

Ultracold gases typically have an optical density much greater than one. This is both a blessing and a curse. Historically, experiments use time-of-flight expansion to reduce the optical density to a level where absorption imaging works effectively. *In situ* absorption imaging has difficulty because only a feeble amount of light can penetrate the optically thick gas. This can be recovered by imaging at very high intensity [46] or reducing the optical density with a microwave pulse (Sec. 4.2.3) or an off-resonant laser (Sec. 3.3).

Dispersive imaging techniques allow for *in situ* and repeated density measurements of an optically thick ultracold sample. The operating principle is that an off-resonant laser acquires a phase shift after passing through an atomic sample. In other words, the condensate appears as a weak lens to an off-resonant laser. This phase shift is typically measured against a reference laser in a homodyne setup. Much of the experimental cleverness arises from constructing the interference in a robust manner. The classic approach is phase contrast imaging, in which the unscattered light is phase shifted relative to the forward scattered light [5, 47, 48].

We use polarization contrast imaging, in which we measure a differential phase shift between the two circular polarizations of light [5], essentially a position-dependent Faraday-rotation measurement. The polarization axis of a linearly polarized laser is rotated by the circular birefringence of the atoms, and that rotation is determined by passing it through a polarization beamsplitter. This process requires that the ultracold gas break

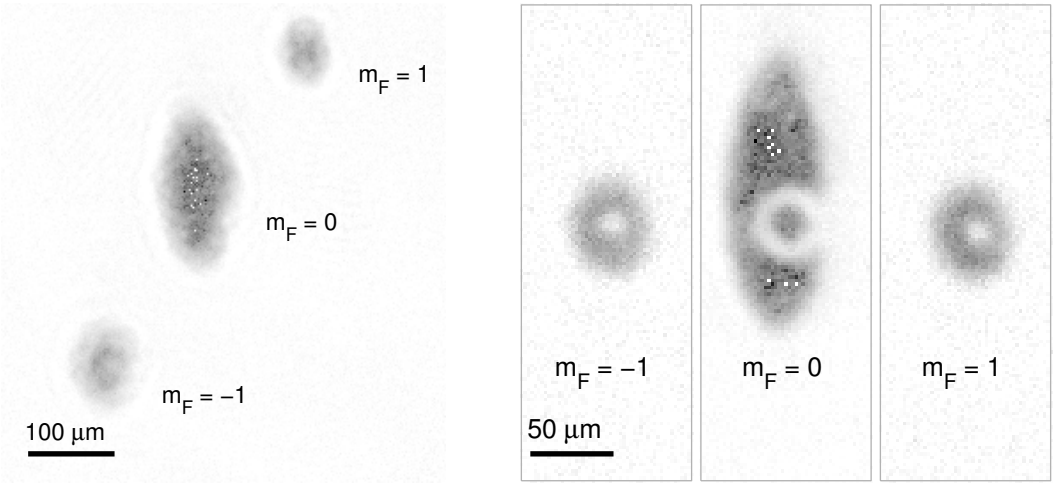

(a) (b)

Figure 4.3: Our first attempt at creating a polar skyrmion, a topological vortex in an $m_F = 0$ condensate. (a) Stern-Gerlach separation shows the three populations, and clearly the $m_F = \pm 1$ density is smaller than the $m_F = 0$ density. The images are unnecessarily saturated. (b) With *in situ* imaging, we can see the sharp torus in the $m_F = \pm 1$ density. While these images were taken from separate realizations, we later were able to image multiple spin projections of the same sample.

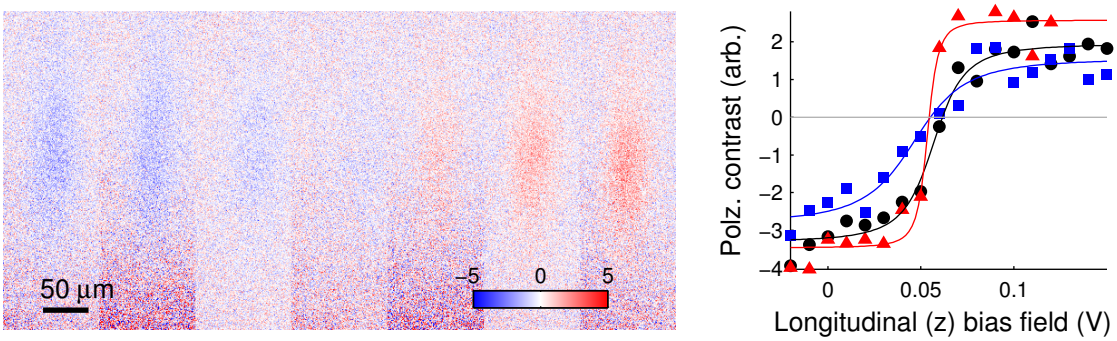

(a) (b)

Figure 4.4: Calibrating the magnetic field orientation with polarization contrast imaging. (a) The sign of the polarization contrast signal reverses as the magnetic field is oriented towards or away from the imaging axis z. For an in-plane field, the signal disappears. Each image is taken at a different value of the z component of a magnetic field. (b) We characterize the transverse field and zero the z component of the magnetization by integrating the polarization contrast signal. Each scan corresponds to a different transverse field setting. The light level is sufficient to destroy the sample, despite the meager signal-to-noise. These images are taken detuned +80 MHz from the D2, $F = 1 \rightarrow F' = 2$ transition.

time reversal symmetry, and so can only be used to measure a magnetized sample with a detuning where the atoms are strongly circular birefringent. A good discussion on dispersive

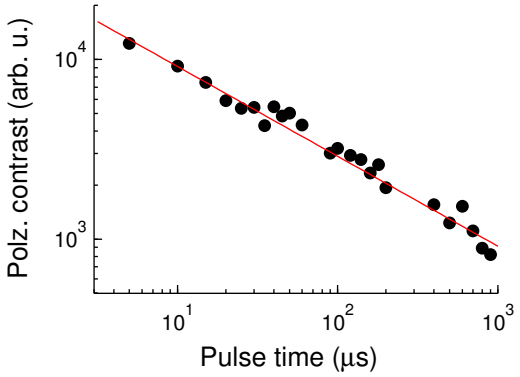

Figure 4.5: Polarization contrast signal versus pulse time. The fit assumes signal proportional to $t^{1/2}$ for reasons which are unclear to me. Detuning is +80 MHz from the D2, $F = 1 \rightarrow F' = 2$ transition.

imaging can be found in Ref. 5, 47, 48.

We originally used polarization contrast imaging to align the magnetic field in the plane of the light sheet, transverse to the vertical imaging axis (Fig. 4.4). The BEC is prepared in the $|F = 1, m_F = -1\rangle$ state with a magnetization antiparallel to the local field. If the magnet field has a small component along the imaging laser, the laser polarization is Faraday rotated and we detect a signal. However, as can be seen from the images in Fig. 4.4a, the images have a poor signal-to-noise ratio. These data were taken with a laser tuned near the D2 line with an Eagleyard 780nm DFB frequency offset lock from the master laser. For a reason we do not completely understand, the signal strength decreased with the square root of the imaging pulse time (Fig. 4.5).

It was our original intention to use polarization contrast imaging to study spinors. We started looking at spin vortices, which are topological structures whose center has a magnetization of opposite direction as the edge. However, our optical density was much lower than previous experiments in the group had a correspondingly worse signal-to-noise ratio. As shown in the next section, we fixed this problem with a novel technique, absorptive spin-sensitive *in situ* imaging.

Before burying polarization contrast imaging, we should praise it. One important advantage of polarization contrast imaging is that it lends itself to AC measurements. The polarization contrast signal can be reversed by reversing the atomic magnetization, the magnetic field orientation, the imaging polarization, or changing the detuning. This was used to great effect in earlier work by the Stamper-Kurn group, where an oscillating polarization contrast was created by Larmor precession. The polarization contrast signal vanishes when the atomic magnetization is transverse to the imaging beam, even if the polarization or other parameters are not properly calibrated or set.

Fundamental Limits

Dispersive imaging is not non-destructive; it should instead be advertised as "minimally destructive". The refraction and scattering of light by atoms in free space are linked

and limit the amount of information that we can glean from linear optics. The typical solution is to use a high optical density where the atom loss rate is tolerable. In the original Berkeley spinor experiment, good signal-to-noise images required condensates of 2-3 million atoms. Our setup was initially able to produce only several 10^5 atoms and achieved lower optical density, and so our dispersive images have significantly lower signal-to-noise than can be found in older spinor papers.

Moreover, dispersive techniques in alkali gases cannot easily access the polar degrees of freedom because the linear birefringence is associated with a high optical scattering rate. For a polar condensate, a rotation of $m_F = 0$ will create an equal superposition of $m_F = \pm 1$ states, for instance $|m_F = +1\rangle \pm |m_F = -1\rangle$. Polarization contrast imaging based on circular birefringence cannot differentiate between these states.

We can understand the limitation of dispersive imaging with a simple model of a two-level atom. In dispersive imaging, a weak, far-detuned laser is phase shifted by the presence of atoms. The presence of atoms is measured from the phase shift between the probe laser and a reference beam. Our key assumption is that an atom is lost after it has scattered a single photon, since the recoil energy is typically much higher than the condensation temperature. Each imaging pulse boils out a certain number of atoms, with a tradeoff between losing atoms and acquiring information.

What is the signal-to-noise ratio of detecting a single atom before it has scattered one photon? In the far-detuned limit, one atom (linewidth Γ, resonant cross section σ_0) will phase shift a laser (detuning Δ, cross sectional area A) by $\phi_1 = \sigma_0\Gamma/(2A\Delta)$. Since the atom scatters a fraction $\sigma_0\Gamma^2/A\Delta^2$ of the photons, we can apply a pulse of up to $N_{\text{photon}}^{\max} = A\Delta^2/\sigma_0\Gamma^2$ photons before the atom, on average, scatters one photon. Our uncertainty in atom number after this pulse is

$$\Delta N_{\text{atom}} = \frac{\Delta\phi}{\partial\phi/\partial N_{\text{photon}}} = \frac{1}{\phi_1\sqrt{N_{\text{photon}}^{\max}}} = 2\sqrt{\frac{A}{\sigma_0}}$$

Optical diffraction limits $A > \sigma_0$ and we find that we cannot determine the presence of a single atom before it has scattered a photon. This result holds for free-space linear optics in general: a mutlilevel atom with complex polarizability α will have $N_{\text{photon}}^{\max} = A/\sigma$ and $\phi_1 = \frac{k}{A\epsilon_0}\text{Re}[\alpha]$, where $k = \omega/c$ is the wavevector of the incident light. The uncertainty in atom number is now

$$\Delta N_{\text{atom}} = \sqrt{\frac{Ak^2}{6\pi}}\frac{|\alpha|}{|\text{Re}[\alpha]|}.$$

We again find that $\Delta N_{\text{atom}} > 1$ because $|\alpha| \geq |\text{Re}[\alpha]|$ and the diffraction limit requires $Ak^2 > 1$. It is worth noting that it is possible to reach or surpass the atom-shot-noise limit in dense samples when $1 < \Delta N_{\text{atom}} \leq \sqrt{N}$.

If we want improved spin imaging, we must break an assumption of this derivation. This can be done by (1) placing the atom in an optical cavity and changing the scattering rate of the atom or (2) avoiding linear optics. We do the latter by 'electron shelving', whereby a small fraction of the atoms scatter a large number of photons and the rest of the atoms are unperturbed.

When imaging magnetization, the signal depends on the differences in polarizability between internal states (or, equivalently, the change of polarizability with optical polarization). A stricter practical limitation is placed by superradiant scattering. Special precautions must be taken to minimize the build up of superradiance, including (1) orienting the linear polarization of the laser along the longest condensate axis to suppress Rayleigh scattering, (2) detuning to the blue of resonance to suppress Rayleigh superradiance, and (3) applying a simultaneous pulse resonant to the D2, $F = 2 \rightarrow F' = 3$ transition to dephase atoms Raman scattered to $F = 2$.

4.2.3 Absorptive spin-sensitive *in situ* imaging (ASSISI)

We circumvent the inherent limitations to dispersive imaging by employing a three-level scheme to image the $F = 1$ spin density (Fig. 4.6). First, a brief microwave pulse transfers a small number of atoms from one spin state in the $F = 1$ manifold to the $F = 2$ manifold. A weak magnetic field is sufficient to spectroscopically separate microwave transitions (Sec. 4.3.1). Then, the atoms in the $F = 2$ states are imaged with a short, intense pulse of resonant imaging light on the D2, $F = 2 \rightarrow F' = 3$ transition, to which the $F = 1$ condensate is dark. In our setup, each imaged atom typically scatters 300 photons, hence we can extract much more information per atom than the limit of one scattered photon per atom in dispersive imaging. We reach a high signal-to-noise ratio by destructively imaging a small fraction of the sample. The theoretical uncertainty in atom counting $\Delta N = \sqrt{16A/\sigma_0\Gamma t}$ (see Eq. A.5) can exceed unity for a large number of scattered photons $\Gamma\tau \gg 1$ even far from the diffraction limit ($A > \sigma_0$). For our system ($\tau = 30$ μs), the column density noise $\Delta\tilde{n} = 0.4/\sqrt{\mu\text{m}^2}$ is far smaller than the peak column density $\tilde{n}_0 = 340/\mu\text{m}^2$.

This technique combines the best features of Stern-Gerlach imaging and polarization contrast. ASSISI can image all m_F states with absorption imaging, like Stern-Gerlach, but does so with a lower atom loss than even polarization contrast imaging. This allows us to image the evolution of structures that arise in polar condensates (e.g., Fig. 4.3), which would be completely dark in circular birefringence polarization contrast imaging. ASSISI probes strictly along the quantization axis, while polarization contrast measures magnetization along the propagation direction of the laser.

A clear example is shown in Fig. 4.7. The polarization contrast image (Fig. 4.7a) is taken at our optimized "best" settings (detuned from the D1 line), but unfortunately at a light level sufficient to destroy the sample. Using ASSISI (Fig. 4.7b), we image only a small fraction (<10%) of the sample and yet have an enormous signal to noise – these images have no digital smoothing, binning, or filtering. The three images correspond to three microwave pulses on the $|F = 1, m_F\rangle \rightarrow |F = 2, m_F\rangle$ with small transferred fractions. Imaging a larger fraction of the spins is detrimental as the signal-to-noise decreases with high optical density. As emphasized earlier, the absorption imaging is done with an imaging pulse at the saturation intensity, which gives optimal signal-to-noise when the optical density of the transferred population is small.

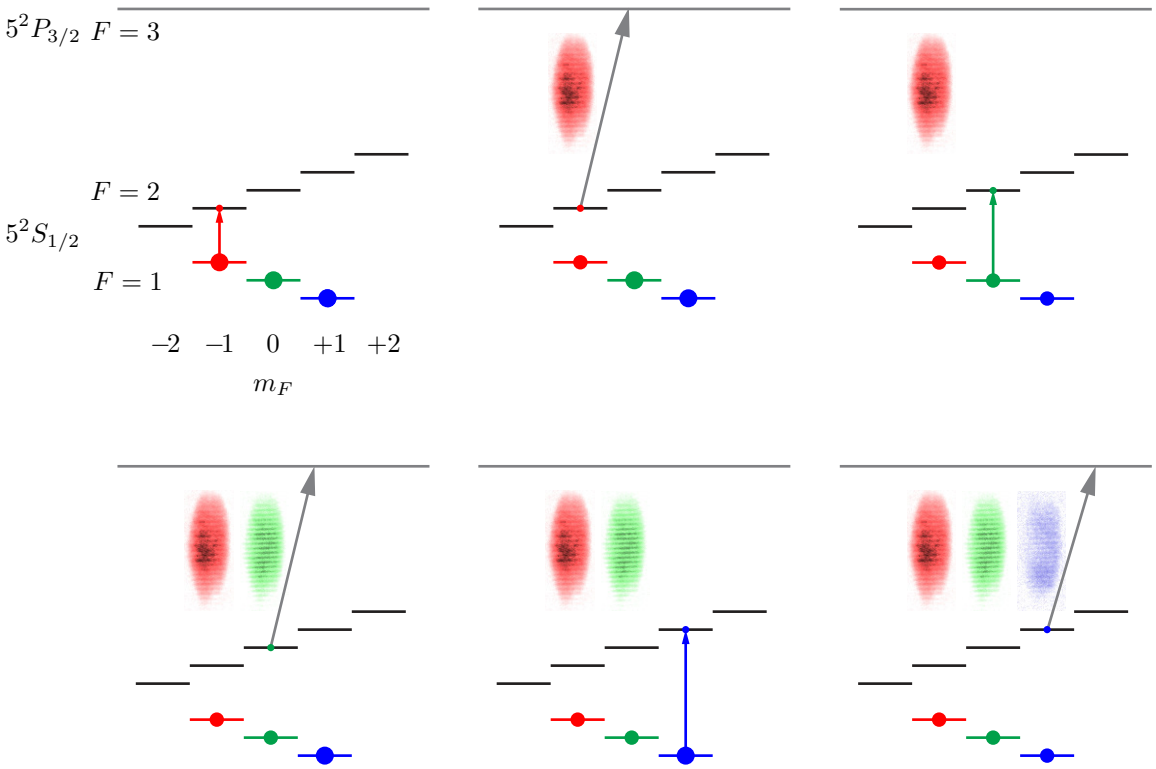

Figure 4.6: ASSISI scheme to read out the three projections of F_z with interleaved microwave and optical pulses. First, a calibrated pulse resonant with $|F = 1, m_F = -1\rangle \rightarrow |F = 2, m_F = -1\rangle$ transfers a small fraction of atoms to $F = 2$. An imaging pulse destructively images the transferred atoms and pushes them out of the trap. Typically, the image is stored on the CCD in frame transfer mode. The process is repeated for $m_F = 0$ and $m_F = +1$ on the same condensate. Projections of the magnetization along other axes can be measured by following this sequence with an RF pulse and repeating the procedure.

Multiaxis magnetization

The sequence of three images described above can be extended by rotating the magnetization with an RF pulse. The first three pulses measure the longitudinal magnetization $m_z = -1, 0, 1$, where m_z denotes the projections of F_z. After a $\pi/2$ pulse, the next three images measure the projections $m_x = -1, 0, 1$ (Fig. 4.8). For ferromagnetic structures, this is a redundant set of information, as we are most interested in the magnetization $M_z = N_{m_z=+1} - N_{m_z=-1}$ and $M_x = N_{m_x=+1} - N_{m_x=-1}$. Fig. 4.8 demonstrates a sequence of six images, each separated by 2 ms, and two magnetizations. From these images we can calculate M_y up to a sign.

We extend these measurements to nine pulses, three triplets separated by two RF pulses (Figs. 4.9, 4.10). Like above, we refer to the first two triplets as the z and x axis of magnetization. If the final RF pulse occurs after an integer plus or minus a quarter number of Larmor cycles, the magnetization will be rotated along y or $-y$. Spin echo pulses can help ensure this, but we instead rely on chance. Insofar that our RF $\pi/2$ pulses are trustworthy,

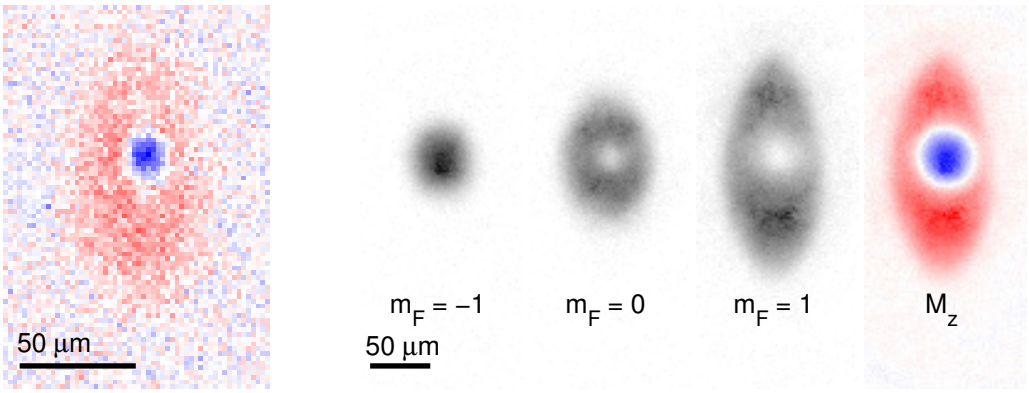

Figure 4.7: (a) Polarization contrast and (b) *in situ* spin images of a ferromagnetic skyrmion. The magnetization image M_z is the difference between the $m_F = 1$ and $m_F = -1$ populations.

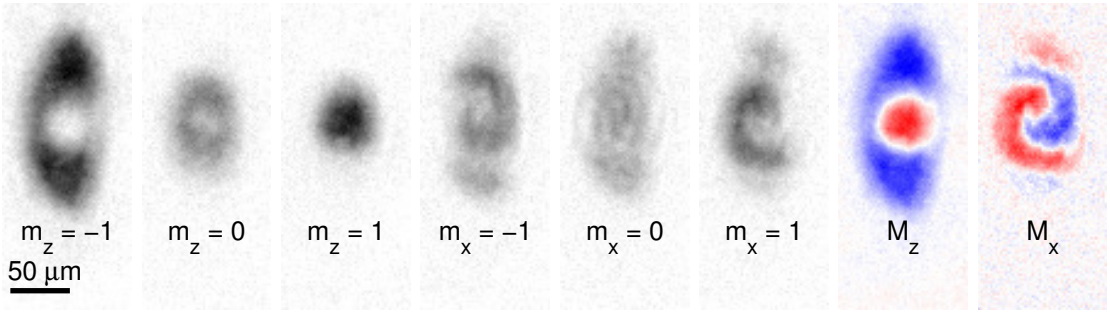

Figure 4.8: Multiaxis magnetization imaging of a topological structure. The first three images measure the longitudinal magnetization, i.e. the projection of the magnetization along the quantization axis $\hat{z}$, as in Fig. 4.7b. We then apply an RF $\pi/2$ pulse to rotate the magnetization by 90° and repeat the original procedure. These images constitute the transverse magnetization, we we arbitrarily label the axis $\hat{x}$. All images are from a single experimental realization and probe the magnetization of the same structure.

the final magnetization ends up along the $y-z$ plane, and we fit for both the RF pulse angle and the free evolution angle from the images by either correlating the images or solving for the angles that maximize $|\langle \vec{F} \rangle|$, since we assume the magnetization is maximal for these ferromagnetic structures. Figs. 4.9 and 4.10 show close to the ideal angle because they are post-selected from a set of repeated experiments on independent samples.

The large dataset of nine images allows us to extract topological parameters from the data, in this case the solid angle swept out by the magnetization. Topological invariants give us a means to solve yes or no questions. For a two-dimensional magnetic system, if the system has fixed uniform magnetization along a boundary, can that magnetization be continuously unwrapped to a uniform magnetization inside the region? The answer can be determined by integrating the solid angle swept out by the local magnetization, where the solid angle is positive for magnetization that rotates counter-clockwise.

$$\Omega = \int dx\, dy\, \vec{m} \cdot \left(\frac{\partial \vec{m}}{\partial x} \times \frac{\partial \vec{m}}{\partial y} \right)$$

If $\Omega = 0$, then the magnetization inside the region can be continuously unwrapped to a constant vector. Otherwise, the region contains a topological defect. In this example of a uniformly magnetized boundary, Ω must be a multiple of 4π, so continuous deformations cannot let it 'jump' from one value to the next. The integrand is often called the topological density, Pontryagin density [49, sec. 1.19], or Berry curvature. Ω is the number of times the magnetization wraps a sphere times 4π, and is closely related to the second homotopy group, the group of equivalent ways to wrap a sphere around the order parameter space.

The discretized version involves calculating the solid angles swept out by two triangles for each 2×2 grid of points. The lower triangle has points $1 = (x, y)$, $2 = (x+1, y)$, and $3 = (x, y+1)$, and the upper triangle $1 = (x+1, y+1)$, $2 = (x, y+1)$, and $3 = (x+1, y)$. It is important to use the exact formula for solid angle to avoid building up numerical errors [50].

$$\tan \frac{\Omega}{2} = \frac{|\vec{m}_1 \vec{m}_2 \vec{m}_3|}{|\vec{m}_1||\vec{m}_2||\vec{m}_3| + \vec{m}_1 \cdot \vec{m}_2\, |\vec{m}_3| + \vec{m}_2 \cdot \vec{m}_3\, |\vec{m}_1| + \vec{m}_3 \cdot \vec{m}_1\, |\vec{m}_2|}$$

Fig. 4.9 shows the magnetization for a spin vortex with a topologically nontrivial structure (spin vortex). The nine consecutive images are shown in black and white, along with the three estimates of the spin projection $F_i = M_i/N$. Unfortunately, the core is quite small and the finer structures are poorly resolved. In particular, the F_x and F_y images have lower contrast than they should, and the $m_F = 0$ images are quite smeared. This is exacerbated by evolution of the magnetization during the 16 ms acquisition time, since our microwave source requires 2 ms to switch frequencies. Regardless, the measured $\Omega = -12.5$ is unusually close to the expected value of 4π.

By comparison, a spin helix has a small integrated solid angle and occupies a small fraction of the magnetization sphere (Fig. 4.10). This analysis works despite the non-uniform boundary of the chosen region.

4.3 Experimental manipulation and control

For an experimentalist, control covers both the aspects that must be managed for the system to work and the aspects that can be dialed to see new science, with considerable overlap between those categories.

4.3.1 Microwave Manipulation

The physics that we are interested in involves placing atoms in a superposition of the three $F = 1$ states. As mentioned above, we use the microwaves to coherently transfer atoms from the $F = 1$ states to the $F = 2$ states. We do this to image the atoms and to measure the local magnetic field. We must calibrate the Rabi frequency of the microwave transitions for this manipulation. Characterizing our microwave setup involves checking

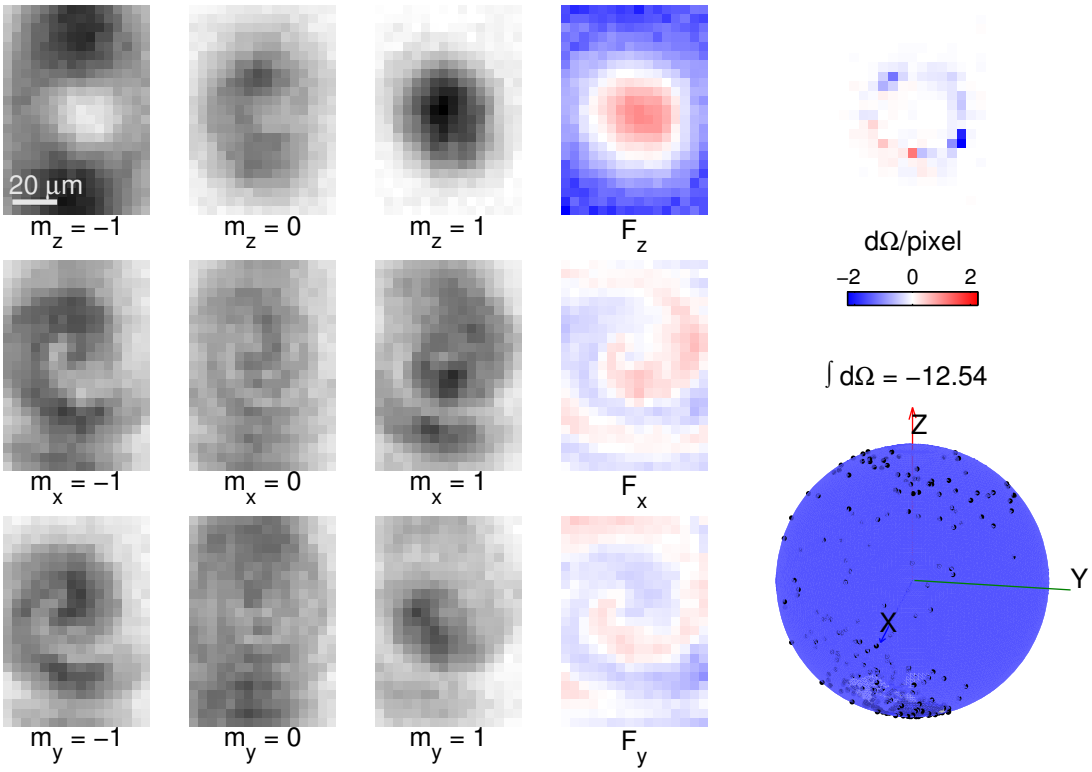

Figure 4.9: Full magnetization and topological imaging of a spin vortex. Nine images of the $m_i = -1, 0, 1$ projections for $i = x, y, z$ are used to calculate the three estimates of the spin project F_i. (Top right) The solid angle encompassed by each 2×2 square of pixels is shown on the top right; most circle the magnetization clockwise (blue). (Bottom right) The magnetization sphere. Each triplet (F_x, F_y, F_z) is projected onto a sphere (black dots). Blue and red regions denote regions of the magnetization sphere covered by the images.

the detuning of the clock transition, of the magnetic-field sensitive transition, and the Rabi frequency.

For microwave evaporation, we mix a Microwave Dynamics PLO-4000 at 7.000 GHz with National Instruments PXI-5650 RF signal generator. However, we found that the PLO-4000 was far too noisy, most likely because the phase locked loop was poorly calibrated and introduced large reference spurs. In particular, it failed two experiments. (1) When a strong microwave tone ($\Omega_0 \approx 5$ kHz) was applied to our atoms with a detuning of 40 kHz for one second, we saw substantial excitation of the atoms, much more than the expected fraction of $(\Omega_0/\Delta)^2 \approx 1\%$ (Fig. 4.11). (2) The measured frequency of the clock transition ($|F = 1, m_F = 0\rangle \to |F = 2, m_F = 0\rangle$) disagreed with the literature by an abnormally large 1 kHz. Substituting the source for an Agilent MXG 5183A immediately solved both problems. All following calibrations and data was taken with the Agilent, including all imaging pulses. Both systems are referenced to a commercial, free-running rubidium clock (Stanford Research Systems FS725).

The frequency of the clock transition ($|F = 1, m_F = 0\rangle \to |F = 2, m_F = 0\rangle$) has

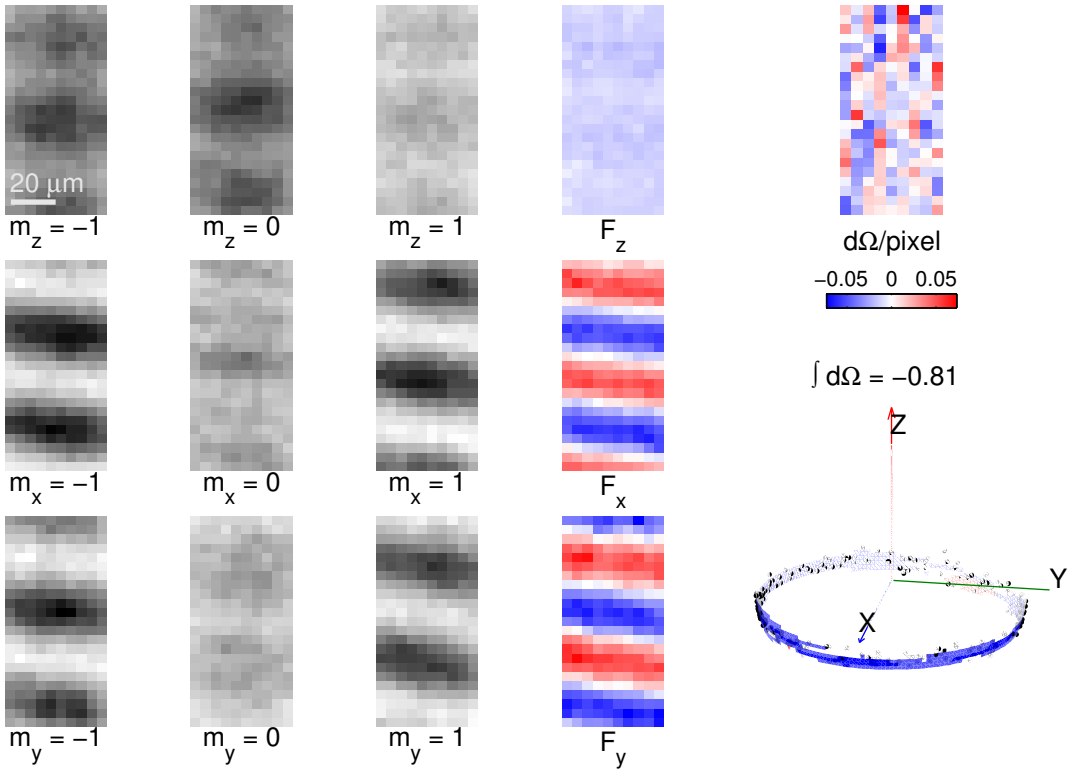

Figure 4.10: Full magnetization and topological imaging of a spin helix. Nine images of the $m_i = -1, 0, 1$ projections for $i = x, y, z$ are used to calculate the three estimates of the spin project F_i. (Top right) The solid angle encompassed by each 2×2 square of pixels is shown on the top right. The solid angles are noisy but average to zero. (Bottom right) (Bottom right) The magnetization sphere. Each triplet (F_x, F_y, F_z) is projected onto a sphere (black dots). Blue and red regions denote regions of the magnetization sphere covered by the images. For a spin helix, all of the points occur on a band at fixed latitude.

been measured exceptionally well [16]. We can verify the literature value by reducing the microwave power by 24 dBm and measuring the Rabi oscillation frequency Ω at several detunings (Fig. 4.12). The expected model $\Omega = \sqrt{\Omega_0^2 + (f - f_0)^2}$ fits the data very well with a deviation of +21 Hz. This disagrees with my expectation from the quadratic Zeeman effect (+26 Hz), the optical trap (-3 Hz), and atom-atom interactions (-13 Hz). However, it is close enough for comfort. For coherent manipulation, we increase the Rabi frequency by maximizing our microwave power (see Fig. 4.13). The Rabi oscillations are clean and allow for good π pulses between these levels.

To make the same fraction of each spin state, the Rabi frequency of the three microwave pulses must be equal. We use the $\Delta m_F = 0$ microwave transition ($|F = 1, m_F\rangle \rightarrow |F = 2, m_F\rangle$) so that the Rabi frequencies depend on the same component of microwave polarization and are related by Clebsch-Gordan coefficients. The Rabi frequency for $m_F = -1$ and $m_F = +1$ are identical, even for a finite detuning. We increase the power of the microwaves when we image the $m_F = 0$ population to match the larger Clebsch-Gordan

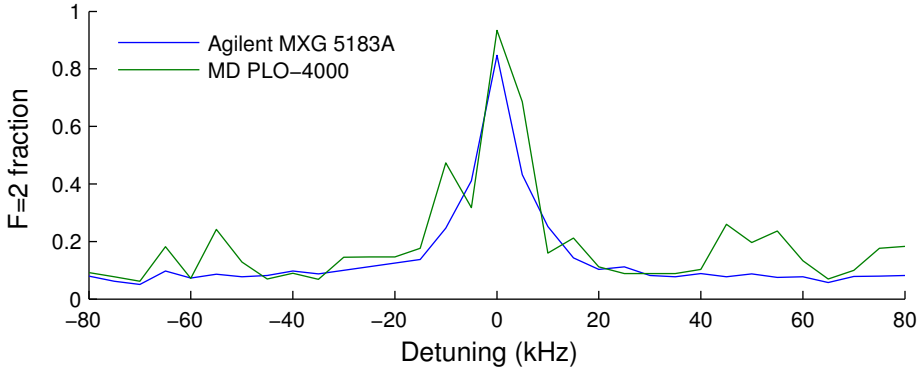

Figure 4.11: Atoms as a narrowband microwave spectrum analyzer. Fraction of atoms excited to $F = 2$ after a long microwave pulse. Except around zero detuning, the MXG 5183A has uniformly low excitation, while the PLO-4000 has "bad" regions, especially around a detuning of 50 kHz. The large background offset is most likely due to residual atoms that were not removed during the preparation of the $|F = 1, m_F = 0\rangle$ condensate.

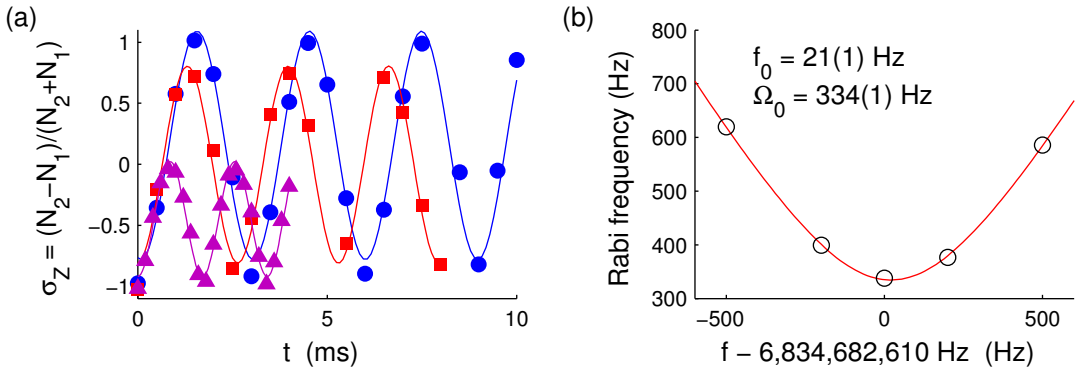

Figure 4.12: Calibrating the Rabi frequency and detuning of the clock transition. (a) Rabi oscillations of $|F = 1, m_F = 0\rangle \rightarrow |F = 2, m_F = 0\rangle$ clock transition for a detuning of 0 Hz (blue circles), 200 Hz (red squares), and 500 Hz (purple triangles). The power is reduced by 10 dBm compared to normal operation. (b) From the detuned Rabi frequencies, we can determine the resonant Rabi frequency and resonance frequency. The offset is primarily from the quadratic Zeeman shift.

coefficient $(4/3 = (\langle 1, 0; 1, 0|2, 0\rangle / \langle 1, 1; 1, 0|2, 1\rangle)^2)$. At one point we found that an increase of 1.04 dB seemed to match the Rabi frequencies better. Later analysis regularly showed too large of a population of $m_F = 0$, so this calibration is most likely incorrect.

These calibrations require an initial population of atoms in the $|F = 1, m_F = 0\rangle$ state. Our sequence always begins with atoms in the $|F = 1, m_F = -1\rangle$ state. For the calibrations shown in Fig. 4.13, the atoms were transferred to the $|F = 1, m_F = 0\rangle$ state with two Landau-Zener sweeps, first from $|F = 1, m_F = -1\rangle$ to $|F = 2, m_F = -1\rangle$ and a finally from $|F = 2, m_F = -1\rangle$ to $|F = 1, m_F = 0\rangle$. The sweeps are 15 ms and 20 ms, respectively, and use a constant microwave frequency and swept magnetic field. Purification

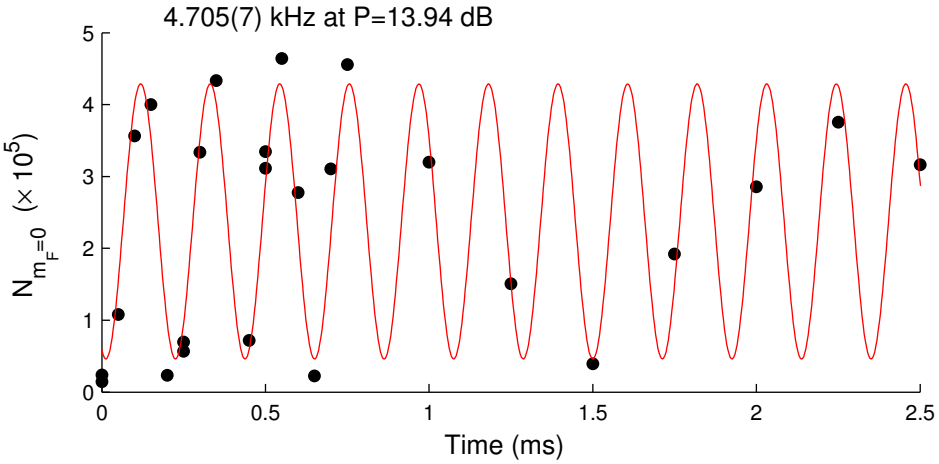

Figure 4.13: Rabi oscilations on the clock transition. Rabi oscillations of $|F = 1, m_F = 0\rangle \rightarrow |F = 2, m_F = 0\rangle$ clock transition.

follows with a large (several G/cm) magnetic field gradient and resonant imaging light to expel $F = 2$ atoms. For later calibration, e.g. Fig. 4.12, we instead applied an intense, resonant, and brief RF pulse that transfers only a small population of the atoms to the $|F = 1, m_F = 0\rangle$ state, and a negligible fraction to $|F = 1, m_F = +1\rangle$. The small fraction ensures that the final, imaged population will have a moderate optical density and will not saturate the imaging.

4.4 Magnetic Field Control

Magnetic field noise is ever present in the lab and must be controlled to produce a clean environment to study spinor physics. In the best of cases, magnetic fields can be controlled by (1) mu-metal shielding that minimizes external field fluctuations, (2) feedback from an external magnetic sensor to control the fields at the atoms, or (3) choosing an atom, atomic transition, or measurement scheme whose level or signal fluctuates negligibly with the ambient noise of the lab. In general we did not follow any of these approaches and simply resorted to frequently measuring the magnetic fields with the atoms and correcting the experiment manually: a graduate student feedback loop. Quite a lot of the data was taken at night when ambient magnetic field fluctuations were smaller. For most of the experiments reported here, reducing magnetic field gradients is critical even while the magnitude of the field is not.

4.4.1 Magnetic Bias Field

We use microwave transitions to calibrate the magnetic bias field daily or several times per day. Fig. 4.14 shows a typical scan of the magnetic-field sensitive microwave transition $|F = 1, m_F = -1\rangle \rightarrow |F = 2, m_F = -1\rangle$ via Rabi spectroscopy. A microwave pulse with fixed time and power but scanned frequency transfers a small fraction of the

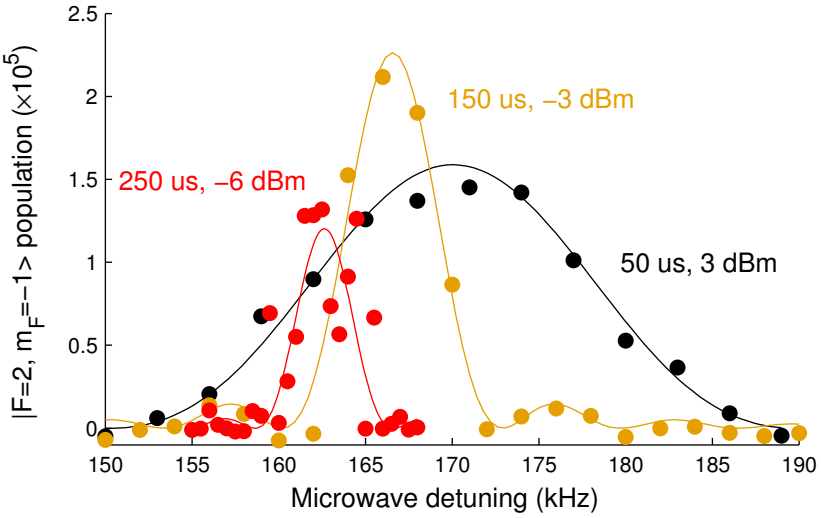

Figure 4.14: Calibrating the magnetic bias field with Rabi spectroscopy. Scans for the magnetic field from July 5, 2013 (black and orange) and July 13, 2013 (red). The drift of ∼5-10 kHz is typical. This transition has a frequency shift of $\mu_B B/h$, twice that of the Larmor frequency. Data is fit to Eq. 4.4.

sample to $|F = 2, m_F = -1\rangle$, which is subsequently imaged. This transition gives us a value very nearly twice the Larmor frequency $\omega_L = g_F \mu_B B/\hbar$, the splitting between $|F = 1, m_F = -1\rangle$ and $|F = 1, m_F = 0\rangle$, where $g_F = \frac{1}{2}$ and μ_B is the Bohr magneton. (Nearly all reported data is in units of Hz, for which $f_L = g_F \mu B/h$ is the relevant form.) The data for $t = 150$ μs shows the tell-tale sidelobes of Rabi spectroscopy (Eq. 4.4). In general, we find that the magnetic field can jump by several kHz over the course of hours and by ∼1 kHz over minutes. This large variations requires pulse times shorter than 200 μs. Unlike typical Rabi spectroscopy, we keep the maximum angle pulse area $\Omega_0 t \ll 1$ so as to not saturate the images: a full transfer will saturate the imaging system and leads to a systematic underestimate of the atom number. The data in Fig. 4.14 is fit to the following Rabi oscillation formula.

$$N_{F=2} = N_0 \frac{\Omega_0^2}{\Omega_0^2 + (f - f_0)^2} \sin^2\left(\pi t \sqrt{\Omega_0^2 + (f - f_0)^2}\right) \tag{4.4}$$

4.4.2 Magnetic Field Gradients

Measuring and controlling magnetic field gradients is one of the more annoying aspects of spinor condensates. The magnetic fields, to order of gradients, can be expanded as follows.

$$\vec{B} = \begin{pmatrix} B_{0,x} \\ B_{0,y} \\ B_{0,z} \end{pmatrix} + \begin{pmatrix} B_{xx} & B_{xy} & B_{xz} \\ B_{yx} & B_{yy} & B_{yz} \\ B_{zx} & B_{zy} & B_{zz} \end{pmatrix} \begin{pmatrix} x \\ y \\ z \end{pmatrix} \qquad B_{ij} = \hat{x}_i \cdot \frac{\partial \vec{B}}{\partial x_j}$$

Except for the fields generated by the ultracold atoms, which we will discuss in Sec. 5.4, Maxwell's equations require that the magnetic field has no curl or divergence within the source-free vacuum chamber. This requires that $B_{ij} = B_{ji}$ and $B_{xx} + B_{yy} + B_{zz} = 0$.

The extent of the condensate is much smaller along the $\hat{z}$ direction than along $\hat{x}$ or $\hat{y}$. For this reason, we safely ignore gradients along $\hat{z}$. As we will see, orienting the bias field in-plane ($B_{0,z} = 0$) lets us ignore terms of the form B_{iz}. For simplicity, assume we orient the field along $\hat{x}$. The atoms feel a spin-dependent force that depends on the magnitude of the magnetic field. Insofar that $B_{0,x} \gg B_{ij}x_j$, we can expand the field as

$$\begin{aligned} |\vec{B}| &= \sqrt{(B_{0,x} + B_{xx}x + B_{xy}y)^2 + (B_{xy}x + B_{xy}y)^2} \\ &\approx B_{0,x} + B_{xx}x + B_{xy}y + \frac{1}{2B_{0,x}}\left(B_{xy}^2x^2 + 2B_{xy}B_{yy}xy + B_{yy}^2y^2\right). \end{aligned}$$

For large $B_{0,x}$, curvatures are suppressed. In addition, the gradients do not depend on B_{yy}. At first glance it would appear that we need to cancel both B_{xx} and B_{xy}. This would be true if we insisted on a bias field oriented along $\hat{x}$. If we instead choose a special axis to orient the bias field, we can suppress one more gradient. In particular, the special axis is an eigenaxes of the 2×2 matrix $\left(B_{ij}\right)$.

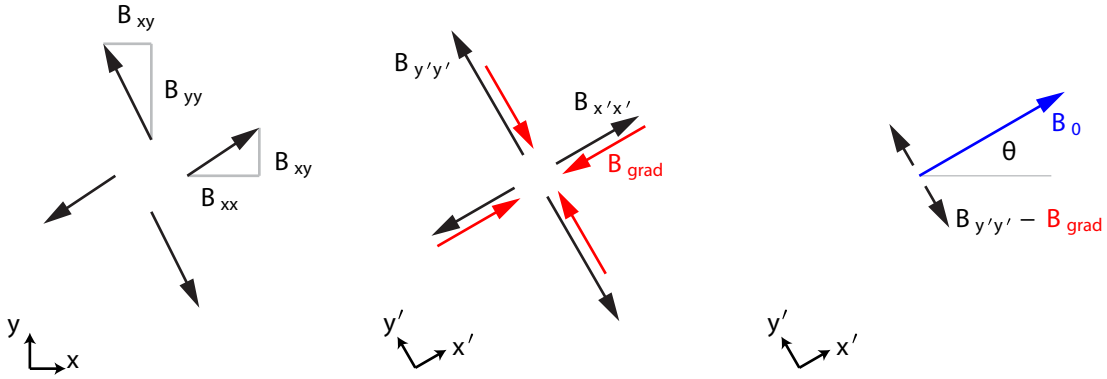

Figure 4.15: Gradient cancellation scheme. (Left) The cross-term B_{xy} can be mathematically eliminated in a (center) rotated frame. A spherical quadrapole field (red arrows) cancels the gradient along the $\hat{x}'$ axis. (Right) A bias-field $\vec{B}_0$ (blue arrow) oriented precisely along this axis creates a gradient-free environment.

In a rotated coordinate system (x', y') given by the eigenaxes of the matrix $\left(B_{ij}\right)$, the off-diagonal term $B_{x'y'} = 0$ (Fig. 4.15, left and center). To this field we add a spherical quadrupole field $B_{\text{grad}}\,(\vec{x} + \vec{y})$. With this field we can cancel one gradient, e.g. by choosing $B_{\text{grad}} = -B_{x'x'}$ (Fig. 4.15, center). We then carefully orient the bias field along $\hat{x}'$ (Fig. 4.15, right). In the language of linear algebra, we set one eigenvalue to zero and orient the bias field along the corresponding eigenvector. Experimentally, we monitor the gradients and iteratively cancel the gradient along the bias field (with B_{grad}) and transverse to the bias field (with the bias field orientation θ). This can be seen by expanding the field for small deviations from the gradient-free configuration.

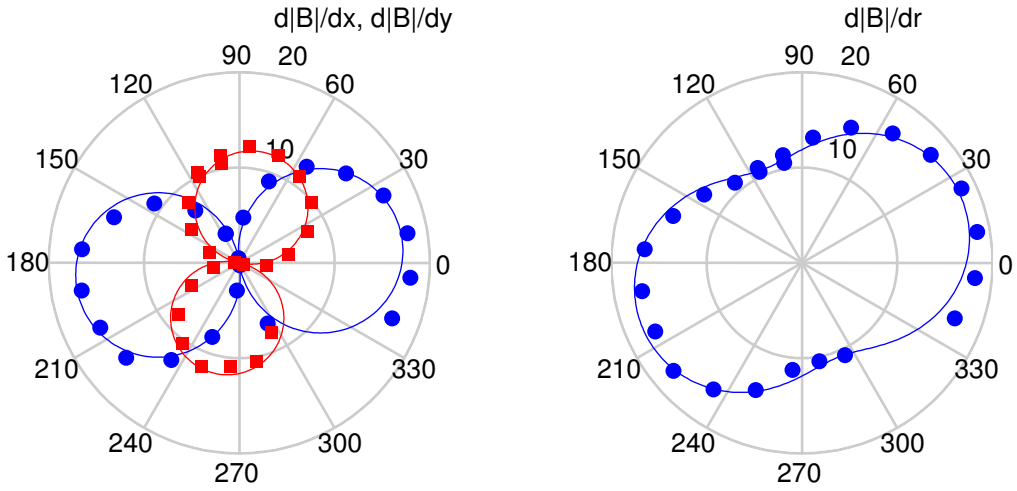

Figure 4.16: Measurement of the magnetic field gradients. (a) Magnetic field gradient along x (blue circles) and y (red squares) as a function of bias field angle θ. Lines are fits to the data for $B_{xx} = 17.1(2)$ Hz/μm, $B_{xy} = 2.5(2)$ Hz/μm, and $B_{yy} = 11.6(2)$ Hz/μm. (b) Same data, but showing the magnitude of the gradient versus bias field angle. The deviation from 180° symmetry is most likely due to small gradients created by the bias field coils used to reverse the field direction. Ramsey pulses are 0.5–1.0 ms on the $|F = 1, m_F = -1\rangle \rightarrow |F = 2, m_F = -2\rangle$ microwave transition. For reference, 1 Hz/μm = 14 mG/cm.

$$|\vec{B}| \approx B_0 - x\, B_{\text{grad}} + y\, d\theta B_{y'y'}$$

4.4.3 Optical Zeeman Effect

A weak magnetic field pertubs an atom by adding a term $H_B = -\vec{\mu} \cdot \vec{B} = -\frac{1}{\hbar} g_F \mu_B \vec{F} \cdot \vec{B}$ to the Hamiltonian. Light tuned to the right wavelength can create the same Hamiltonian, except the magnetic field $\vec{B}$ is replaced by a function of the intensity, detuning, and polarization of the light. Using light has a key advantage: the Hemlholtz equation that governs optics allows for much more varied structures than Laplace's equations allow for magneto-statics. In particular, we use this method to create effective magnetic fields with either Gaussian or sinusoidal profiles. We call a laser tuned to this wavelength the *optical Zeeman laser*.

In rubidium, the spin-orbit coupling of the electronic excited state can be leveraged to create coupling between the hyperfine spin and laser polarization. Fig. 4.17a shows the calculated ac Stark shift of the three $F = 1$ states in the presence of a circularly polarized laser. At the "magic-zero" or "tune-out" wavelength 790.03 nm, the Stark shift vanishes for $m_F = 0$ atoms [51]. A laser tuned to this wavelength cannot excite phonons in an $m_F = 0$ condensate (Fig. 4.17a(b)), but can excite spin waves. This will be our primary technique to study magnons in the next chapter.

We can detect the effective magnetic field from the optical Zeeman effects with a

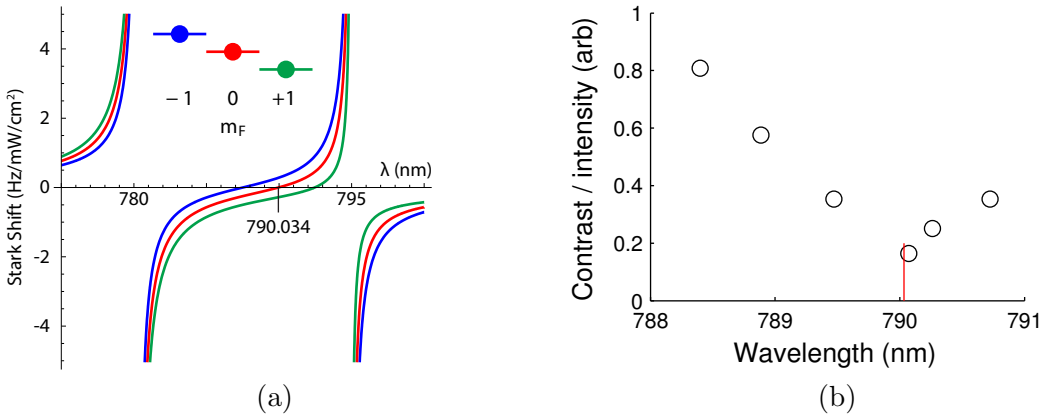

Figure 4.17: AC Stark shift and suppression of phonons at the magic-zero wavelength. (a) Calculated ac Stark shift of the $F = 1$ states for a circularly polarized laser. More advanced calculations indicate that the ac Stark shift of the $m_F = 0$ state vanishes at 790.034(7) nm [51]. (b) A standing wave excites phonons in an $m_F = 0$ condensate. At the magic-zero wavelength, the contrast of the phonons is minimized.

Ramsey interferometer similar to our measurement of magnetic field gradients [52]. The atoms are illuminated by the optical Zeeman laser for 2 ms between two RF $\pi/2$ pulses with the magnetic field oriented parallel to the laser propagation and to gravity. The laser adds diagonal terms to the Hamiltonian proportional to F_z. In this case, we have a very sensitive map of the optically induced field. The peak shows $\sim 4\pi$ phase shift at the highest intensity, corresponding to a Rabi frequency of $h \times 1$ kHz.

The optical Zeeman laser can also rotate the longitudinal magnetization by introducing an oscillating off-diagonal matrix terms, e.g. proportional to $F_y \cos \omega t$. These terms can create spin structures where the polar angle of magnetization varies inhomogeneously. In this case, we orient the propagation direction of the laser transverse to the magnetic bias field (Fig. 4.19a) to create an energy proportional to F_y. The resonance condition requires oscillating the intensity of the laser at the Larmor frequency $\frac{1}{2}\mu_B B_0$, where B_0 is the local real magnetic field. An example of is shown in Fig. 4.19b, where the optical Zeeman laser is focused to a waist ($1/e^2$ radius) of 12 μm inside a much larger condensate. This process can also be described as a resonant two-photon Raman transfer.

More interesting examples are shown in Fig. 4.20. For instance, frequency chirping the amplitude modulation, rather than a resonant amplitude modulation, can create a Landau-Zener transfer with a substantial transverse spin structure (Fig. 4.20c).

4.5 Quadratic Zeeman Shift and spinor phase transitions

As described above in Sec. 4.1.3, the ground state phase depends on a competition between the spin-dependent contact interactions $\frac{1}{2}c_2 n\langle \vec{F}^2 \rangle$ that favors a ferromagnetic state and the quadratic Zeeman Shift $q\langle F_z \rangle$ that favors a polar state. Tuning q can cause the polar ground state $(0, 1, 0)$ to suddenly find itself far out of equilibrium in the ferromagnetic

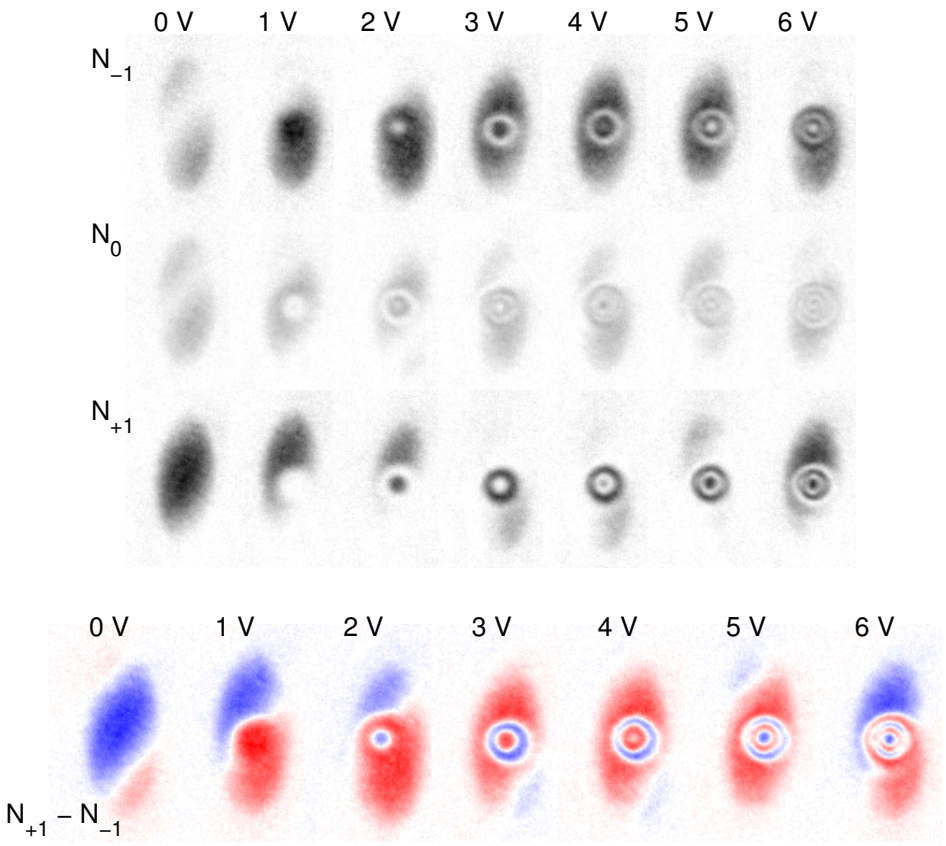

Figure 4.18: Optical Zeeman effect measured with a Ramsey interferometer. An effective magnetic field is applied to the atoms for 2 ms between RF $\pi/2$ pulses. Images show the spin density in the $m_F = -1, 0, +1$ states as well as the magnetization $M_z = N_{m_F=+1} - N_{m_F=-1}$. The voltage is proportional to the intensity of the optical Zeeman laser.

portion of the phase diagram [42, 14]. We verify our preparation, control, and imaging by reproducing this quench in Fig. 4.21.

The quench is performed by suddenly turning on a off-resonant microwave drive. The drive is detuned +40 kHz from the $|F = 1, m_F = 0\rangle \rightarrow |F = 2, m_F = 0\rangle$ transition and decreases the energy of the dressed $|F = 1, m_F = 0\rangle$ state. The $m_F = \pm 1$ states are initially seeded with a brief RF pulse to speed up the process. A magnetic field gradient separates the domains and lets them grow is size. Without a gradient, the domain size increases only very slowly [14].

The evolution of a quench depends on the sample preparation. The spin-dependent Hamiltonian allows for dynamics where two atoms in the $m_F = 0$ scatter into the $m_F = +1$ and $m_F = -1$ states, conserving $\langle F_z \rangle$ and spherical symmetry. The conservation prohibits the polar ground state $(0, 1, 0)$ from evolving into a longitudinal ferromagnetic ground state, such as $(1, 0, 0)$. Instead, for a fixed magnetization, the system evolves towards two large domains of $(1, 0, 0)$ and $(0, 0, 1)$. The evolution of the $m_F = 0$ population can be seen in Fig. 4.22. Dipolar interactions can allow for collisions that change $\langle F_z \rangle$, but we do not

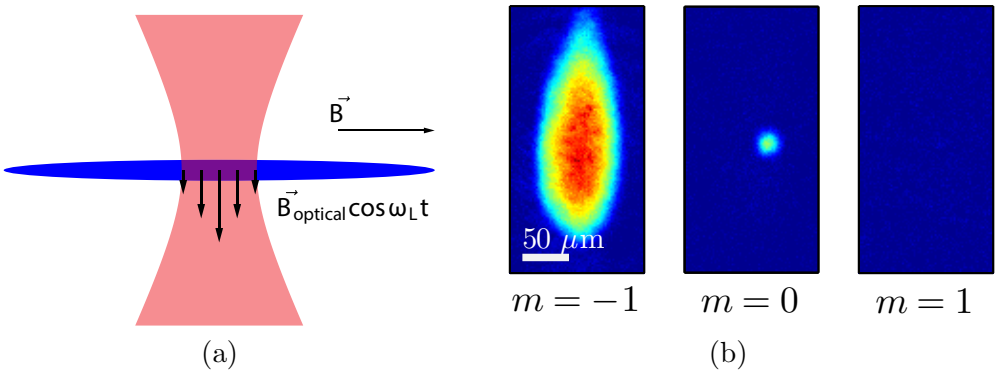

Figure 4.19: Optically writing of spin excitations. (a) A focused laser (red hyperbola) introduces an effective transverse magnetic field proportional to the local intensity. As the laser amplitude is modulated as the Larmor frequency, the magnetization of the atoms (blue trap) is rotated longitudinally. (b) A rotation of the longitudinal magnetization can be measured as a slight increase in the local $m_F = 0$ population. This can be described as $\sim 10^3$ magnons. The time evolution of this pattern is investigated in Sec. 5.2.

observe this process.

4.6 Future

This chapter set out the experimental requirements of working with spinors and the capabilities offered by the apparatus. The next step is applying this knowledge to explore new physics. Ch. 5 focuses on elucidating the basic properties of magnons, spin wave excitations, of the ferromagnetic condensate.

There are several other promising directions for this setup. For instance, ASSISI is unique in observing real-time dynamics of polar phases, which could be used to explore quenches, instabilities, and topological structures in the polar phase. Another compelling direction is studying domain walls, which are experimentally easy to create and common to many broken symmetry systems [40].

4.6.1 Domain walls.

An immiscible mixture of two components has a ground of two large domains. If the mixing energy is large, the two components will be separated by a sharp domain wall of width $\sim \hbar/\sqrt{m \times \text{mixing energy}}$. Fluctuations in the location of the domain wall may have a much lower energy scale, since they depend not on the mixing energy but the kinetic energy of a curved wavefunction. Excitations of a domain wall are known as ripplons and are predicted to have fractional dispersion relations, e.g. $\omega \propto k^{3/2}$ [53, 54, 55].

The $m_F = -1$ and $m_F = +1$ states form an immiscible mixture in the ferromagnetic phase (Fig. 4.23). Mixing of these two states decreases $\langle \vec{F}^2 \rangle$, which is energetically costly. We create an equal mixture by performing an RF rotation ($\omega_L \tau = \pi/2$) of a pure $m_F = 0$ condensate. The system starts in the highly energetic polar states, which quickly

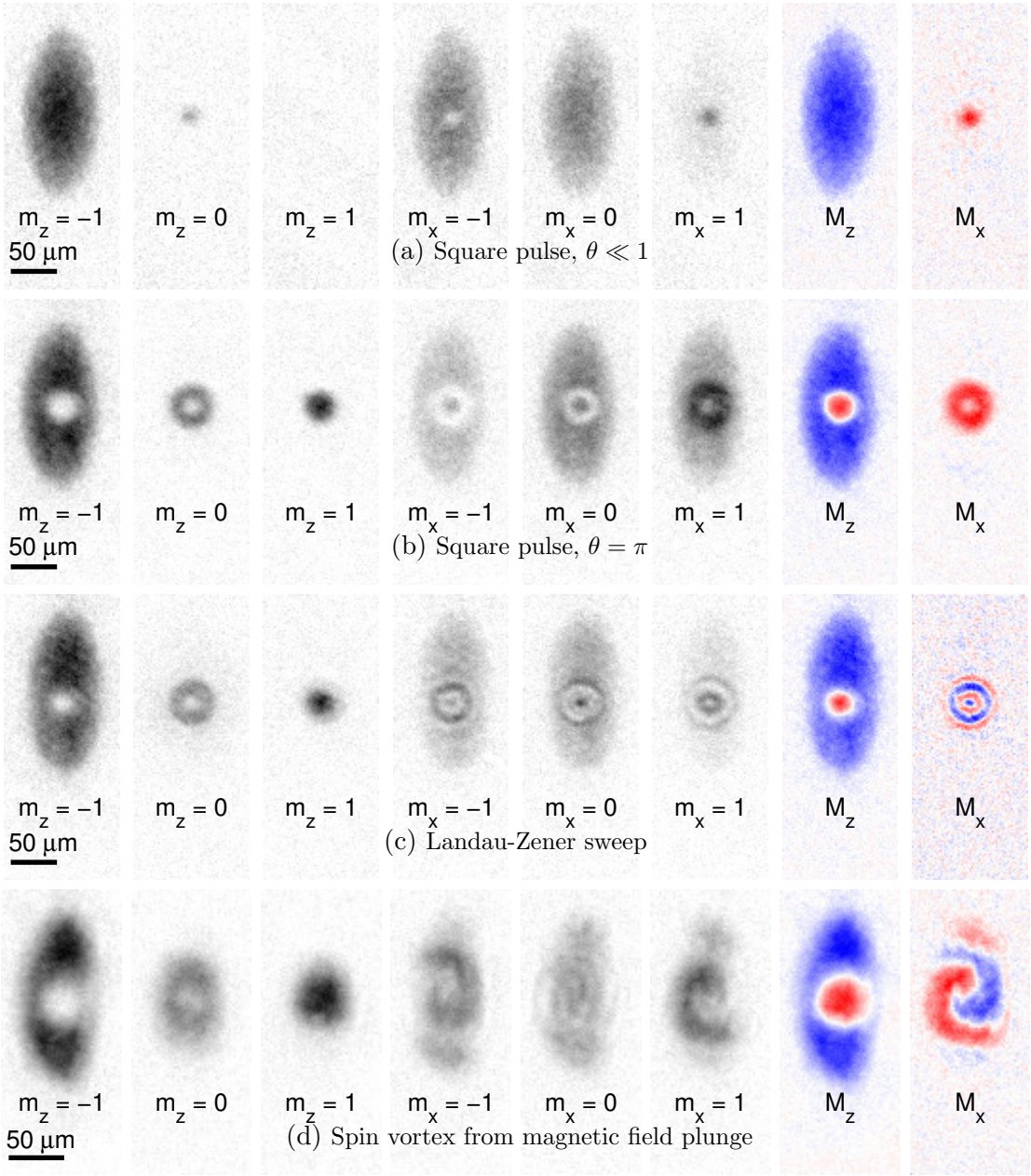

Figure 4.20: Creating a compact spin structure. (a) The optical Zeeman laser is briefly amplitude modulated to rotate the spin in the $x-z$ plane. This produces a small m_z=0 population and transverse magnetization M_x. (b) A longer pulse produces a π rotation at the center of the laser with a smooth transverse magnetization, still confined to the $x-z$ plane. (c) An alternative strategy is to frequency chirp the amplitude modulation to create a Landau-Zener sweep. The transverse magnetization now varies rapidly and circles about the z axis. The longitudinal magnetization of (b), (c), and (d) the spin vortex (from Fig. 4.8) are nearly identical, but the transverse magnetization is qualitatively different.

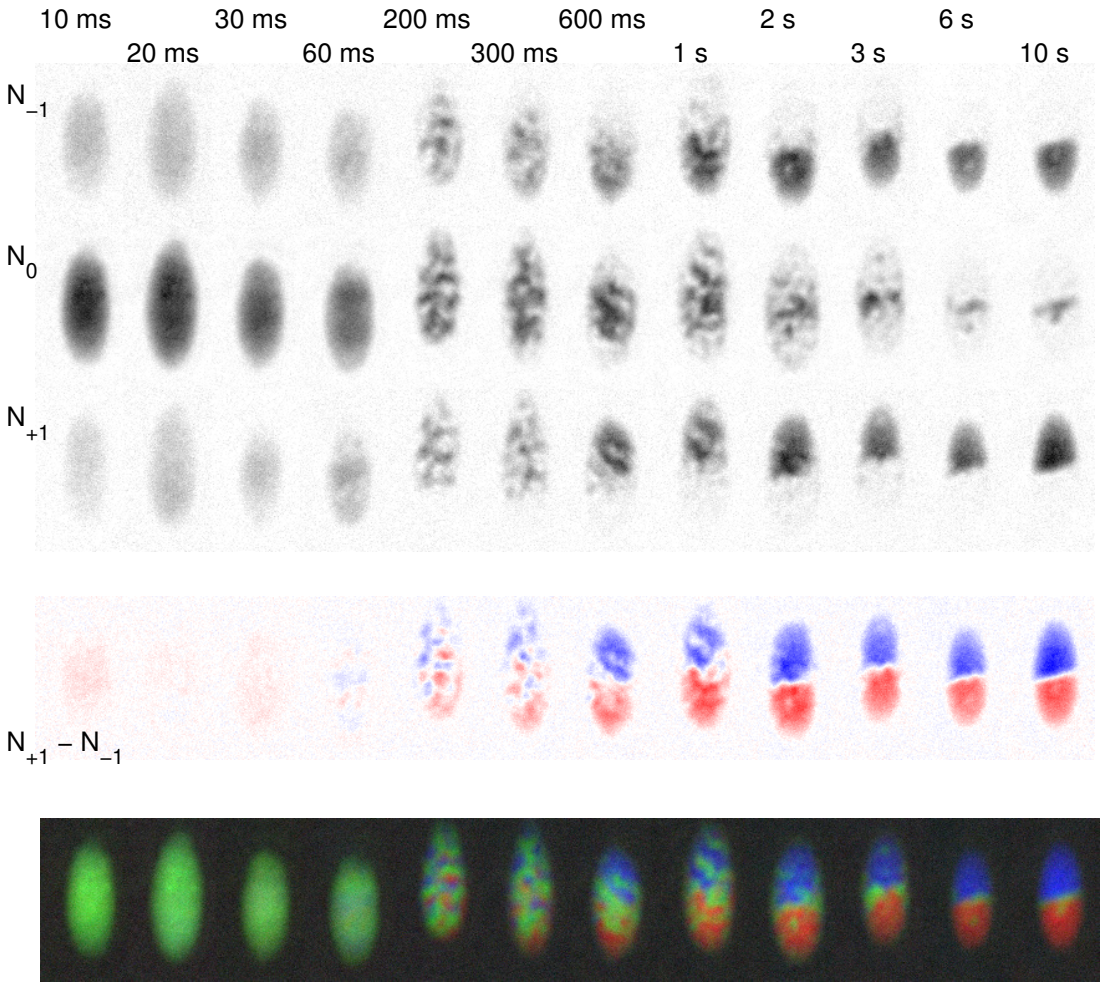

Figure 4.21: Quench of a polar condensate. The $m_F = 0$ condensate is seeded with an initial population of $m_F = \pm 1$ atoms. (Top)

phase separates with the help of a magnetic field gradient.

The domain wall remains jagged even after two seconds. This could because of thermal fluctuations or undamped oscillation from the separation process. We later learned that several vortices are often created during condensation; the fluctuations in the domain wall could due to motion of the vortices. A better experimental sequence would involve creating the mixture in the thermal gas and condensing in the presence of a gradient without vortices. From a large number of independent realization we could extract the equal time correlation function of the domain wall. Multiple imaging would allow for the complete space-time correlation function. The unusual dispersion relation may lead to an unusual correlation function.

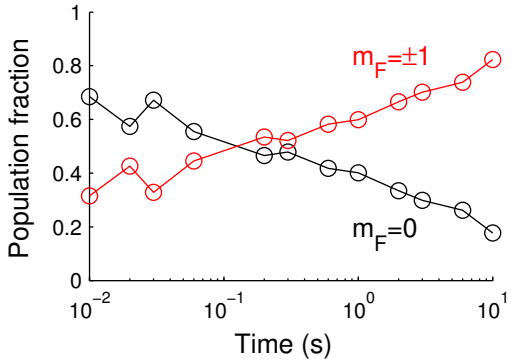

Figure 4.22: Spin populations during a quench. The initial imbalance between $m_F = 0$ and $m_F = \pm 1$ is set by a brief RF pulse that rotates a uniform $(0, 1, 0)$ ground state. During the quench to the ferromagnetic state, the $m_F = 0$ slowly vanishes.

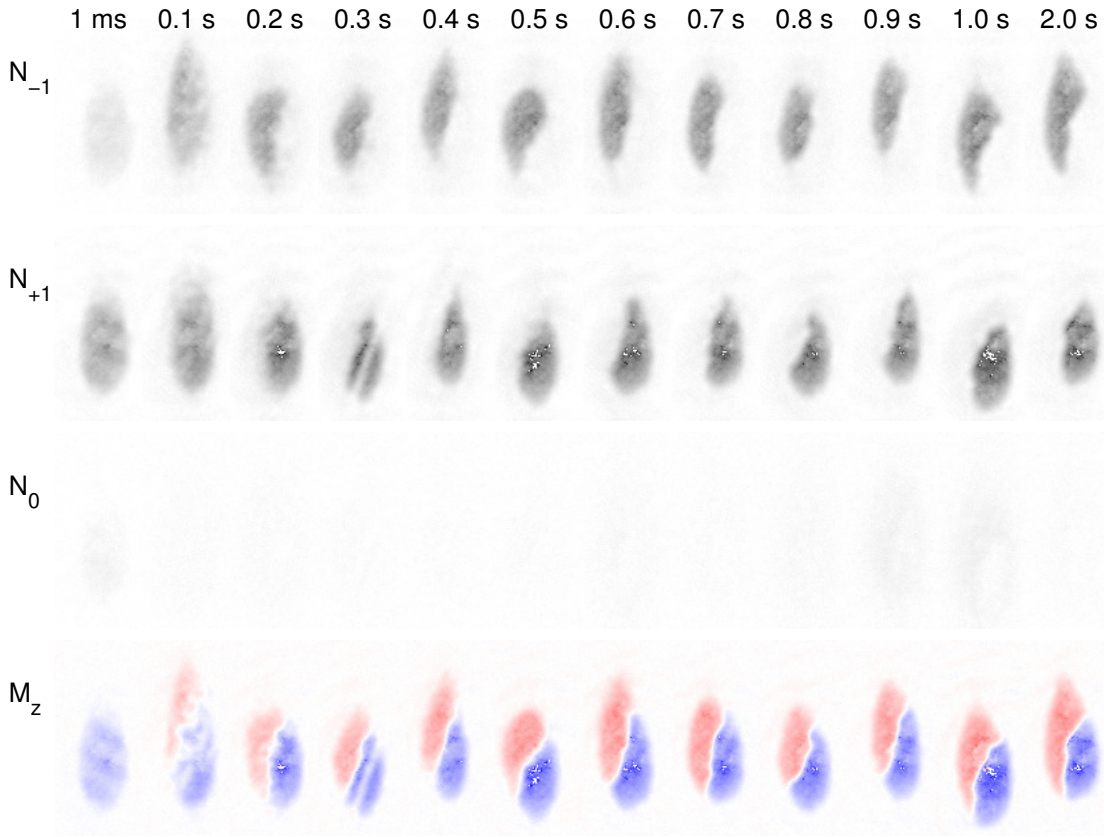

Figure 4.23: Domain wall formation between the $m_F = +1$ and $m_F = -1$ states in the ferromagnetic phase. A nearly pure $\frac{1}{\sqrt{2}}(1, 0, 1)$ state separates into two domains after a few hundred milliseconds in a magnetic field gradient. Even after two seconds, the domain wall is clearly jagged. The excitation could by thermally activated or arise from undamped oscillations created during the separation procedure.

Chapter 5

Magnons

5.1 Low-energy excitations: phonons and magnons

As discussed in the beginning of Ch. 4, the symmetry of a condensed matter system is intimately tied to its low energy excitations and therefore its low temperature thermodynamic properties. For instance, a scalar Bose gas breaks a global phase symmetry when it becomes a condensate. A ferromagnetic BEC breaks a total of three symmetries[1], but has only two Nambu-Goldstone bosons: phonons, with a linear dispersion relation, and magnons, with a quadratic dispersion relation [58, 59]. The difference between the number of broken symmetries and the number Nambu-Goldstone bosons has been recently understood [6].

In this chapter we apply tools from precision experiments in atomic physics to investigate the magnetic moment, dispersion relation, and gap of magnons in a ferromagnetic condensate. We perform these experiments by creating and interfering coherent magnon waves. There are two key results in this chapter. First, we directly observe a gap created by magnetic dipole-dipole interactions that is consistent with mean-field theory. Second, we measure a magnon recoil frequency that is close to, but systematically smaller than, the expected result for mean-field theory with contact interactions. We claim this as evidence of a heavy magnon, with an effective mass 3.3% heavier than the bare rubidium mass.

5.1.1 Linearized Schrödinger equation

We will derive phonons and magnons by adding fluctuations to the order parameter $\psi = \sqrt{n}\,(1,0,0)$ and linearize the resulting Schrödinger equation. Physically, fluctuations

[1] At high temperatures, an $F = 1$ Bose gas is symmetric under rotations and the addition of a quantum mechanical phase, summarized by the symmetry group $G = SO(3) \times U(1)$. At low temperatures, a ferromagnetic condensate minimizes its energy by choosing a global phase and spin direction. What is less obvious is that the low temperature state is still invariant to a combined rotation about the axis of magnetization by an angle α and the addition of a phase $-\alpha$: $e^{i\alpha}e^{-iF_z\alpha/\hbar}(1,0,0) = (1,0,0)$. The symmetry group of the ferromagnetic state is then $H = U(1)$. The broken symmetries are characterized by the order parameter manifold $M = G/H = SO(3)$ [56, 57].

can be parameterized in terms of changes in the density and spin orientation.

$$\psi = \sqrt{n}e^{-i\mu t}(1+\chi)\, R(\theta,\phi)\begin{pmatrix}1\\0\\0\end{pmatrix} \xrightarrow{\theta\ll 1} \sqrt{n}e^{-i\mu t}(1+\chi)\begin{pmatrix}1-\frac{1}{4}\theta^2\\ \frac{1}{\sqrt{2}}\theta e^{-i\phi}\\ \frac{1}{4}\theta^2 e^{-2i\phi}\end{pmatrix} \tag{5.1}$$

The small complex number χ characterizes changes in the scalar density and phase, while θ and ϕ are Euler angles that characterize changes in the spin orientation. These fluctuations are along the broken symmetry directions of the ferromagnetic ground state and are expected to produce gapless excitations. Fluctuations of the $m_F = -1$ component, neglected here, create gapped excitations[58].

The contact interactions do not depend on θ or ϕ, so the interaction term in the Schrödinger equation evaluates to $\mu|1+\chi|^2\psi$ with $\mu = (c_0 + c_2)n$ (see Sec. 4.1.2 and Eqs. 4.2, 4.3). It is easiest to characterize fluctuations of spin by the complex number $\zeta = \frac{1}{\sqrt{2}}\theta e^{-i\phi}$, which is the wavefunction for $m_F = 0$ atoms. We can now linearize the ansatz and Schödinger equation.

$$\psi \approx \sqrt{n}e^{-i\mu t}\begin{pmatrix}1+\chi\\ \zeta\\ 0\end{pmatrix} \tag{5.2}$$

$$i\hbar\dot{\chi} = -\frac{\hbar^2}{2m}\nabla^2\chi + 2\mu(\chi+\chi^*) \tag{5.3}$$

$$i\hbar\dot{\zeta} = -\frac{\hbar^2}{2m}\nabla^2\zeta \tag{5.4}$$

These two equations represent the two Nambu-Goldstone bosons of our system: phonons (χ) and magnons (ζ). The eigenspectrum of Eq. 5.3 is the well-known Bogoliubov phonon with $E_\chi = \sqrt{(\hbar^2k^2/2m)(\hbar^2k^2/2m + 2\mu)}$. Magnons, as described by Eq. 5.4, have free-particle solutions $E_\zeta = \hbar^2k^2/2m$ with no gap and an effective mass identical to the bare mass of rubidium. Our experiments nearly reproduce this simple analysis, but we will find that dipolar interactions introduce a slight gap (energy offset). We also observe a heavier effective mass.

In this section, we will exclusively study magnons by setting $\chi = 0$. Eq. 5.4 is solved by $\zeta = \zeta_0\, e^{i\left(\vec{k}\cdot\vec{x}-\omega(k)t\right)}$. To order $O(\theta)$, this solution represents a magnetization with a fixed polar angle θ and a periodic azimuthal angle $\phi = \vec{k}\cdot\vec{x} - \omega(k)t$.

$$\psi_{\text{magnon}} = \sqrt{n}e^{-i\mu t}\begin{pmatrix}1\\ \frac{1}{\sqrt{2}}\theta e^{i(\vec{k}\cdot\vec{x}-\omega(k)t)}\\ 0\end{pmatrix} = \sqrt{n}e^{-i\mu t}\, R(\theta,\vec{k}\cdot\vec{x}-\omega(k)t)\begin{pmatrix}1\\0\\0\end{pmatrix} \tag{5.5}$$

Our data is inconsistent with the mean-field dispersion relation $\omega(k) = \hbar k^2/2m$, but instead matches $\omega(k) = \Delta(n) + \hbar k^2/2m^*$. Regardless, we will assume the form of Eq. 5.5 for small values of θ.

The next order of Eq. 5.4 includes phonon-magnon interactions. Numerical simulations show that the eigenfrequency shifts depending on the amplitude of $|\zeta|^2$, i.e. at non-negligible $m_F = 0$ populations.

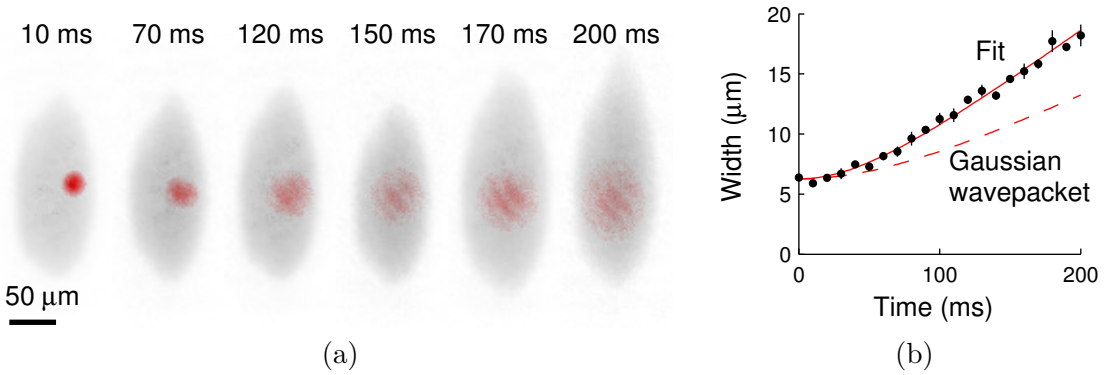

Figure 5.1: Expansion of a magnon wavepacket. A Gaussian wavepacket of spin is created with a brief pulse from the optical Zeeman laser. (a) Expansion of the $m_F = 0$ atoms (red) in the presence of a weak magnetic field gradient over 200 ms. The condensate profile is shown in light gray. It is not clear whether the fringes are real or imaging aberration. (b) An average of the width over time for three runs (black circles). The fit shows the expected hyperbolic profile (red line). However, it expands more rapidly than is expected for a Heisenberg-limited wavepacket (red dashed line). This is most likely because the laser intensity is not Gaussian, as evidenced by the structure seen after 120 ms.

5.2 Magnons act like free-particles in a flat potential

For a nonuniform trapping potential, the effective potential for spin excitations remain flat because of a precise cancellation of the trapping potential and mean-field repulsion of the condensate. For convenience we'll present an alternative derivation of Eq. 5.4, with an $m_F = 0$ wavefunction ψ_0 (equivalent to ζ in our ansatz). In the limit of a small magnon population (neglecting terms of order $|\psi_0|^2$ and $\psi_{-1}\psi_{+1}$), the Schrödinger equation is

$$i\hbar\dot{\psi}_0 = -\frac{\hbar^2}{2m}\nabla^2\psi_0 + V_0\psi_0 + (c_0 + c_2)\psi_{-1}^*\psi_{-1}\psi_0 = -\frac{\hbar^2}{2m}\nabla^2\psi_0 + V_{\text{eff}}\psi_0.$$

In the Thomas-Fermi limit, the condensate density matches the trapping potential $n_{-1} = (\mu - V_{-1})/(c_0 + c_2)$.

$$V_{\text{eff}} = V_0 + (c_0 + c_2)\frac{\mu - V_{-1}}{c_0 + c_2} = V_0 - V_{-1} + \frac{\mu}{c_0 + c_2} \tag{5.6}$$

Hence, magnons propagate as if the potential were flat, as long as they remain in a region of the condensate where the Thomas-Fermi approximation applies. Within the condensate, the density shift precisely cancels the trap confinement. This satisfies the intuition that magnetic excitations, like most quasiparticles, live 'on top of' the condensate and are impervious to small defects in the trapping potential. For instance, an interferometer based on magnons should be impervious to small corrugations in the trapping potential.

Our first and simplest experiment with magnons is to monitor the expansion of a small wavepacket (Fig. 5.1). The optical Zeeman laser is tightly focused to a spot size of 12 μm (e^{-2} radius). A brief pulse from that laser locally rotates the magnetization, which

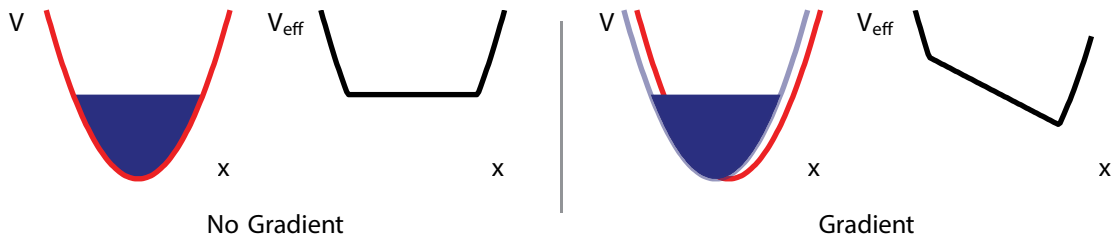

Figure 5.2: Effective potential of a magnon in a gradient. (Left) Without a magnetic field gradient, the magnons experience a potential from the optical trap and the mean-field shift of the $m_F = -1$ condensate. These contribute to an effectively flat trap where the local chemical potential is nonzero. (Right) In the presence of a magnetic field gradient, the density of the $m_F = -1$ condensate is shifted (light blue) while the potential for $m_F = 0$ is unchanged. The effective potential for $m_F = 0$ is the sum, which contains the gradient.

we image as a small population of $m_F = 0$ atoms (Figs. 5.1a and 4.19). We expect that a wavepacket with an initial $e^{-1/2}$ radius σ_0 will expand like a free particle in a flat potential.

$$\sigma(t) = \sqrt{\sigma_0^2 + \left(\frac{\hbar t}{2\sigma_0 m}\right)^2} \tag{5.7}$$

In Fig. 5.1b, we observe an expansion that qualitatively matches this theory. However, the rate of expansion is 50% faster than expected for a Gaussian wavepacket. In addition, the wavepacket shapes shows odd and distorted structures for expansion times beyond 100 ms. Most likely both of these effects are due to aberrations in the optical Zeeman laser profile, as any non-Gaussian profile with a uniform initial phase will expand more quickly than predicted by Eq. 5.7. It is also possible that non-zero flow of the superfluid distorts the images.

The expansion of a wavepacket also gives an estimate for the effective mass m^* of a magnon, though as we have seen this estimate is biased by initial errors in the preparation. In the next several sections we will greatly improve our estimates of the effective mass.

5.2.1 Magnetic Moment

Above we described a magnon as an $m_F = 0$ atom that lives in a sea of $m_F = -1$ atoms. In most experiments, it is sufficient to ignore the background condensate and pretend that we have $m_F = 0$ atoms in a flat potential. Yet a magnetic field gradient accelerates magnons as if their magnetic moment were $\mu = -\mu_{BEC} = \frac{1}{2}\mu_B$. This is because a displacement of the condensate creates a force on magnons due to the chemical potential gradient.

Fig. 5.2 illustrates the effect. A magnetic field gradient shifts the equilibrium position of the $m_F = -1$ condensate. According to Eq. 5.6, $V_{-1} = V_0 - \mu_{-1}B'x$, so the new effective potential $V_{\text{eff}} = -\mu_{-1}B'x$ has a gradient. Hence, magnons have an effective magnetic moment $\mu^* = -\mu_{-1} = -\frac{1}{2}\mu_B$.

The precise cancellation of the potential and mean-field energy is unique to spinor condensates with contact interactions because the m_F states are connected through rotational symmetry. A condensate that is spin-polarized along $m_F = -1$ is a superposition of

m_F states along another basis. Thus it is not a coincidence that the $m_F = -1 \leftrightarrow m_F = 0$ scattering length is exactly the same as the $m_F = -1 \leftrightarrow m_F = -1$ scattering length. In pseudo-spin systems, such as $F = 1$ and $F = 2$ mixtures, this cancellation is not perfect and adds a slightly curvature to the potential. This also implies that the Larmor frequency has no density-dependent shift due to contact interactions, while there is a density dependent shift on the clock transition between $F = 1$ and $F = 2$ states.

We can measure the magnetic moment by accelerating a magnon wavepacket in a magnetic field gradient. First, we condense a pure $m_F = -1$ condensate in the presence of the small magnetic field gradient. Then, a magnon wavepacket is suddenly created with the optical Zeeman laser. The wavepacket accelerates in the direction of the gradient, like a free particle under constant force. The gradient can be independently measured by a Ramsey pulse sequence to a third state, $|F = 2, m_F = -1\rangle$, as described in Sec. 4.4.2. The sign of the gradient is determined from the change in equilibrium position of the condensate.

$$a = \frac{\mu^* B'}{m^*} \qquad \lambda_{\text{gradient}} = \frac{h}{\mu B' \tau} \qquad a\lambda_{\text{gradient}}\tau = \frac{\mu^*}{\mu}\frac{h}{m^*}$$
$$\mu^* = -1.04(2)_{\text{stat}}(8)_{\text{sys}}\ \mu_{-1} \tag{5.8}$$

This analysis assumes that the Ramsey pulse sequence depends on the true magnetic moment μ, whereas the kinematic acceleration depends on μ^*. This might not be true, but, in any case, at our level of accuracy, the kinematic experiment lacks the fine resolution needed to test mean-field physics. At our measurement resolution, it clearly agrees with our expectation that a magnon in a ferromagnetic condensate has an effective magnetic moment consistent with $-\mu_{-1}$ and inconsistent with the magnetic moment of a free $m_F = 0$ atom. In Eq. 5.8, we set $m^* = 1.033\, m$, as measured in Sec. 5.3.

Uncertainty in the magnification of the imaging system adds a substantial systematic error. If our magnification is incorrect by a factor γ, then both the acceleration and $\lambda_{\text{gradient}}$ have an error proportional to γ. The overall uncertainty in μ^* is then proportional to γ^2. When we later measured the magnon dispersion relation, we found an error of $\approx 4\%$ in the imaging magnification of a standing wave of magnons compared to an independently calibrated CCD camera. Thus, we estimate the systematic error to be 8%, far outweighing the systematic uncertainty.

The magnetic moment also serves as a measure of h/m^*, with a measured value consistent with the mean-field theory prediction $m = m^*$. In the next section, we will introduce a new method to measure m^* with an order of magnitude reduction in statistical and systematic uncertainties.

5.3 Dispersion Relation

5.3.1 Standing wave and the quasiparticle dispersion relation

Quite generally, a standing wave consists of stationary nodes and antinodes whose amplitude oscillates sinusoidally in time. The functional form will typically look something like this:

$$A(x, t) = e^{-\Gamma t} \cos kx \cos \omega t.$$

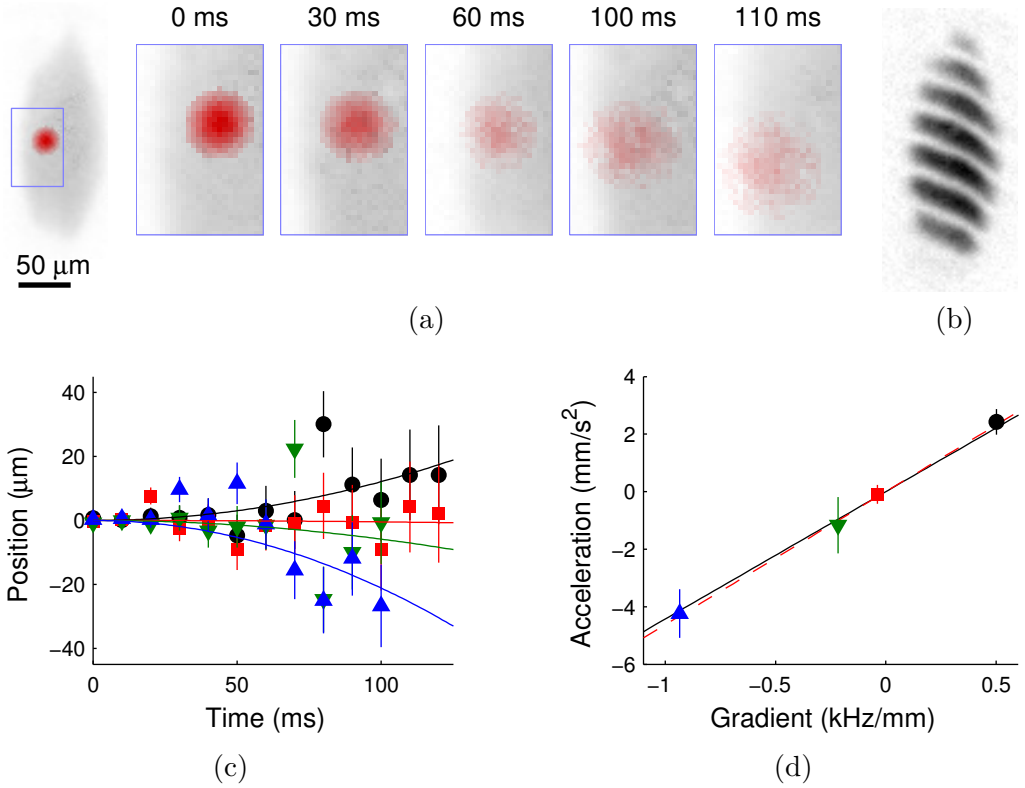

Figure 5.3: Magnetic moment of a magnon. A Gaussian wavepacket is consistently created in one location. (a) The wavepacket is accelerated in the direction of the magnetic field gradient. As explored in the previous section, the wavepacket expands while it accelerates. The region-of-interest (blue box) is 50 by 75 μm. (b) The magnetic field gradient is determined by a Ramsey interferometer sequence between $|F = 1, m_F = -1\rangle$ and $|F = 2, m_F = -1\rangle$. The image shows fringes in the $F = 2$ population. (c) The position versus time shows the expected quadratic dependence. However, we observe many outliers. The sloshing of the condensate creates an initial uncertainty in velocity, which turns into an uncertainty in position which increases in time. The data is fit with a least-squares algorithm that self-consistently determines the standard error as a function of time (vertical lines, 1 σ errors). (d) Fits of the acceleration from the kinematic data versus gradient. The data is closer to the fit (black line) and theory (red line) that it should be, given the large uncertainty in position measurements.

In this context, we can identify the dispersion relation as a function that connects the wavenumber to the frequency, $\omega(k)$. In a many-body system, a standing wave of elementary excitations will have an oscillating amplitude A—magnetization for magnons, density for sound—with a value of k and ω that correspond to the usual dispersion relation. In atomic physics, the dispersion relation frequency is known as a recoil frequency. The experimental strategy is to create a standing wave of one wavelength and measure the resulting oscillation frequency. This allows for an AC measurement in both space and time, which will generally give good signal-to-noise. By changing the wavelength over many experiments, the dispersion relation function can be mapped out. This section describes our efforts to measure the magnon dispersion relation with this technique (Fig. 5.4).

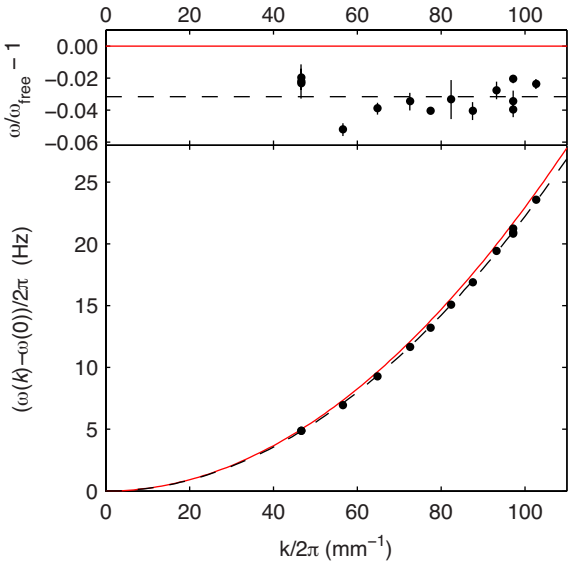

Figure 5.4: Our final data for the dispersion relation of a magnon. As expected, the dispersion relation is very close to a quadratic result $\omega \propto k^2$ (black dashed line). The surprising result is that the frequencies are systematically shifted down, corresponding to a magnon mass of 3.3% heavier than the bare rubidium mass (solid red line).

5.3.2 Description of experiment: spin wave and contrast interferometry

We create a standing wave of magnons with a spin-dependent optical potential, as described in Sec. 4.4.3. The mathematics is most clear in position coordinates, but the process is qualitatively easier to understand in momentum space. The spin-dependent potential is created by two laser beams that intersect at an angle ϑ. Both laser beams are intensity modulated at the Larmor frequency (typically 85 kHz, depending on the position of the elevator) for a few cycles, typically $30 - 60$ μs. Intensity modulation allows for resonant Raman transitions that simultaneously excite the spin and apply momentum kicks (Fig. 5.5).

What is less obvious in the momentum space picture is that certain processes are forbidden. For example, diffraction to the same spin state ($|m_F = -1, q = \pm k\rangle$) only enters

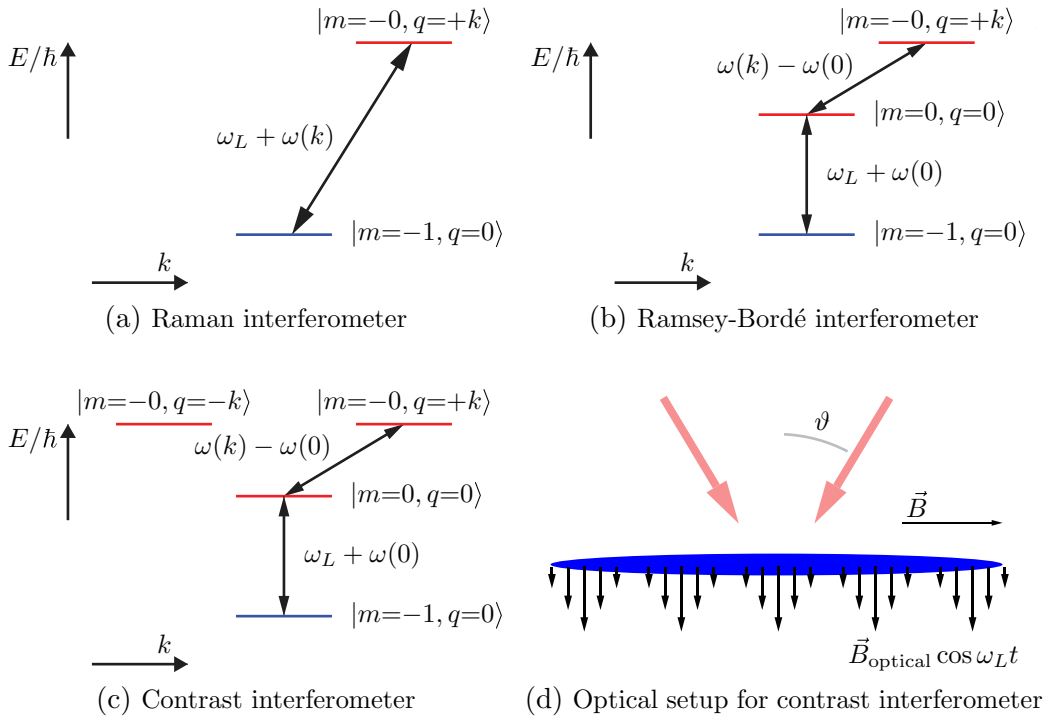

(a) Raman interferometer (b) Ramsey-Bordé interferometer

(c) Contrast interferometer (d) Optical setup for contrast interferometer

Figure 5.5: Raman, Ramsey-Bordé, and contrast interferometer schemes. A measurement of the dispersion relation by interfering matter waves at distinct momenta is typically termed a recoil frequency experiment. (a) The dispersion relation could be probed with a single magnon wavevector. Unfortunately, this scheme is sensitive to bias field fluctuations in the lab. (b) We can eliminate sensitivity to the magnetic field fluctuations by comparing the frequency of magnons created at two wavevectors, in particular at $\vec{q} = 0$ and $\vec{q} = \vec{k}$. This is similar to the Ramsey-Bordé interferometer. (c) With the contrast interferometer we also excite atoms to $\vec{q} = -\vec{k}$, which removes sensitivity to dipole oscillations of the condensate and acceleration noise. (d) A contrast interferometer is generated by interfering two paths of the optical Zeeman laser at a half-angle ϑ. The interference creates a periodically modulated effective magnetic field. A brief amplitude modulation at the Larmor frequency periodically rotates the magnetization, creating magnons at $q = 0$, $q = +k$, and $q = -k$, where $k = 2k_L \sin(\vartheta/2)$ and $k_L = 2\pi/(790.03\text{ nm})$ is the optical Zeeman laser wavenumber.

at second order. This is directly related to the choice of wavelength, where the scalar Stark shift vanishes. In position space, the laser induces a periodic Rabi frequency of the form $\Omega = \frac{\Omega_0}{2}(1 + \cos \vec{k} \cdot \vec{x})$. We apply the intensity modulated pulse for a time τ, which rotates the wavefunction about its axis by an angle $\theta(x) = \theta_{\text{avg}}(1 + \cos \vec{k} \cdot \vec{x})$, where $\theta_{\text{avg}} = \Omega_0 \tau/2$. The condensate wavefunction is initially fully polarized along $m_F = -1$.

$$\psi_{\text{after pulse}} = R_y(\theta)\sqrt{n}\begin{pmatrix} 0 \\ 0 \\ 1 \end{pmatrix} = \sqrt{n}\begin{pmatrix} \frac{1}{2}(1 - \cos\theta) \\ -\frac{1}{\sqrt{2}}\sin\theta \\ \frac{1}{2}(1 + \cos\theta) \end{pmatrix} \tag{5.9}$$

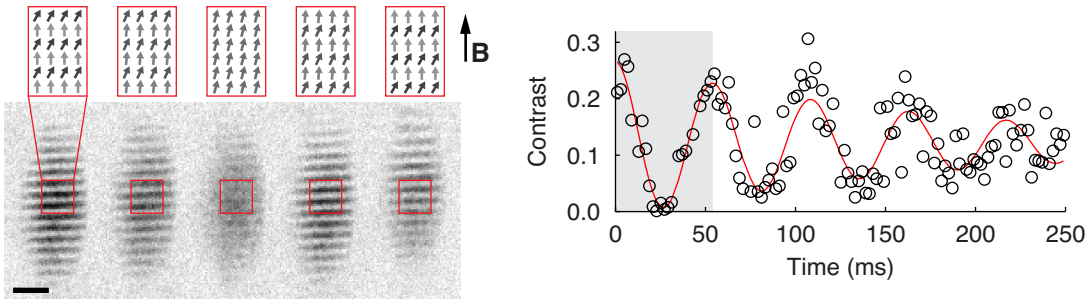

Figure 5.6: Sample images from the contrast interferometer. (Left) The system is initialized with a magnetization that is periodically tilted in the $x-z$ plane (top), where the corresponding density of $m_F = 0$ atoms is a series of straight fringes. The contrast of the fringes disappear and appear every half cycle. (Right) The contrast of the Fourier transform oscillates at twice the eigenfrequency. The system damps towards a finite contrast, possibly because of inhomogeneous broadening.

Up to $O(\theta_{\text{avg}}^2)$, we can expand the wavefunction as

$$\sqrt{n}\begin{pmatrix} 0 \\ -\frac{1}{\sqrt{2}}\theta_{\text{avg}}(1+\cos\vec{k}\cdot\vec{x}) \\ 1 \end{pmatrix}$$

Comparison to Eq. 5.5 shows that we have created a superposition of magnons at $q = 0, \pm k$, as advertised. In our experiment, we measure the local polar angle of the magnetization through the population of the $m_F = 0$ component. This method is reminiscent of dark-field imaging in optics [27] because we achieve a very low background (no atoms for a fully magnetized vector) at the expense of quadratic, rather than linear, sensitivity to the angle. The population of $m_F = 0$ atoms is

$$P_{m_F=0} = n(\vec{x})\,\theta_{\text{avg}}^2\left(\frac{3}{4} + \cos\vec{k}\cdot\vec{x}\,\cos\omega t + \frac{1}{4}\cos 2\vec{k}\cdot\vec{x}\right). \tag{5.10}$$

For each image in our dataset, we calculated the power spectral density $S(\vec{q})$—the absolute value squared of the two-dimensional fast Fourier transform—and compare the power in the peak at $\vec{k}$ to the peak at zero momentum.

$$C(\vec{k}) = \frac{\sum_{\text{box around } \vec{q}=+\vec{k}} S(\vec{q}) + \sum_{\text{box around } \vec{q}=-\vec{k}} S(\vec{q})}{\sum_{\text{box around } \vec{q}=\vec{0}} S(\vec{q})} = \frac{2\sum_{\text{box around } \vec{q}=+\vec{k}} S(\vec{q})}{\sum_{\text{box around } \vec{q}=\vec{0}} S(\vec{q})}$$

If our data were described by Eq. 5.10, we would expect $C(\vec{k}) = \frac{2}{9}\cos^2\omega t$, close to the experimentally measured contrast at low momenta. For larger values of $|\vec{k}|$, the imaging resolution of our system further reduces contrast.

5.3.3 First data and systematic errors

Our first attempt immediately led to a clean oscillation and we managed to take a dataset that matched the quadratic dispersion relation and the expected mass (Fig. 5.7).

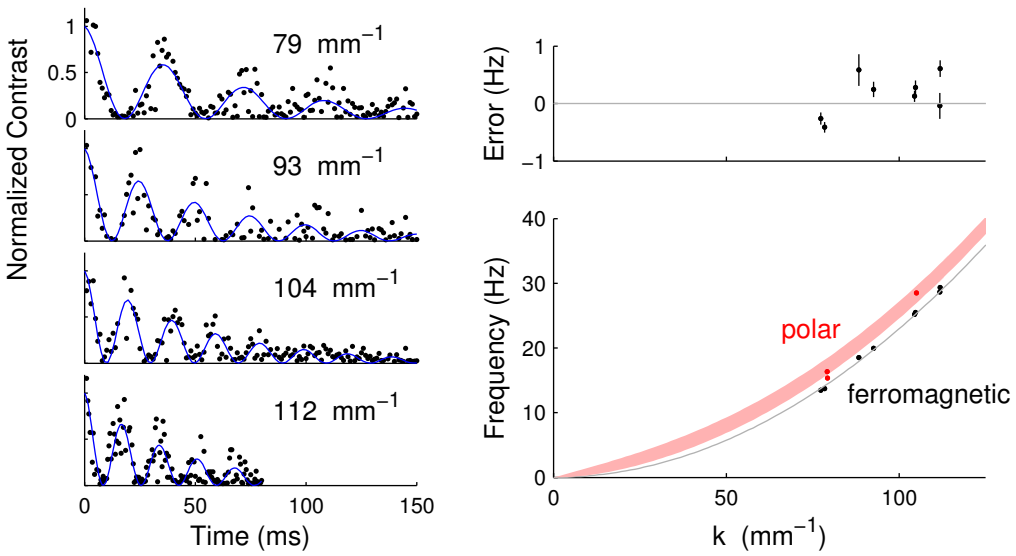

Figure 5.7: Initial magnon contrast interferometer data. (a) Contrast curves versus time for the ferromagnetic magnon (normalized to 1). The rapid decay in contrast is due to vortices created during condensation. (b) Dispersion relation for our first try (April 1, 2013). The values agree with mean-field theory (black line) better than the final data set does. Also shown are three points taken for polar magnons when $q > 2c_2n$, where the uncertainty in the theory arises from an uncertainty in the density.

Unlike in a typical recoil frequency experiment, we optically image the spatial fringe pattern. This allowed us to find several sources of error that led to loss of contrast and biased frequencies. For example, we found that after a single oscillation, the fringe pattern was garbled and uneven (Fig. 5.8). In the next several months, we identified and solved six major problems with the experiment, listed from most important to least.

1. The calibration of the magnon wavelength must be better than 0.5% to measure an effective mass with systematic error of better than 1%.

2. The eigenfrequency increases with magnon density due to nonlinear (interaction) shifts as $\Delta f \propto \theta_{\rm avg}^2 \propto n_{\rm magnon}$. We calibrated the shift versus population of $m_F = 0$ atoms at two wavevectors and interpolated the dataset. The shift is similar to a numerical simulation of our system with spin-independent contact interactions.

3. While the contrast interferometer removes the effect of magnetic field gradients and accelerations, magnetic field gradients cause a frequency chirp of the recoil frequency[2]. The magnetic field gradient is independently calibrated in our system (see Sec. 5.4 and Fig. 5.17).

[2]We neglected this effect until it was pointed out by referee during peer review of our article.

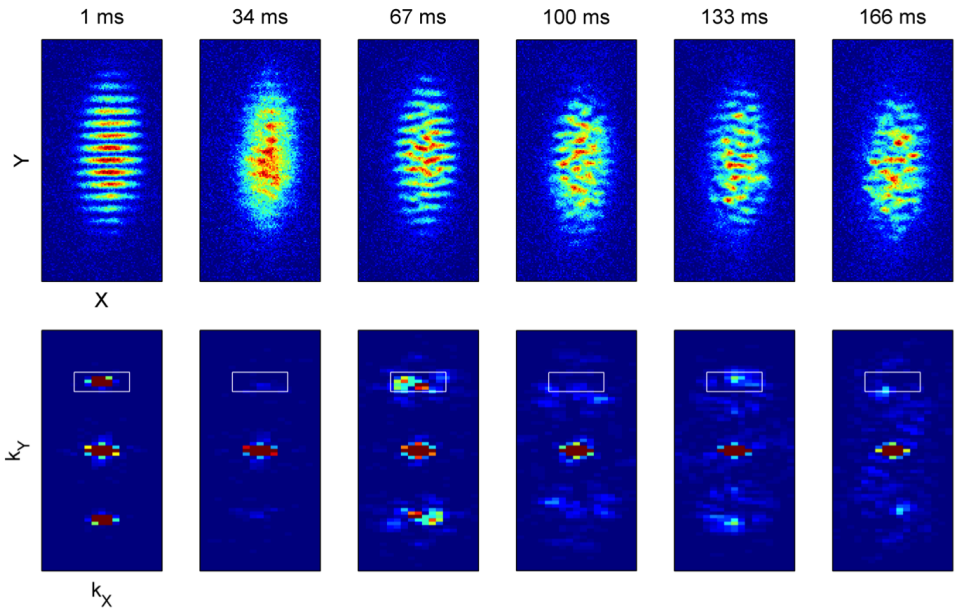

Figure 5.8: Loss of contrast due to vortices. Real space (top) and Fourier space (images) of the 65/mm pattern in a sample full of vortices. The images are shown roughly every half cycle. The inhomogeneous decay and fringe pattern is due to a large number of vortices produced by condensing the sample too quickly. For instance, the 67 ms image contains roughly a dozen vortices.

4. In the initial realization of the magnon interferometer, we cooled the condensate too rapidly and produced a large number of vortices. These vortices caused a rapid decay of the fringe contrast. This was solved by an extremely slow evaporation profile when ramping through the BEC critical point. This also establishes the magnon contrast interferometer as a method to investigate vortices (see Sec. 5.5.1).

5. Ambient noise somehow drives shape oscillations of the condensate, which adds phase shifts to the interferometer. We run the contrast interferometer 20 times per oscillating condensate, timed to sample several phases of the quadrupole oscillation, the main shape oscillation we observe. Averaging the several contrast runs per condensate efficiently removes the phase shift from the quadrupole oscillations.

6. Many collective excitations experience frequency shifts with temperature. We observe an increasing frequency with temperature, but we do not see a convincing trend in the region of temperatures that the data was taken. We do not apply a correction based on temperature.

5.3.4 Calibrating the length scale

Our original goal for this experiment was to look for a shift of several 10^{-3} in the effective mass of a magnon, as predicted in Ref. 60. In fact, what we are after is h/m^*, which has units of length^2/time. It is therefore necessary to calibrate the length scale at

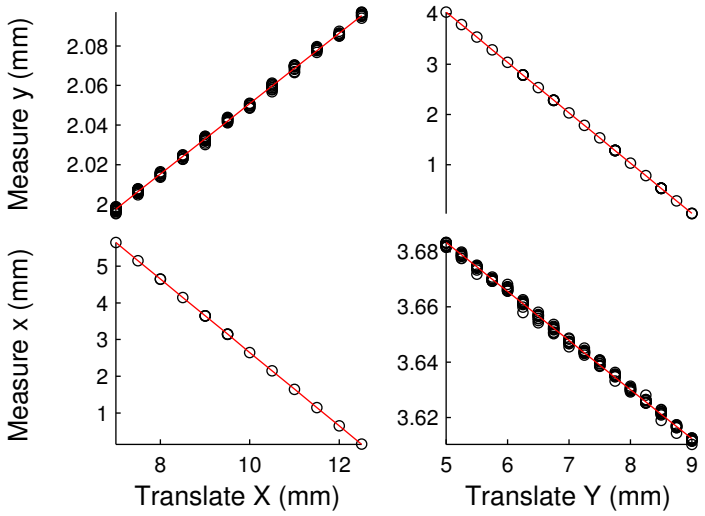

Figure 5.9: Calibration of the CCD pixel spacing. The CCD under test measures the x and y position of a focused laser with an assumed pixel size of exactly 2.2 μm. The shift in position is recorded against translating the camera with micrometer screws along perpendicular x and y axes. Fitting to a model of a rectangular array of pixels and assuming that the translation axes x and y are at right angles (red line), we find a pixel spacing of 2.19978(8) μm by 2.2006(1) μm and an angle of 1.017(8)°, where only the statistical noise is included. The root-mean-square residual is 1.2 μm and peak error is 2.8 μm over 320 measurements. We report this measurement as being consistent with square pixels spaced by 2.20(1) μm, where the large error should more than account for misalignments. The translation stage is aligned such that translation along z produces a minimal shift, with an angular error of less than 1 mrad and contributes negligibly to the calibration error. The NewFocus 562 translation stage specifies <100 μrad tolerances on the right angles. The NewFocus SM-13 and HR-13 micrometers specify 1 μm and 0.5 μm sensitivities, respectively, which suggests an accuracy at that level.

or below the part-per-thousand level. In a precision recoil experiment, the length scale is calibrated against a retroreflected laser of known frequency and wavefront. This calibrated ruler can have an accuracy of several parts in 10^{-10}, which remains the largest systematic error in measuring the recoil frequency in an atom [61]. However, in our experiment, we intersect the two lasers at a small angle. This dramatically reduces the accuracy of the measurements; here we work hard to reach 10^{-3}!

We measure the wavelength of the interference pattern *projected along the condensate axis*, $|(\vec{k}_1 - \vec{k}_2) \times \hat{n}|$, where $\hat{n}$ is the unit vector along the tightest trap frequency. If the condensate serves as a waveguide for magnons, this projection is more important than $|\vec{k}_1 - \vec{k}_2|$. The diffracted wavevector of magnons is $\vec{q} = ((\vec{k}_1 - \vec{k}_2) \times \hat{n}) \times \hat{n}$. In our alignment procedure, we set $\hat{n}$ is parallel to gravity. The following is our list of instructions to complete this alignment procedure.

Level the BEC against gravity. We measure the displacement of the BEC in a weak optical trap and in one that is recompressed. We first adjust the alignment of the optical trap and perform fine adjustments with the level of the floating optical table.

During this procedure, we verify that the magnetic field gradient is negligible. This ensures that the long axis of the BEC, through which magnons propagate, is perpendicular to gravity. We find an offset of less than $\Delta y = 30$ μm along the direction with trap frequency $\omega_y = 2\pi \times 4$ Hz. This constrains the angle to $\Delta y\, \omega_y^2/g \approx 2$ mrad.

Align a perpendicular reference laser. We align a reference laser that (1) propagates antiparallel to gravity and (2) passes through the center of the BEC. We align it to gravity by retroreflecting the laser off of a mirror whose front surface is referenced to an accurate bubble level. We verify that is passes through the atoms by imaging it on the camera used for absorption imaging. The angular error is less than 1 mrad.

Align the spin grating to the reference laser. A downward propagating laser is aligned to the reference laser at more than two points. This beam therefore is aligned to the atoms and is parallel to gravity. In this case, we used one of the two arms of the spin grating, which is focused on the atoms. The two lasers are well aligned over two meters and contribute a negligble angular error.

Align the CCD surface to the spin grating. A mirror is placed between the objective and atoms to divert the light onto a CCD camera with a small pixel size of 2.20 μm (Allied Vision Technologies, Guppy PRO F-503). We match the distance between the objective and atoms to the objective and camera by placing the camera at the focus of laser beam that was previously focused on the condensate. The laser beam has a 12 μm $1/e^2$ radius, and the relative alignment is well within the Rayleigh range of 0.5 mm. We also verify that the measured spin grating wavelength changes negligibly with camera position over several mm. Then, we align the translation stage to match the propagation of the reference laser, and align the CCD tilt to retroreflect the reference laser. However, since the camera is at the focus of the 200mm objective lens, we can only use the space between the camera and objective to align the retroreflection. This limits the accuracy of the entire procedure to 5-10 mrad.

Calibrate the CCD pixel spacing. We calibrate tha the CCD pixel spacing is $2.20(1)_{\mathrm{sys}}$ compared to fine micrometers (Fig. 5.9). We focus a laser onto the CCD and ensure that the position of the laser does not change when the CCD is translated towards the laser. Then, we tilt the CCD to ensure a retroflection, again at an accuracy of 5-10 mrad. Finally, we record the position of the laser on the CCD as a function of the two perpendicular micrometers. This measurement was performed after the experiment was completed.

Once aligned, the plane of the atoms matches the plane of the CCD camera through the mirror. As the optical table angle drifts, the alignment should remain correct, insofar that both the condensate and camera tilt together. For this reason, we correct tilts by adjusting the tilt of the optical table, and not the optical trap, which would ruin the above alignment procedure. A very conservative error estimate of 20 mrad leads to an error of $1-\cos(20\text{ mrad}) \approx 2\times10^{-4}$ in determining the spin grating wavelength, or a 4×10^{-4} in the estimated magnon frequency. To shift the data by 1%, we would need a huge misalignment of 100 mrad (6°).

5.3.5 Magnon density shift

Ideally, we would measure the dispersion relation of a single magnon by exciting one condensate atom into a superposition of spin and momentum states. Our experiment cannot measure such a tiny signal. Instead, we create $\sim 10^4$ magnons and measure the shift with magnon density as a function of the average tilt angle ($\theta_{\rm avg}$). As shown in Fig. 5.10 and Fig. 5.11b, the contrast signal oscillates more rapidly with increasing tilt angle. We correct all of the measurements in the dispersion relation by extrapolating towards $\theta_{\rm avg} \to 0$.

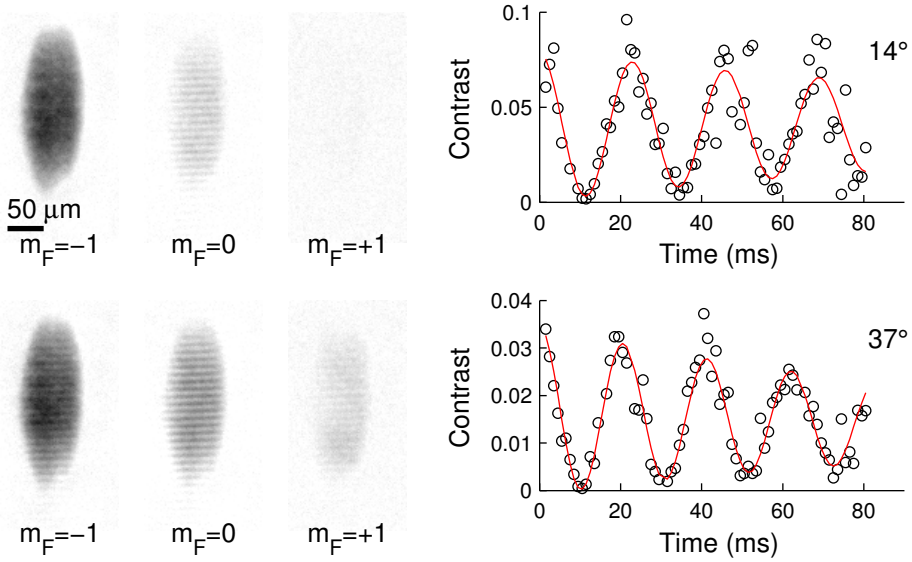

Figure 5.10: Density shift of the magnon contrast interferometer. (Left) images of the three m_F states for two different angle ($\theta_{\rm avg} = 14°$ and $37°$). At small angles only the $m_F = 0$ image shows fringes, whereas the $m_F = +1$ images has a negligible population. At larger angles, the $m_F = -1$ and $m_F = +1$ images show clear fringes. All images are normalized to the same peak density. (Right) The frequency of the contrast in the $m_F = 0$ increases dramatically with increasing angle (see Fig. 5.11b). The fringe frequency is 98/mm (10 μm wavelength).

We measure the tilt angle through the average Rabi frequency ($\Omega_{\rm avg}$) by counting the number of atoms in each m_F state for various pulse times (see Fig. 5.10 left and Fig. 5.11a). The measurements match theory at this wavenumber, based on integrating the populations from Eq. 5.9 over position.

$$\begin{aligned}
\langle P_{m_F=+1} \rangle &= \frac{3}{8} + \frac{1}{2} J_0(\theta_{\rm avg}) \cos\theta_{\rm avg} + \frac{1}{8} J_0(2\theta_{\rm avg}) \cos 2\theta_{\rm avg} \\
\langle P_{m_F=0} \rangle &= \frac{1}{4} \left(1 - J_0(2\theta_{\rm avg}) \cos 2\theta_{\rm avg}\right) \\
\langle P_{m_F=-1} \rangle &= \frac{3}{8} - \frac{1}{2} J_0(\theta_{\rm avg}) \cos\theta_{\rm avg} + \frac{1}{8} J_0(2\theta_{\rm avg}) \cos 2\theta_{\rm avg}
\end{aligned}$$

J_0 is the Bessel function of the first kind. We will frequently use the small angle expansion

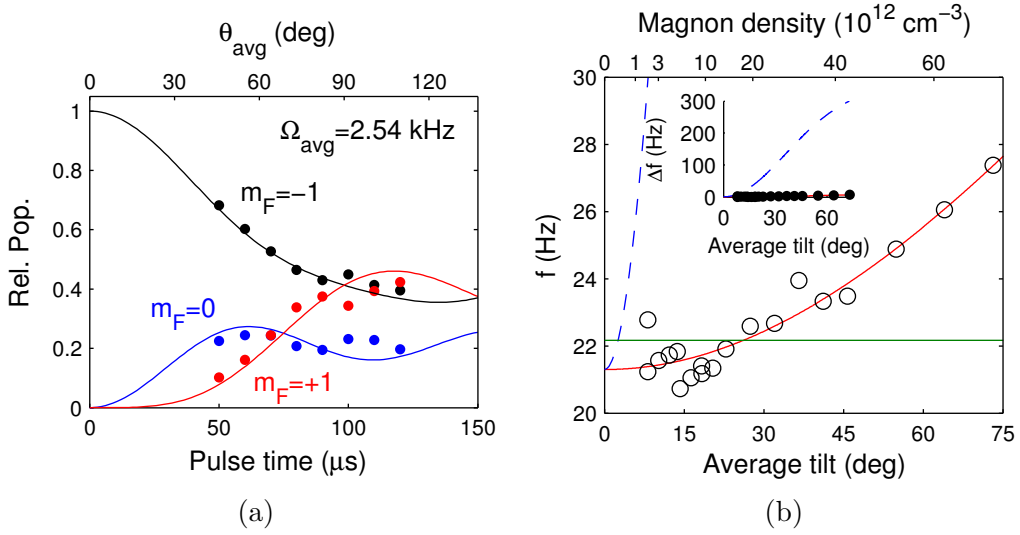

Figure 5.11: Density shift of the magnon contrast interferometer. Relative population as a function of spin grating pulse time. Each image is normalized to remove atom number fluctuations, we fit an undercounting of the $m_F = 0$ population by 1.7. The fit average Rabi frequency is 590 Hz. The data is taken for magnons with wavenumber 98.27/mm with an extrapolated frequency of 21.39 Hz, 3.5% smaller than the mean-field prediction of 22.16 Hz. The empirical density-dependent shift is 4.3(2) Hz/rad^2 or 4×10^{-5} Hz/$N_{m_F=0}$.

and identify $\langle P_{m_F=0} \rangle$ as the magnon fraction.

$$\frac{n_{\text{magnon}}}{n} = \frac{3}{4}\theta_{\text{avg}}^2$$

Unfortunately, at a lower wavenumber, we have had significant (factor of 2) disagreement between the angle determined by comparing the three ratios $\langle P_{m_F} \rangle$ and by comparing the number of $m_F = 0$ atoms against the total atom number. In the final dataset, we correct the density shift by empirically measuring the frequency shift per number of imaged $m_F = 0$ atoms rather than frequency shift per θ_{avg}^2.

Numerical calculation of the density dependent shift

The frequency shift with magnon density can be calculated from first principles by numerically integrating the Gross-Pitaevskii equation in one-dimension. I implemented a split-step Fourier method of a magnon standing wave in a box with uniform density and periodic boundary conditions [62, Sec. 3.3.1]. For simplicity, all numerics shown here were performed with only spin-independent interactions ($c_2 = 0$). A separate simulation with spin-dependent contact interactions show nearly the same behavior over our experimental range. The simulations disagree substantially for wavenumbers smaller than those accessed in the experiment, when $c_2 n > \hbar\omega$.

The numerical simulation show a frequency shift proportional to θ_{avg}^2. For each wavenumber, the simulation estimates a frequency f at 7 amplitudes up to $\theta_{\text{avg}} = 0.6$ rad

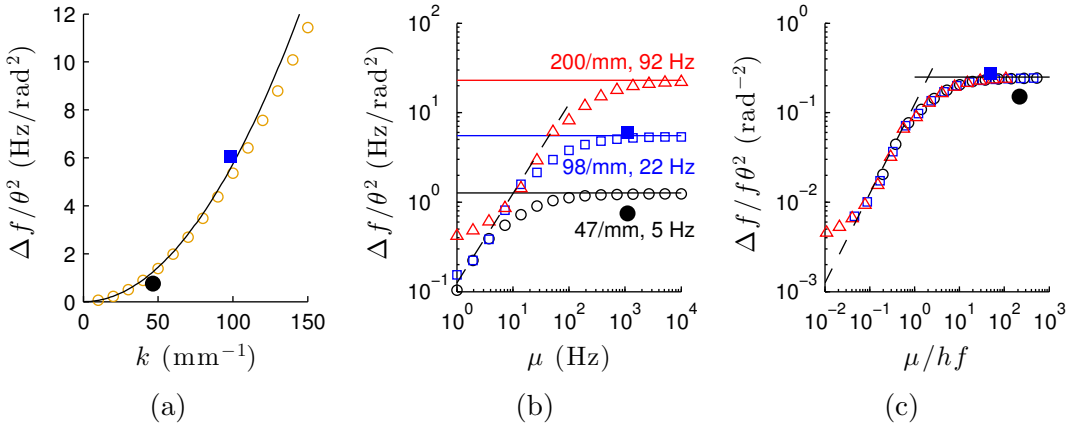

Figure 5.12: Numerical simulation of the magnon interferometer shows a pronounced frequency shift with density. For each wavenumber k and chemical potential μ, we simulate the interferometer for seven initial amplitudes and fit the resulting frequencies to a model with $\Delta f \propto \theta_{\rm avg}^2$. (a) At a chemical potential of $h\times 1$ kHz (open orange circles), the frequency shift increases dramatically with wavenumber. The simulation fits well to the high-density model $\Delta f = f_0\theta_{\rm avg}^2/4$ (black line) and is reasonably close to the two experimentally measured values (closed black circle at 47/mm and closed blue square at 98/mm). (b) The frequency shift (calculated at three wavenumbers) shows two regimes as a function of the chemical potential: a linear dependence on μ when $h\mu \ll f$ (dashed black line) and a saturated behavior for $h\mu \gg f$ (solid lines). (c) The same data collapses onto a single curve when the fractional frequency shift $\Delta f/f$ is plotted against the normalized chemical potential μ/hf. All simulations assume a uniform potential with spin-independent interactions only ($c_2 = 0$ and no dipolar interactions are included).

and fits the frequencies to a model with $f = f_0 + \Delta f\theta_{\rm avg}^2$. The results are identical for simulations with small grid sizes (in both time and position) and for much smaller amplitudes.

The main result of these simulations is Fig. 5.12. The simulations confirm the magnitude of the shift to within a factor of 2. The error is most likely due to inconsistencies in calibrating θ in the experiment. Fig. 5.12c demonstrates that the fractional frequency shift $\Delta f/(f\theta_{\rm avg})^2$ depends only on the dimensionless ratio $\mu/(hf)$. The simulated data show two regimes, when $\mu \gg hf$ and $\mu \ll hf$.

$$f = f_0 + \frac{\mu}{8h}\theta_{\rm avg}^2 = f_0 + \frac{c_0 n_{\rm magnon}}{6h} \qquad \mu \ll hf_0$$
$$f = f_0\left(1 + \frac{1}{4}\theta_{\rm avg}^2\right) = f_0\left(1 + \frac{n_{\rm magnon}}{3n}\right) \qquad \mu \gg hf_0$$

We can analytically calculate the frequency shift in the regime $\mu \ll hf_0$ with perturbation theory. The initial condition of the wavefuction up to $O(\theta_{\rm avg}^4)$ is as follows.

$$\psi(t=0) = \begin{pmatrix} \frac{1}{2}(1+\cos\theta) \\ -\frac{1}{\sqrt{2}}\sin\theta \\ \frac{1}{2}(1-\cos\theta) \end{pmatrix} \approx \begin{pmatrix} 1 - \frac{1}{4}\theta^2 \\ -\frac{1}{\sqrt{2}}\theta \\ \frac{1}{2}\theta^2 \end{pmatrix} \approx \begin{pmatrix} 1 - \theta_{\rm avg}^2\left(\frac{3}{8} + \frac{1}{2}\cos kx + \frac{1}{8}\cos 2kx\right) \\ -\frac{1}{\sqrt{2}}\theta_{\rm avg}\left(1+\cos kx\right) \\ \theta_{\rm avg}^2\left(\frac{3}{8} + \frac{1}{2}\cos kx + \frac{1}{8}\cos 2kx\right) \end{pmatrix}$$

In the limit of negligible interactions, we replace $\cos nkx$ with $e^{-in^2\omega_0 t}\cos nkx$, where $\omega_0 = \hbar k^2/2m = 2\pi f_0$.

$$\psi_{gn\to 0}(t) = \begin{pmatrix} 1-\theta_{\text{avg}}^2\left(\frac{3}{8}+\frac{1}{2}e^{-i\omega_0 t}\cos kx+\frac{1}{8}e^{-i4\omega_0 t}\cos 2kx\right) \\ -\frac{1}{\sqrt{2}}\theta_{\text{avg}}\left(1+e^{-i\omega_0 t}\cos kx\right) \\ \theta_{\text{avg}}^2\left(\frac{3}{8}+\frac{1}{2}e^{-i\omega_0 t}\cos kx+\frac{1}{8}e^{-i4\omega_0 t}\cos 2kx\right) \end{pmatrix}$$

For weak interactions ($\mu \ll hf_0$), we can add spin-independent interactions as a perturbation. We will assume that the perturbation is of the form $V = c_0\sum_i |\psi_{c_0 n\to 0}|^2$, as above. In the three-level basis $\{1, \cos kx, \sin kx\}$, the perturbation is diagonal.

$$V \Leftrightarrow c_0 n \begin{pmatrix} 1 & 0 & 0 \\ 0 & 1+\frac{1}{8}\theta^2 & 0 \\ 0 & 0 & 1-\frac{1}{8}\theta^2 \end{pmatrix}$$

The asymmetry between cosine and sine oscillations occur because our ansatz assumes the original oscillation is a cosine. This also suggests the the frequency shift depends on the type of interferometer used. Indeed, an interferometer that excites only $q = 0$ and $q = +k$ has a different dependence on θ. For the contrast interferometer, the frequency shift is the difference between the standing (1) and oscillating ($\cos kx$) states and is proportional to θ^2, as expected.

$$f = f_0 + \frac{c_0 n}{8h}\theta_{\text{avg}}^2$$

For small angles, $n_{\text{magnon}}/n = \frac{3}{4}\theta^2$. Then the frequency shift has the form

$$\Delta f = \frac{1}{6}\frac{c_0 n_{\text{magnon}}}{h}$$

or 1/6 the shift of a uniform, scalar, dilute interferometer.

5.3.6 Magnetic field curvature

The contrast interferometer removes phase shifts due to gradients because it measures the phase difference $\phi_{+k} + \phi_{-k} - 2\phi_0$, where ϕ_q is the phase shift accrued by the arm with momentum q. However, the contrast interferometer is susceptible to curvatures. In our setup, the curvature is due to an inhomogeneous magnetic field that creates an anti-trapping potential for magnons (see Eq. 5.6).

$$V_{\text{eff}}(y) = \mu\left[B(y) - B(0)\right] \approx -\frac{1}{2}\mu\frac{d^2|B|}{dy^2}y^2 = -\frac{1}{2}m\Gamma^2 y^2 \qquad \Gamma = \sqrt{\frac{\mu}{m}\frac{d^2|B|}{dy^2}}$$

Here, Γ takes the place of the usual harmonic oscillator angular frequency. The equation of motion in a harmonic anti-trapping potential is $\ddot{y} = \Gamma y$. The measured magnetic field curvature is $(h/\mu) \times 0.74$ mHz/μm^2 along the y direction (see Fig. 5.17), so $\Gamma = 1.8$ Hz. Most of the curvature is due to the inhomogeneous magnetic field of the lab and not dipolar interactions: without dipolar interactions, Γ would be 20% smaller.

We start the magnon interferometer by uniformly placing the atoms in a superposition of momentum states $q = 0, \pm k_0$. Over time, the atoms will accrue a phase due to the local potential $V_{\text{eff}}(y)$. In addition, the momentum changes as they propagate, which in turns gives an extra phase shift to the interferometer. The overall phase should be proportional to the action of the classical trajectory. For the interference pattern at the center of the condensate after an evolution time τ, the classical trajectory has the boundary conditions that the initial velocity is $\dot{y}(0) = v_0 = \hbar k_0/m$ and the final position is $y(\tau) = 0$.

$$y = \frac{v_0}{\Gamma}\frac{\sinh\Gamma(t-\tau)}{\cosh\Gamma\tau} \qquad v = v_0\frac{\cosh\Gamma(t-\tau)}{\cosh\Gamma\tau}.$$

The phase shift is proportional to the action acquired over the time τ.

$$\begin{aligned}
\phi &= \frac{m}{2\hbar}\int_0^\tau dt\left[\dot{y}^2 + \Gamma^2 y^2\right] \\
&= \frac{m}{2\hbar}\int_0^\tau dt\left[\frac{v_0^2\cosh^2\Gamma(t-\tau)}{\cosh^2\Gamma\tau} + \frac{v_0^2\sinh^2\Gamma(t-\tau)}{\cosh^2\Gamma\tau}\right] \\
&= \frac{mv_0^2}{2\hbar}\int_0^\tau dt\frac{\cosh 2\Gamma(t-\tau)}{\cosh^2\Gamma\tau} \\
&= \frac{mv_0^2}{2\hbar}\frac{\tanh\Gamma\tau}{\Gamma} \\
&= \frac{\hbar k_0^2}{2m}\frac{\tanh\Gamma\tau}{\Gamma}
\end{aligned}$$

As Γ tends to zero, we recover the usual $\phi = \omega_0\tau$. All fits to the contrast oscillations include the frequency chirp, with fixed $\Gamma = 1.8$ Hz, variable damping coefficients γ, A, B, D, and a frequency $2\pi f = \omega_k - \omega_0$.

$$C(t) = A + e^{-\gamma t}\left[B + D\cos\left(2(\omega_k - \omega_0)\frac{\tanh\Gamma t}{\Gamma}\right)\right] \tag{5.11}$$

5.3.7 Vortices and decay of contrast

We were initially puzzled by the images of the contrast decay with warped magnon wavefronts but high contrast (Fig. 5.8, 67ms frame). We correctly guessed that these were due to large phase fluctuations across the condensate, yet further evaporative cooling did not appear to remedy the situation. Once we began to take multiple images of the same condensate, it was clear that we had unwittingly created a vortex detector! We reduced the number of vortices by cooling the condensate extremely slowly, with a 4–6 second ramp in the immediate vicinity of the BEC critical temperature. In Sec. 5.5.1, we adjust to cooling rate to create one vortex on average and demonstrate a real-time vortex tracker.

5.3.8 Shape oscillations

The trap frequencies of $2\pi \times (4, 9, 300)$ Hz used in this experiment were quite low, and unfortunately the floating optical table does little to damp vibrations in the room around the lowest frequency. In fact, there is a possibility that the table is underdamped and

amplifies noise at several Hertz. As we previously mentioned, the contrast interferometer should remove errors due to residual dipole oscillations. However, quadrupole oscillations, such as a breathing mode, can compress or expand the magnon wavevector and lead to errors. If the phase of oscillation were random, we could hope that the experiment would average out this effect. If, alternatively, the oscillation were started due to an error in the experiment such as a glitch of the optical trap intensity, our data might be biased by it. To remove this type of error, we perform 20 experiments of the magnon interferometer for each BEC we form, and we create magnons at a rate incomensurate with the quadrupole mode at 4.5 Hz. After we image the magnons, we remove all of the $m_F = 0$ and $m_F = +1$ atoms by simultaneously driving a microwave transition to the F=2 state and applying a resonant optical pulse on the D2, F=2 to F'=3 transition. This leaves a clean, $m_F = -1$ BEC to start the next magnon interferometer.

Fig. 5.13a shows the first 12 magnon contrast interferometers, all with a propagation time 79 ms, derived from the same oscillating BEC. During the oscillation, it is clear that both the wavevector and the contrast change. What contrast do we assign this run? Since we are equally sampling many phases of the oscillation, one answer is to average the contrast. An alternative approach is to measure the change in contrast versus wavevector, as shown in Fig. 5.13b. We fit a sinusoidal model for dC/dk and correct each image based on its wavevector change Δk (i.e., calculate a new contrast C' where $C' = C - \frac{dC}{dk}\Delta k$ for each image). The two approaches are shown in Fig. 5.13c and lead to the same measured frequency; therefore we believe we are properly controlling for this error.

5.3.9 Thermal shift and damping

Collective excitations of a condensate typically show a shift of the frequency with temperature. For instance, the frequencies of shape oscillations in a scalar condensate have been observed to either increase or decrease with temperature, depending on the mode [63, 64].

In Fig. 5.14a, we observe an increasing frequency of the magnon contrast oscillations with temperature. The final temperature is set by changing the intensity of the optical dipole trap at the end of evaporative cooling. For a wide range of trap depths, the contrast frequency falls below the expected mean-field estimate. This suggests that the unusually low recoil frequency is not due to thermal effects. We do not correct the data for a thermal shift.

In addition to a frequency shift, we observe a dramatic increase in the damping rate with temperature (Fig. 5.14b). This trend is commonly observed for phonons and shape oscillations in a scalar condensate [63, 64]. For phonons, the damping is often attributed to Landau damping, whereby the excitation scatters off of thermally occupied phonons [31, 30]. It is possible that magnons decay by a similar mechanism. Since the magnons are fluctuations of a broken symmetry, they are expected to be highly damped at the phase transition[3].

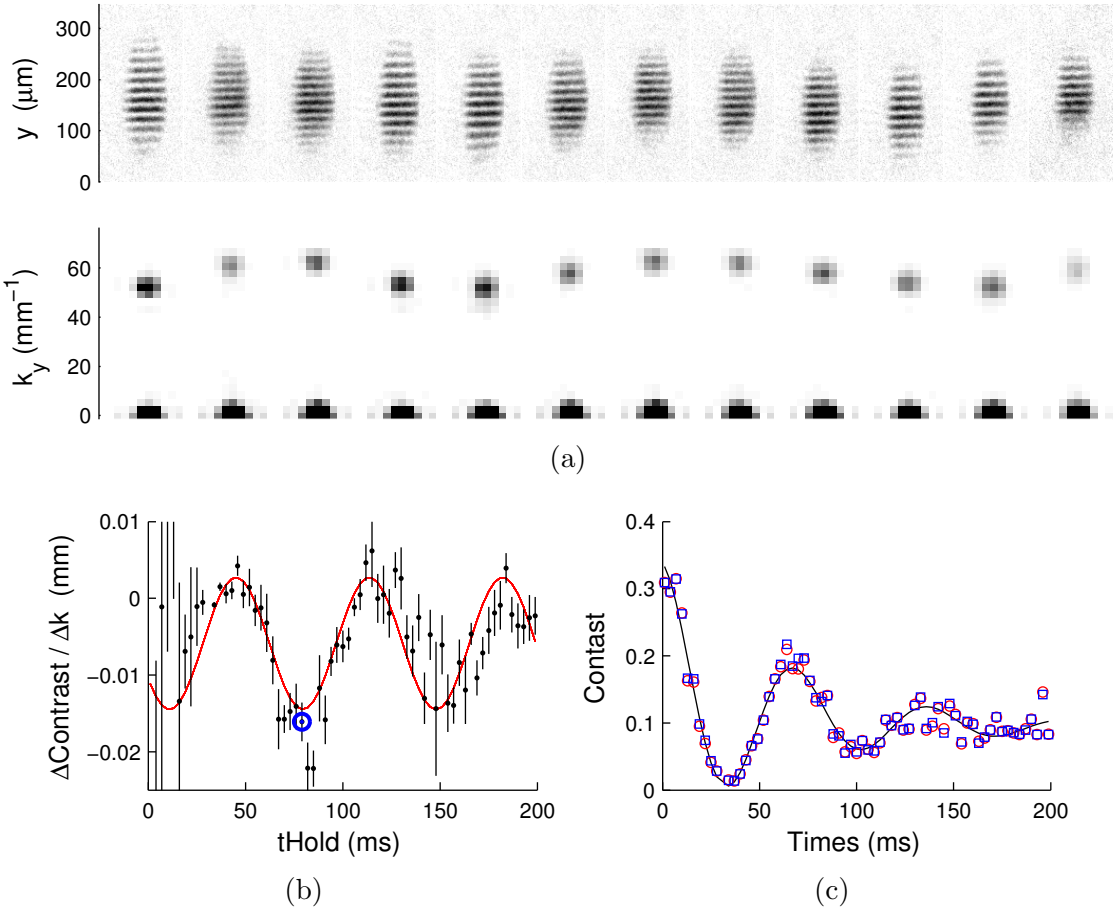

Figure 5.13: Quadrupole oscillations in the magnon contrast interferometer. (a) We run 20 magnon contrast interferometers in a single oscillating BEC for each propagation time. Quadrupole oscillations cause the standing wave to accordian (top), which shifts the measured wavevector k (bottom). (b) The change in contrast versus wavevector oscillates at the same frequency as the contrast signal. The blue circle at 79ms corresponds to the dataset shown in (a). The offset may be due to the linear decrease of the modulation transfer function with wavenumber. (c) The contrast oscillation is very similar for the averaged contrast signal (red) and corrected signal (blue). All data correspond to 56.6/mm. This dataset is a scan with 66 time steps of 20 images each, leading to a total of 1,320 contrast interferometer runs.

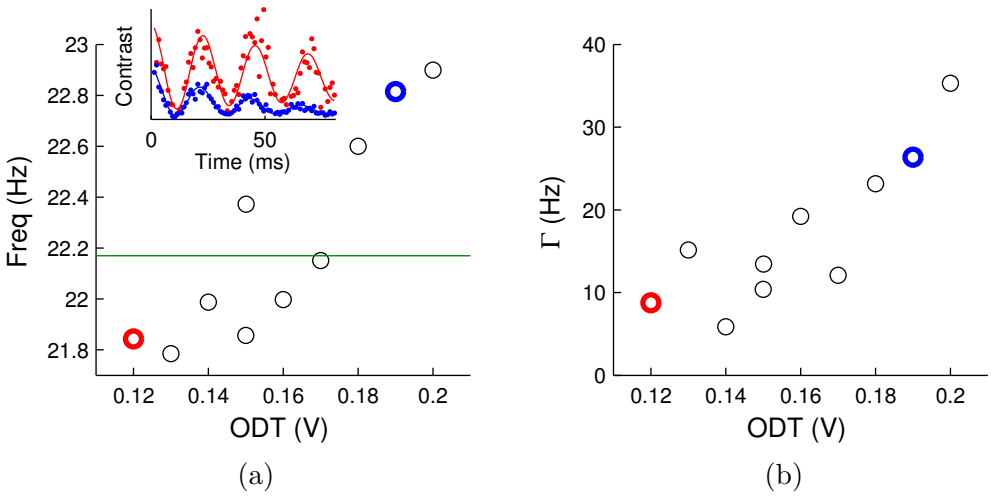

Figure 5.14: Thermal shift of the magnon contrast interferometer. (a) Magnon interferometer frequency and (b) damping rate as a function of temperature. The inset shows contrast oscillations at 0.12 V (red) and 0.19 V (blue). Unfortunately, the temperature was not well-calibrated in this setup. We observe a large thermal fraction above 0.18 V and a vanishing trap depth between 0.10 V and 0.11 V. The final data was taken at 0.12 V, where we do not detect an appreciable shift in the magnon frequency. The data remain well below the free particle result (solid green line) for a large range of trap depths, and so we are confident that the unusually low magnon frequency is not a thermal effect. We do not apply a thermal shift to the final data. The data are taken for magnons with wavenumber 98.27/mm and an expected mean-field result of 22.16 Hz, identical to Fig. 5.11.

5.3.10 Final data

Fig. 5.15a shows the final data run. The data were taken from 9pm–9am on the three nights from Friday, Aug. 23 through Monday, Aug. 26. During these hours, both elevators in the building were held on the ground floor, during which time the magnetic field environment was unusually quiet. We measured ∼1 mG fluctuations over many hours, with a correspondingly small magnetic field gradient fluctuations (Sec. 4.4.2). A scan of the frequency shift versus amplitude was taken at the lowest measured momentum, complementing the data previously taken in Fig. 5.11b. We subtracted a frequency shift proportional to the number of measured magnons. Between the calibrated values, we interpolate the frequency shift based on the measured magnon frequency.

5.4 Dipolar interactions and the many-body gap

The contrast interferometer naturally subtracts out an offset, or gap, in the dispersion relation. In this section we will complete our measurement of the dispersion relation by directly measuring the density-dependent component of $\omega(0)$.

The measured dispersion relation clearly shows that the minimum energy to create

[3]Thanks to Manuel Endres for pointing this out.

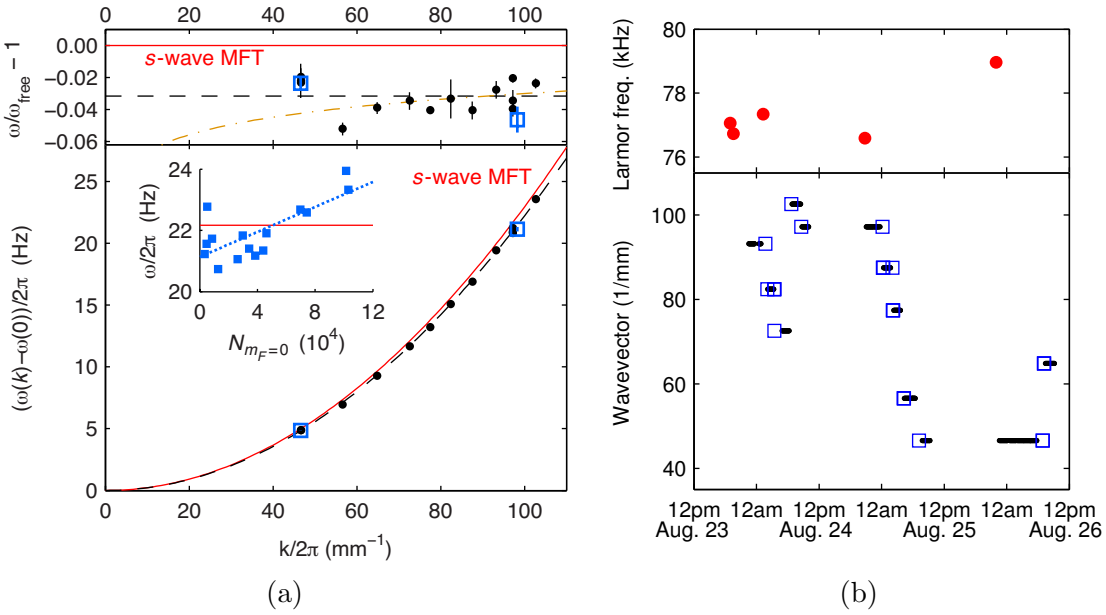

(a) (b)

Figure 5.15: (a) Dispersion relation from the final dataset. Individual scans at a single magnon population (filled black circles) follow a nearly quadratic dispersion relation (red dashed line), but with an effective mass $3.3(2)_{\mathrm{stat}}(10)_{\mathrm{sys}}\%$ heavier than the mean-field prediction for s-wave interactions (solid red line) for. A power-law fit to the data $\omega \propto k^{\alpha}$ yields $\alpha = 2.01(1)_{\mathrm{stat}}$ (dot-dashed orange line). All data is corrected for shifts from a finite magnon density, as calibrated by scans of the interferometer against magnon population (inset). Extrapolations of these calibrations towards zeros magnon population are shown as open blue squares. (b) Data taking schedule. Contrast interferometer sequences (bottom, filled black circles) are interspersed with calibrations of the standing wave momentum (bottom, open blue squares) and the magnetic field (top, filled red circles). Magnetic fields were stable during the relevant ~ 60 hour period. Not shown are checks and cancellation of the magnetic field gradient, which are very sensitive to fluctuations in the bias field. 22,801 magnon contrast interferometers were harmed in the making of this plot.

a magnon is $\hbar\omega(0)$, the energy of a $\vec{k}=0$ magnon. A zero momentum magnon is equivalent to a global rotation of spin, as seen in Eq. 5.5.

$$\begin{aligned}\psi_{\text{magnon}} &= \sqrt{n}\, e^{-i\mu t/\hbar} \begin{pmatrix} 1 \\ \frac{1}{\sqrt{2}}\theta e^{-i\left(\vec{k}\cdot\vec{x}+\omega(k)t\right)} \\ 0 \end{pmatrix} \\ &\xrightarrow{\vec{k}\to 0} \sqrt{n}\, e^{-i\mu t/\hbar} \begin{pmatrix} 1 \\ \frac{1}{\sqrt{2}}\theta e^{-i\omega(0)t} \\ 0 \end{pmatrix} \\ &= \sqrt{n}\, e^{-i\mu t/\hbar} R\left(\theta, \phi=\omega(0)t\right) \begin{pmatrix} 1 \\ 0 \\ 0 \end{pmatrix} \end{aligned} \tag{5.12}$$

We measure $\omega(0)$ by measuring the time-dependent evolution of the azimuthal phase ϕ.

If the Hamiltonian is spherically symmetric, a global rotation of the magnetization cannot change the energy and $\omega(0)=0$. In our system, symmetry is broken by a uniform bias field and by dipole interactions coupled to the anisotropic trap geometry. The uniform bias field introduces a preferred axis and an energy μB of magnetic excitations. The main impact of the large field is that it requires the global conservation of the longitudinal spin and M_z, though locally the spin is free to rotate (e.g., Fig. 5.6 shows the motion of longitudinal spin). By moving to a rotating frame, the impact of this energy scale disappears. For a more advanced discussion, see Ref. 65.

A more serious complication arises from dipolar interactions. In a spherical trap, dipolar interactions still cannot add a gap because the system remains spherically symmetric. However, our system is better approximated as a thin film because the $\hat{z}$ axis has a far tighter confinement, with a calculated Thomas-Fermi radius of 1.7 μm, than the in-plane directions, with measured Thomas-Fermi radii of 68 μm and 142 μm along $\hat{x}$ and $\hat{y}$, respectively. Once the spatial symmetry of the trap is broken, dipolar interactions can introduce an energy that changes with the magnetization direction. For instance, spins oriented in-plane and out-of-plane should have different energies.

A calculation of the dipolar energy shift effect is derived in Sec. 5.4.2. In summary, the rate of precession of the magnetization oriented an angle θ from the bias field, precessing about an in-plane bias field, and averaged over the $\hat{z}$ axis, depends on the local in-plane density and magnetic field.

$$\omega_{\text{prec}} = \frac{\mu}{\hbar}B + \Delta(n)\cos\theta \qquad \Delta(n) = \frac{2}{5}\frac{\mu_0\mu^2 n}{\hbar} \tag{5.13}$$

I call $\Delta(n)$ the *many-body gap* because it is a gap whose energy depends on the local density, as opposed to the single-particle gap created by the bias magnetic field.

As can be seen from the wavefunction in Eq. 5.12, an increased rate of precession about an effective magnetic field is the same as an energy shift because the magnon has a magnetic moment. In this case, the spin precession rate increases because of the real magnetic field induced by dipoles of the gas. We measure the gap by using the condensate as a local magnetometer, similar to Ref. 52 expect that we probe the magnetic dipole

field generated by the condensate itself. We measure a $2.5(1)_{\text{stat}}$ Hz dipole field, which in magnetic field units is 3.6 μG (360 pT) with a statistical error of 0.15 μG (15 pT).

5.4.1 Experiment

We measure $\Delta(n)$ by performing Ramsey interferometry in our inhomogeneous condensate. The density in the condensate changes only slowly with position, and we are free to make a local density approximation (LDA). In particular, we measure for a time short enough that the phase gradients do not move, and over a distance large compared to the dipolar healing length $\hbar/\sqrt{\mu_0\mu^2 m n_0} \approx 4$ μm.

Fig. 5.16 shows a schematic of the measurement and sample images, and is very similar to the proposal in Ref. 67. The condensate is prepared with the magnetization aligned precisely along the in-plane magnetic field. An RF pulse with variable pulse time rotates the magnetization to a polar angle θ. The condensate precesses in a magnetic field that is a combination of the local magnetic field and the induced dipolar magnetic field. After an evolution time of τ, the transverse magnetization acquires an azimuthal phase shift ϕ.

$$\phi(\vec{r}) = \frac{\tau}{\hbar}\left[\mu B(\vec{r}) + \Delta(n(\vec{r}))\cos\theta\right] \tag{5.14}$$

We extract $\Delta(n)$ by comparing the transverse phase to the local density. This comparison across the sample allows us to extract the several microgauss dipole field amidst milligauss fluctuations of the local field without resorting to spin echo pulses. The experimental difficulties lie in removing the inhomogeneities of the local magnetic field that can mask the dipole signal. Gradients are minimized by taking the data past midnight and manually nulling the magnetic field gradient between each 7 minute run. Fortunately, only 55 runs (six images each) were required for this measurement. Despite these efforts, gradients still vary during each shot of the experiment and are eliminated in the data analysis.

The laboratory environment also contains a magnetic field curvature. Both a magnetic field curvature and the dipolar field create a phase shift that scales quadratically with position across the condensate. We separate the effects by comparing the azimuthal phase shift with θ, which only changes the dipole contribution. Fortunately, the curvature is stable over the entire dataset. For each image of F_x, we fit a model of a magnetic field with a bias, gradient, and curvature. The form is intended to extract the phase shifts from Eq. 5.14.

$$\begin{aligned} F_x(x,y) &= F_{x,0} + \delta F \sin\phi(x,y) \\ \phi &= \phi_0 + \pi\tau\left(f_{xx}(x-x_0)^2 + 2f_{xy}(x-x0)(y-y0) + f_{yy}(y-y_0)^2\right) \end{aligned} \tag{5.15}$$

As seen in Fig. 5.17, f_{xx}—the curvature of the Larmor frequency along x—varies greatly with the magnetization angle. Our model of dipole interactions indicates that its contribution disappears at $\theta = \pi/2$. We can then subtract the magnetic field curvature by fitting to a model with free parameters $f_{ii,0}$ and $f_{ii,\pi/2}$.

$$f_{ii} = f_{ii,\Delta}\cos\theta + f_{ii,B} \qquad \Delta(n_0) = h \times \frac{1}{2}R_i^2 f_{ii,\Delta} \tag{5.16}$$

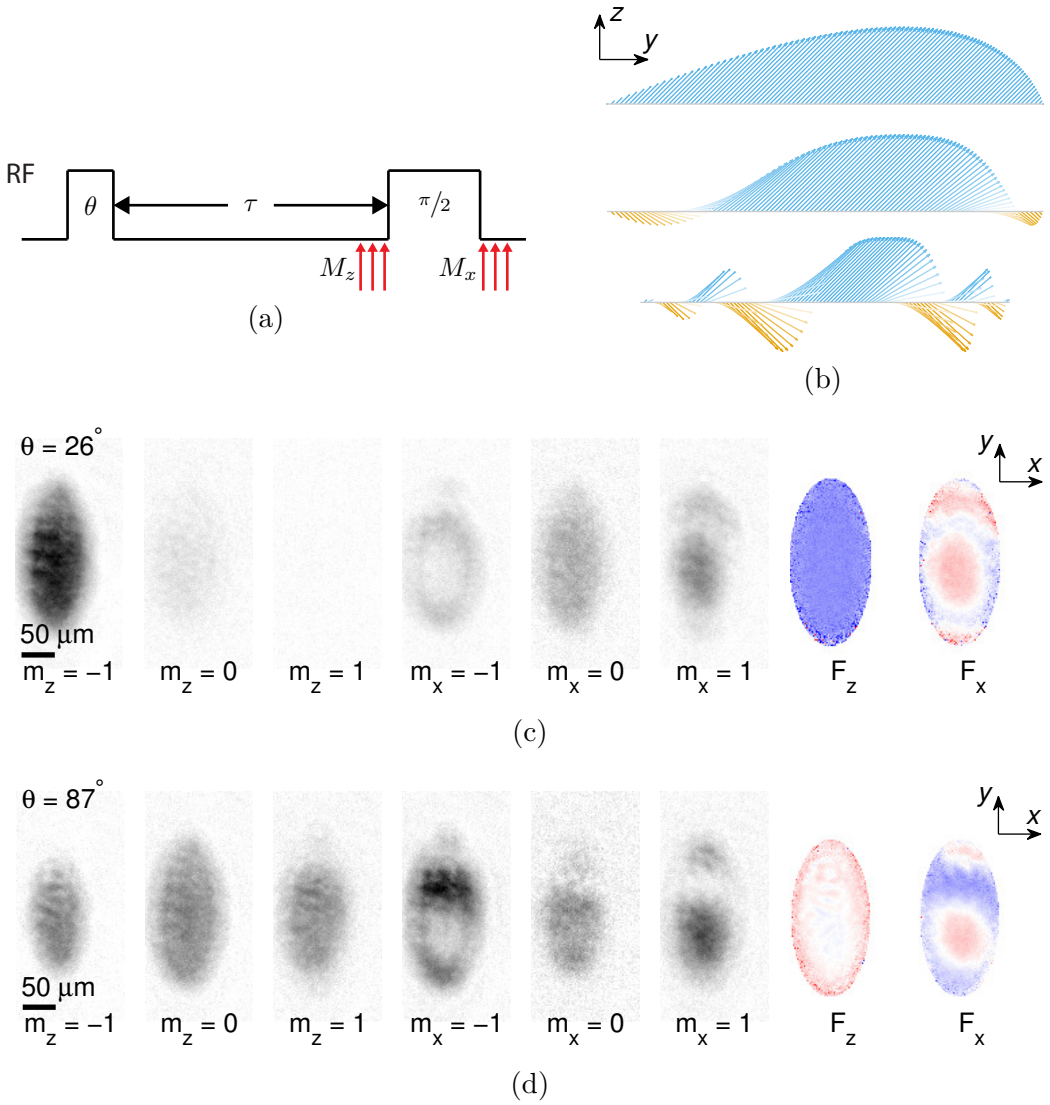

Figure 5.16: Spin precession in the presence of dipolar interactions. (a) Magnon imaging sequence. An RF pulse of variable time rotates the initial magnetization, which is allowed to evolve for 100–300 ms. (b) A calculation shows the azimuthal phase of the local magnetization winding up after a time $t = 0$, $\pi\hbar/\Delta$, and $4\pi\hbar/\Delta$. Arrows represent the magnetization of a line cut through the system. (c,d) Magnetization imaging for two angles, (c) 26° and (d) 87°. Images of the three F_z projections of the longitudinal spin are followed by images of the three F_x projections of the transverse spin. The reconstructed images are estimates of $\langle F_z \rangle = M_z/N$, the magnetization normalized by the density. The curvature of the azimuthal angle, the arcsine of F_x, is larger for small angles due to dipolar interactions. Nearly all of the transverse structure in (d) is due to an inhomogeneous magnetic field. Note that the longitudinal magnetization is smooth for small angles and acquires an inhomogeneous profile for large angles, similar to [66].

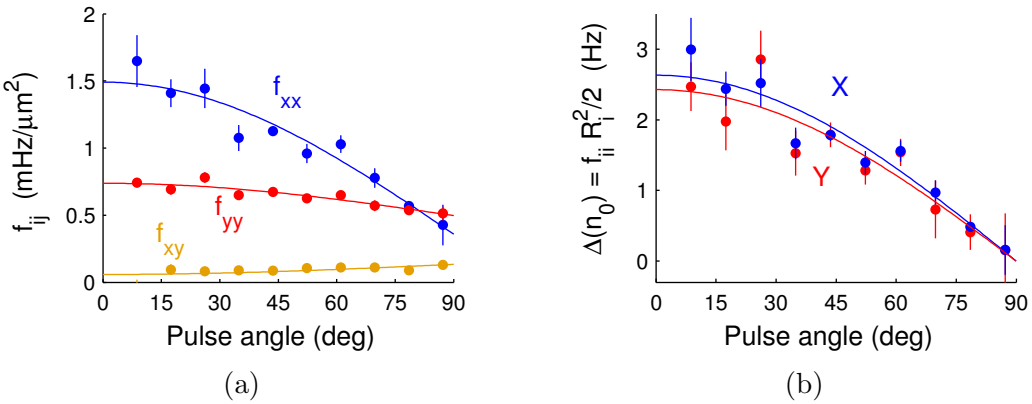

Figure 5.17: Curvature of Larmor precession due to dipolar interactions. (a) The second derivative of the precession frequency f_{ij} are based on fits to F_x. As expected, f_{xx} varies more rapidly with θ because the condensate density changes more rapidly along x. The cross-term f_{xy} is nearly constant. (b) We assume that the dipole contribution vanishes at $\theta = \pi/2$ and subtract the contribution from our data. The frequency difference betweens atoms at the center (at density n_0) and at the edge (zero density) is simply $f_{ii}R_i^2$ collapses on a line, strengthening our hypothesis that the curvature scales with local density. Each points represents the average of 5 runs with τ between 100 and 300 ms, and error bars are 1 σ standard errors.

The curvatures along x and y give nearly identical estimates of $\Delta(n_0)$, as expected for a frequency proportional to the local density (Fig. 5.17b). Our largest systematic error comes from uncertainty in the Thomas-Fermi radii, largely because of a slight anisotropy in the trap.

$$\Delta(n_0) = h \times 2.5(1)_{\text{stat}}(2)_{\text{sys}}$$

Gap map

The curvatures f_{ii} give the correct general form of the dipolar field. Since the system size is much larger than the dipolar healing length, very many regions of the gas can be considered separate experiments. We use this abundance of data to form a *gap map*, a map of the magnon gap across the sample. Eq. **??** indicates that the gap should vary with the local in-plane density.

The first step is to construct the gap map is to measure the local phase shift in each region of our image. Mathematical complications arise from phase unwrapping a 2D image. We use the fits from Eq. 5.15 to inform phase unwrapping. The fit determines the phase quadrant $[n\pi, (n+1)\pi)$ and the arcsine of the normalized magnetization determines the phase within the quadrant (Fig. 5.18). Artifacts in the phase occur at the phase boundary $n\pi$, which average down because each image has a random phase offset, fluctuating gradient, and variable τ. Phase offsets and gradients are subtracted from the data. We average independent runs to get a frequency map and fit for the local gap on a pixel-by-pixel basis with the model $f = \Delta\cos\theta + f_B$ (Fig. 5.19). Frequencies are measured relative to the edge of the condensate.

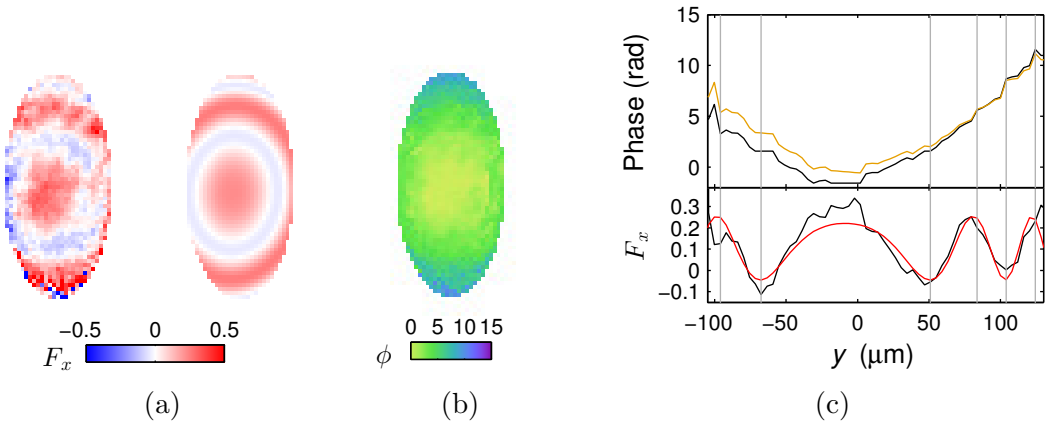

Figure 5.18: Phase unwrapping for gap map. (a) Measured (left) and fit (right) images of the F_x magnetization for an difficult-to-fit run (17°, 300 ms evolution time). The short-range structure is due to instability of the spin helix, which completely dissolves for longer evolution times [68]. (b) Unwrapped phase of the Larmor precession angle. (c) A cross-section of the center of these three plots along y. The magnetization (bottom, solid black line) wraps several 2π. The fit (bottom, solid red line) determines the regions where we add multiples of π to the unwrapped phase (vertical gray lines). The phase estimate (top, black line) within each region is the arcsine of the normalized magnetization. We then remove a gradient and offset phase (orange) to ensure that the relative phase is zero at the condensate center. All data is binned by 2x2 pixels to reduce noise.

We compare the resulting phase map with the in-plane density of the condensate from the longitudinal magnetizations in Fig. 5.19. The in-plane density n is related to the column density $\tilde{n} = \frac{4}{3}nR$, where R is the *local* Thomas-Fermi radius.

$$n(x,y,0) = \tilde{n}(x,y)^{2/3}\left(\frac{9m\omega_z}{32(c_0+c_2)}\right)^{1/3}$$

The measured column density is a small fraction of the total column density, lest we destroy the sample before we measure the transverse magnetization. However, the scaling factor was not well calibrated in this data. From the measured Thomas-Fermi radii and calibrated trap frequencies, we determine that we measure 5% of the atoms during each imaging pulse. The anharmonicity of the optical trap adds an error to this calculation. A pixel-by-pixel comparison of the gap and in-plane density shows a nearly linear behavior.

5.4.2 Calculation of the dipolar shift

Calculating the dipolar interactions is a straightforward problem in classical electromagnetism.

1. Calculate the induced $\vec{B}_m$ and $\vec{H}_m$ fields for a specific a magnetization density $\vec{M}$.
2. Calculate the torque on the rotating magnetization from this induced field.
3. Integrate the torque over the tightest condensate axis.

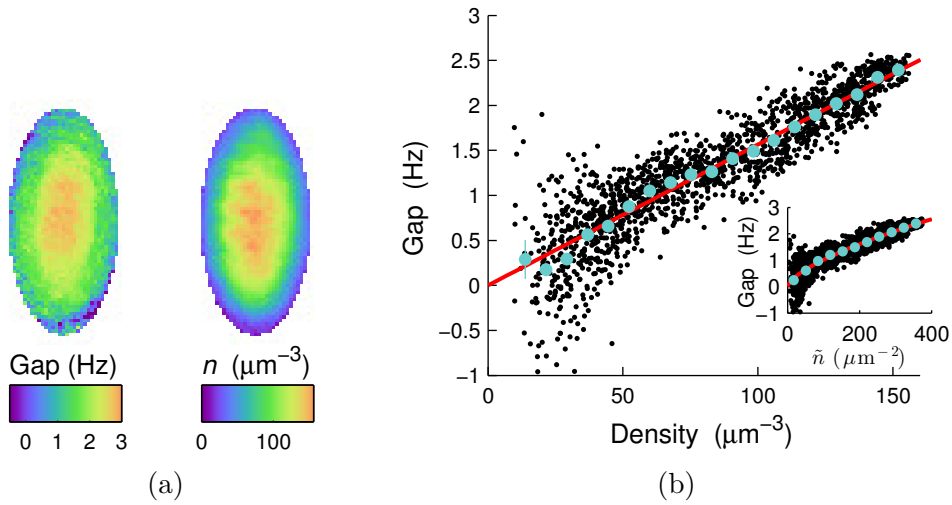

Figure 5.19: Gap map. (a) A pixel-by-pixel analysis of the local phase shows a magnon gap that varies in position. The map has ellipses of equal energy of nearly identical form to the in-plane density of the condensate. (b) Each 4.08×4.08 μm pixel yields an independent experiment comparing the gap versus local density. The data has a nearly linear fit. Errors may be due to high frequency imaging aberrations from scattering by dust that we discovered afterwards. (Inset) A fit of the gap to the local column density ($\tilde{n} \propto n^{2/3}$) deviates from a linear fit at low densities.

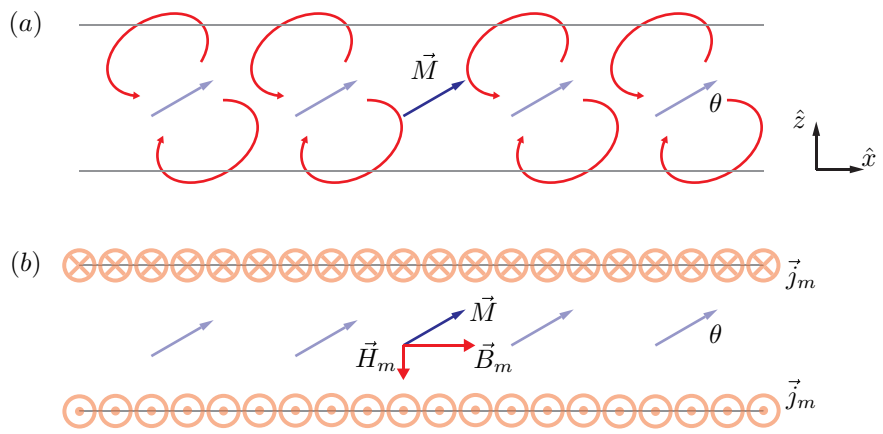

Figure 5.20: Dipolar interaction schematic. (a) A series of spins with magnetization $\vec{M}$ tilted an angle θ from the plane is equivalent to (b) an effective current density $\vec{j}_m$, which induces $\vec{B}_m$ and $\vec{H}_m$ fields.

Induced magnetic field

A block with magnetization density $\vec{M}$ will induce a magnetic field created by an effective current distribution $\vec{j}_m = \vec{\nabla} \times \vec{M}$. Our condensate is very thin in the z direction, so we assume the magnetization varies most strongly along z and weakly along the other two dimensions, $\partial \vec{M}/\partial x = \partial \vec{M}/\partial y = \vec{0}$. Without loss of generality, we'll have the magnetization

point an angle θ in the $x-z$ plane.

$$\vec{M} = \mu n(\hat{x}\cos\theta + \hat{z}\sin\theta)$$

$$\vec{j}_m = \hat{y}\,\mu\cos\frac{\partial n}{\partial z}$$

where $\mu = -\frac{1}{2}\mu_B$ is the magnetic moment and n is the condensate density. We need to solve the following equations [69, see Ch. 8].

$$\vec{\nabla}\cdot\vec{B} = 0 \qquad \vec{\nabla}\times\vec{B} = \mu_0\vec{j}_m$$

In this case, the solution depends only on the component of magnetization along the condensate.

$$\vec{B}_m = \hat{x}\,\mu_0\mu n\cos\theta$$

It is common and useful to define $\vec{H}_m = \frac{1}{\mu_0}\vec{B} - \vec{M}$, where $\vec{\nabla}\times\vec{H}_m = 0$.

$$\vec{H}_m = -\hat{z}\,\mu n\sin\theta$$

Fig. 5.20 shows a schematic of this solution.

Torque of the induced field on the atomic spins

The Larmor precession is due to torque on the atomic magnetization.

$$\frac{d\vec{M}}{dt} = -\frac{\mu}{\hbar}\,\vec{M}\times\vec{B} \tag{5.17}$$

The solution we are looking for is one where the magnetization precesses about the $\hat{x}$ axis at a rate ω, which self-consistently depends on the induced dipolar magnetic field.

$$\vec{M} = \mu\,(\hat{x}\,\cos\theta + \hat{y}\,\sin\theta\cos\omega t + \hat{z}\,\sin\theta\sin\omega t) \tag{5.18}$$

$$\vec{B} = \hat{x}\,(B_0 + \mu_0\mu\,n\cos\theta) + \hat{y}\,\mu_0\mu\,n\sin\theta\cos\omega t \tag{5.19}$$

Plugging these two equations into Eq. 5.17 won't work because they contain counter-rotating terms. Instead we will make two changes to simplify the equations. First, we can add a term to $\vec{B}$ that is proportional to $\vec{M}$, since it will cancel out in the cross product: $\vec{M}\times(\vec{B} + a\vec{M}) = \vec{M}\times\vec{B}$. For instance, the form of $\vec{H}_m$ is a more convenient.

$$\vec{B}_{\text{eff}} = \hat{x}\,B_0 - \hat{z}\,\mu_0\mu n\sin\theta\sin\omega t$$

Second, if $|B_0| \gg |\mu_0\mu\,n|$, we expect that the precession frequency will only change slightly. In the spirit of the rotating-wave approximation, we can divide the field into components that co-rotate and counter-rotate with $\vec{M}$, and neglect the latter.

$$\begin{aligned}\vec{B}_{eff} &= \hat{x}\,B_0 - \frac{1}{2}\mu_0\mu\,n\sin\theta(\hat{y}\,\cos\omega t + \hat{z}\,\sin\omega t)\\ &\quad + \frac{1}{2}\mu_0\mu\,n\sin\theta(\hat{y}\,\cos\omega t - \hat{z}\,\sin\omega t)\\ &\Rightarrow\ \hat{x}\,B_0 - \frac{1}{2}\mu_0\mu\,n\sin\theta(\hat{y}\,\cos\omega t + \hat{z}\,\sin\omega t)\end{aligned}$$

We can use this new form to solve Eq. 5.17 with

$$-\omega = \frac{\mu}{\hbar}B_0 + \frac{\mu_0\mu n}{2\hbar}\cos\theta$$

$$\Delta\omega = \frac{\mu_0\mu n}{2\hbar}\cos\theta \tag{5.20}$$

where the minus sign of ω arises because Larmor precession is, by convention, clockwise.

Intuitive derivation of the torque The effective magnetic field applied to the atoms can be split into three components: longitudinal, rotating, and counter-rotating terms:

$$\vec{B} = \hat{x}B_{long} + (\hat{y}\cos\omega t + \hat{z}\sin\omega t)B_{rot} + (\hat{y}\cos\omega t - \hat{z}\sin\omega t)B_{crot}.$$

Each shifts the frequency by an amount proportional to the applied field, where we've switched the sign of ω to make it positive.

$$\begin{aligned}\Delta\omega_{long} &= \frac{\mu}{\hbar}B_{long}\\ \Delta\omega_{rot} &= (\text{something})\frac{\mu}{\hbar}B_{rot}\\ \Delta\omega_{crot} &= 0\end{aligned}$$

What remains is solving the prefactor of $\Delta\omega_{rot}$. As mentioned above, a field parallel to $\vec{M}$ does not affect the Larmor precession ($\vec{M}\times(\alpha\vec{M}) = 0$). So, in the particular case where $B_{rot} = B_{long}\cot\theta$ (where θ is the angle between $\vec{M}$ and the bias field), then it must be true that $\Delta\omega_{rot} = -\Delta\omega_{long}$. Therefore, the prefactor must be $-\cot\theta$.

$$\Delta\omega = \Delta\omega_{long} + \Delta\omega_{rot} = \frac{\mu}{\hbar}\left(B_{long} - B_{rot}\cot\theta\right)$$

For the field in Eq. 5.19, $B_{long} = (\mu_0\mu\, n/\hbar)\cos\theta$, $B_{rot} = B_{crot} = \frac{1}{2}(\mu_0\mu\, n/\hbar)\sin\theta$, so $\Delta\omega = \frac{1}{2}(\mu_0\mu\, n/\hbar)\cos\theta$.

Average over BEC profile

The local Larmor precession frequency $\Delta\omega$ in Eq. 5.20 varies from maximum to zero along the thinnest, z, axis of the condensate. We are specifically interested in a BEC in a harmonic trap that obeys the Thomas Fermi profile, $n(x,y,z) = n(x,y,0)(1 - z^2/R_z'^2)$, where $R_z' = \sqrt{2(c_0+c_2)n(x,y,0)/m\omega_z^2}$ is the local Thomas-Fermi radius. The Larmor frequency then varies as $\Delta\omega(z) = \Delta\omega_0(1 - z/R_z'^2)$ with $\Delta\omega_0 = \frac{1}{2}\mu_0\mu^2 n_0$ (we are dropping the dependence on x and y for now). It is tempting to simply weight the Larmor frequency by the density, but this does not give the right expression.

$$\Delta\omega_{avg} \neq \frac{\int \Delta\omega(z)\, n\, dz}{\int n\, dz}$$

Instead we needsto be average the spin projections. For short times, $\vartheta = dt\,\Delta\omega \ll 1$. We can average the components $M_y = n\cos\vartheta$ and $M_z = n\sin\vartheta$. Integrating through z,

$$\tilde{M}_z = \int \mu n(z)\, dz \left(1 - \frac{1}{2}\vartheta(z)^2\right) = \mu\tilde{n}\left[1 - \frac{1}{2}\left(\vartheta_0\sqrt{\frac{24}{35}}\right)^2\right]$$

$$\tilde{M}_y = \int \mu n(z)\, dz\, \vartheta(z)^2 = \mu\tilde{n}\frac{4}{5}\vartheta_0$$

The angle measured in the experiment, which depends on $\tilde{M}_y$, is $\theta_{\rm avg} = (4/5)\,\theta$.

$$\Delta\omega_{\rm avg} = \frac{2}{5}\mu_0\mu^2 n$$

Matching to experiment

In the experiment, we measure the averaged shift in Larmor precession frequency and look for a shift that matches the in-plane condensate density along x and y, the two weakest trap frequencies. In this analysis, we will use cyclical frequencies $f = \omega/2\pi$. After subtracting out background gradients, our model predicts a frequency shift that varies quadratically with position.

$$f(x,y) = f_0 + \frac{1}{2}f_{xx}x^2 + \frac{1}{2}f_{yy}y^2$$

As derived above, we expect the frequency shift to vary with the peak condensate density $n(x,y,0) = n_0(1-(x/R_x)^2-(y/R_y)^2)$. From Eq. 5.13, we expect

$$f = \frac{2}{5}\mu_0\mu^2 n_0\left(1 - \frac{x^2}{R_x^2} - \frac{y^2}{R_y^2}\right).$$

Matching the two expressions gives a result independent of the atom number and density.

$$f_{ii} = \frac{4}{5}\mu_0\mu^2\frac{n_0}{R_i^2} = \frac{2\mu_0\mu^2 m\omega_i^2}{5(c_0+c_2)h}$$

From the measured trap frequency $\omega_x = 2\pi \times 9.1$ Hz, we would predict $f_{xx}^{\rm theory} = 1.5\ \mu{\rm Hz}\,\mu{\rm m}^{-2}$, rather larger than the measured value of $f_{xx} = 1.1\ \mu{\rm Hz}\,\mu{\rm m}^{-2}$. However, the measured trap frequency also underestimates with the imaged Thomas-Fermi radius, predicted to be 58 μm but measured 68 μm. It is likely that the calibration of the trap frequencies was not valid during the gap experiment, or that the optical potential was anharmonic.

Alternatively, we can directly compare the slope of the gap map (Fig. 5.19) to theory. We determine the peak density of 145 $\mu{\rm m}^{-3}$ from an independent measurement of the atom number (3×10^6) and the trap frequencies. The theoretical estimate $(2/5)\mu_0\mu^2 n = h \times 2.4$ Hz is quite close to the measured value of $h \times 2.5(1)$ Hz. The gap map may provide a better estimate of the density profile than imaging or calculations of a harmonic trap.

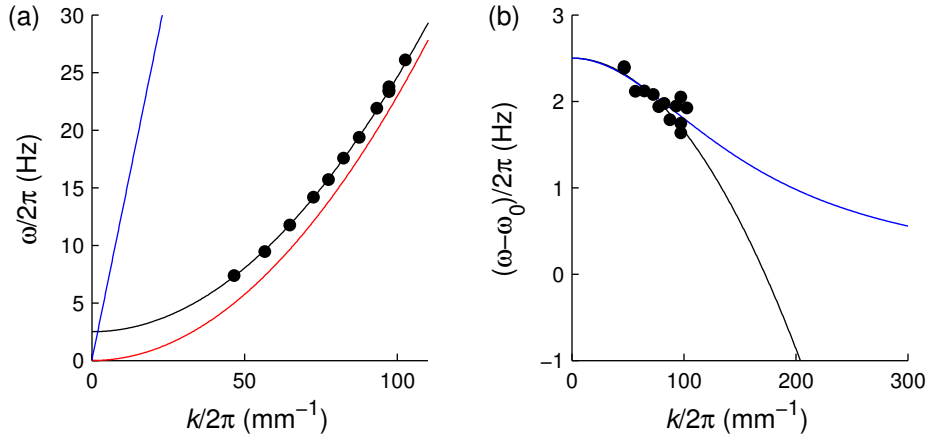

Figure 5.21: Dispersion relation with gap. (a) Fit (solid black line) to the dispersion relation data plus the measured many-body gap (black dots), for the value at the peak density of the trap. For reference, the blue line is the phonon dispersion relation at the trap center. (b) The difference between the data (black dots) and low-energy estimate (solid black line). The extrapolation crosses zero at a wavenumber of 175/mm and is most likely not real. An arbitrary theory with a momentum scale of 150/mm may suggest a more likely model.

5.4.3 Dipolar interactions: responsible for the heavy magnon mass?

When we combine the gap and dispersion relation data, we find a low-momentum dispersion relation at the center of the condensate of

$$\hbar\omega(k) = \Delta + \frac{\hbar^2 k^2}{2m^*} \tag{5.21}$$

Fig. 5.21 shows the data for the peak condensate density compared to mean-field theory with no dipolar interactions. At high momentum, Eq. 5.21 predicts that the magnon frequency will drop below the mean-field value. This extrapolation seems unlikely for two reasons. First, at very high momentum, the lower energy physics should only cause a slight perturbation to the energy. Second, when the magnon wavelength is smaller than the smallest Thomas-Fermi radius, the dipolar terms are likely to drop out. We expect that the effective mass should approach the bare mass at high energy.

From this simple reasoning, it is not surprising that the magnon mass is heavy, as the dispersion relation needs to approach the mean-field result at finite momentum. To make a rough estimate of the magnon mass, we match Eq. 5.21 to the free (no-dipole) result at $k = \pi/R_{TF}$.

$$\frac{\hbar^2}{2m}\left(\frac{\pi}{R_{TF}}\right)^2\left(1 - \frac{m}{m^*}\right) = \Delta$$

For $R_{TF} = 1.7$ μm and $\Delta = h \times 2.5$ Hz, we estimate $m^*/m = 1.01$, not bad for such a rough estimate, given that it is highly sensitive to the choice of k. A particular (and artificial) model to the data is shown in Fig. 5.21b, which uses a longer cutoff wavelength of 7 μm. We should be able to expand our understanding by pushing magnon contrast interferometry

to higher momentum, a lower dimensionality (1D), or use the $F = 2$ states where dipolar interactions are four times stronger.

5.5 Future

A key result of this chapter is that magnons have a slightly heavier mass than predicted by mean-field theory with s-wave interactions. Despite checking numerous potential sources of error, we have been so far unable to dismiss the result. Regardless, I am not completely convinced, as I always feel there remains a final crucial error to uncover. With some straightforward experimental upgrades, it should be possible to more thoroughly test this result.

If dipolar interactions are responsible for shifting the dispersion relation, the effective magnon mass may be anisotropic. In this work, we only measured the recoil frequency for wavevectors in the direction of the magnetization. Rotating the spin grating direction or magnetic bias field could help search for this effect. Moreover, performing the experiment in a 1D geometry ($\omega_x \approx \omega_y \ll \omega_z$) should also influence the form of the dispersion relation. The proportionality constant between density and gap should be different in this geometry.

As mentioned above, the extrapolation of a quadratic dispersion relation appears to be unphysical at high momentum. Improving the imaging resolution would allow for running the magnon interferometry at higher momentum, since our scheme requires resolving the oscillating spins (e.g., Ref. 70). This could also be achieved by alternative readout schemes, such as a readout spin grating pulse to map the interferometer phase on the spin populations.

The magnon contrast interferometer should be a viable technique to study other regions of the spinor phase diagram. For instance, in the polar phase, magnons are predicted to have a linear dispersion relation. This could be studied in the $F = 2$ manifold of rubidium. The technique can also be applied to probe dipolar interactions in high magnetic moment atoms or to test $SU(N)$ symmetry in alkaline earth atoms.

5.5.1 Real-time vortex tracking

While we were tracking down the rapid decay of contrast and strange patterns in Fig. 5.8, we discovered that a magnon contrast interferometer serves as a real-time vortex tracker. As discussed in Sec. 5.3.2, a short spin grating pulse initializes the interferometer by diffracting atoms into three momentum states ($q = 0, \pm k$). These diffracted atoms are also promoted to the $m_F = 0$ spin state. If the condensate phase is nonuniform, that nonuniform phase is directly mapped onto each interferometer arm. As the three momentum states shear past each other, they interfere to show the phase profile of the condensate from which they were created (Fig. 5.22a).

The local condensate phase is effectively *copied* onto interferometer states. Once we measure the density of $m_F = 0$ atoms and remove them, the original phase profile of the condensate appears to be negligibly perturbed[4]. We can then repeat the interferometer on the same condensate at a later time to observe the condensate phase evolution. We have repeated this process 20–50 times by using only a small percentage of the atoms in each

[4]Since we are imaging a topological structure, it may be robust to perturbations and heal.

interferometer pulse. Fig. 5.22b-c show trajectories of two vortices through the condensate over several seconds. The vortices are created when the condensate is cooled.

This technique shows both the handedness of the vortices and their direction of motion. If we used a 2D gas, it may be possible to observe the rate of vortex-antivortex pairs be spontaneously created and destroyed.

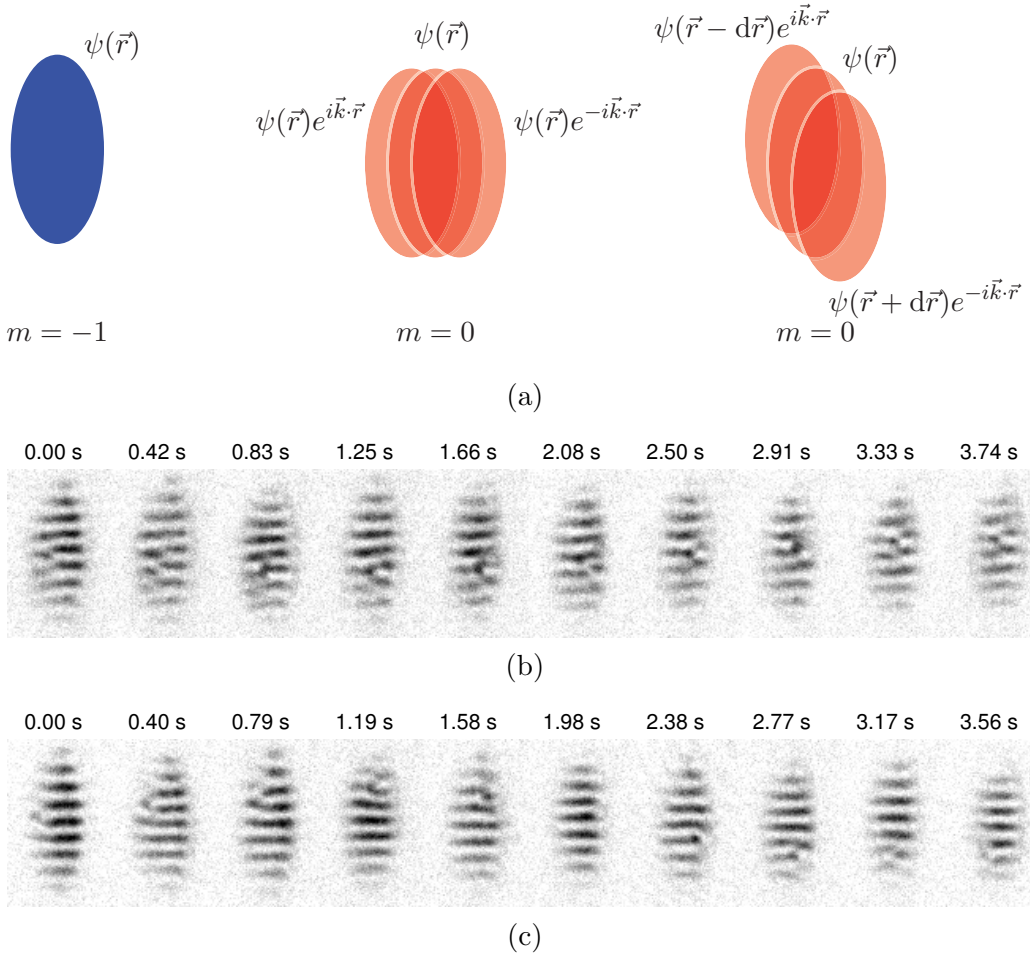

Figure 5.22: Real-time vortex tracking. (a) Scheme.The spin-polarized $m_F = -1$ is described by a scalar wavefunction $\psi(\vec{r})$, which may have a nonuniform and out-of-equilibrium phase. The initial spin grating pulse maps the wavefunction onto three momentum states with spin $m_F = 0$. Over time, the three momentum states shear past each other and interfere. We typically image after one oscillation of the magnon interferometer (time $1/(2\omega)$). (b-c) Two realizations of a scalar condensate with a vortex in the (b) middle and (c) edge. 10 images of the contrast interferometer for each condensate show a clear counterclockwise propagation of each vortex.

Appendix A

Light-atom coupling and imaging

A.1 Lorentz model of an atom

The Lorentz model of an 'electron-on-a-spring' yields surprisingly good predictions of how atoms interact with light. The model assumes that an electron is a simple-harmonic oscillator with a phenomenological resonant frequency ω_0 and damping rate Γ driven by an electric field oscillating at ω. For large detunings $|\omega - \omega_0| \gg \Gamma$, we often neglect the damping—this is the dispersive regime where refraction is most important. For simplicities' sake, let the electric field be polarized along $\hat{x}$, so all of the motion is along x. We will write the electric field as $\vec{E}(t) = \mathrm{Re}[\hat{x}\, E_0 e^{-i\omega t}]$ and only consider the real part. This looks like the *rotating wave approximation* in quantum mechanics, but is is not (we will get to that later). This is a mathematical simplification, not an approximation, so long as it is understand that $\mathrm{Re}[x]$ is the actual solution. We solve by Fourier analysis, guessing that $x = x_0 e^{-i\omega t}$ is the solution.

$$m\ddot{x} + m\Gamma\dot{x} + m\omega_0^2 x = eE_0 e^{i\omega t} \quad \Rightarrow \quad x_0 = \frac{e/m}{\omega_0^2 - \omega^2 - i\Gamma\omega} E_0$$

The solution looks like an oscillating dipole $\vec{d} = e\vec{r}$ which is proportional to the applied field.

$$ex_0 = \frac{e^2/m}{\omega_0^2 - \omega^2 - i\Gamma\omega} E_0 \quad \Rightarrow \quad \vec{d} = \alpha(\omega)\vec{E} \qquad \alpha = \frac{e^2/m}{\omega_0^2 - \omega^2 - i\Gamma\omega}$$

$\alpha(\omega)$ is the complex polarizability. For the next few sections I will simply write α and solve a few basic equations. The important thing to notice is that the solution $\vec{d} = \alpha\vec{E}$ is the same as a linearly polarizable medium in classical electromagnetism where the atom is an induced dipole.

We will solve for the absorption and emission of this dipole by two methods and equate them to solve for Γ and the cross section σ. Then we can explicity write out the above expression for α to connect the solution to the quantum mechanical equations.

A.2 Absorption and Fluorescence (Classical)

A.2.1 Scattered Power - Radiation Damping

The Larmor formula tells us that the average power radiated from an oscillating dipole is

$$\langle P\rangle = \left[\frac{1}{4\pi\epsilon_0}\right]\frac{2}{3}\frac{e^2\langle\ddot{x}^2\rangle}{c^3} = \left[\frac{1}{4\pi\epsilon_0}\right]\frac{\omega^4|\alpha|^2|\vec{E}|^2}{3c^2}.$$

I've written brackets [] around the terms that should be included in the MKS units for electromagnetism. If you leave out those terms, you get *Gaussian* or *cgs* units. The intensity of a laser is $I = [4\pi\epsilon_0]\,|\vec{E}|^2c/8\pi$. This includes a 1/2 from averaging over the volume, but not the 1/2 that we will later need in the rotating-wave approximation for quantum mechanics. We can replace the $\langle P\rangle$ with P_{sc}, the scattered power.

$$P_{sc} = \left[\frac{1}{(4\pi\epsilon_0)^2}\right]\frac{8\pi I\omega^4|\alpha|^2}{3c^4}$$

The power scattered is proportional to the intensity by a constant with units of area, the cross section σ_{sc}, $P_{sc} = I\sigma_{sc}$. Geometrically, if a laser is incident on an absorbing disk of area σ, then $I\sigma$ is the power scattered.

$$\sigma_{sc} = \left[\frac{1}{(4\pi\epsilon_0)^2}\right]\frac{8\pi\omega^4|\alpha|^2}{3c^4}$$

The decay Γ is due to light scattering, an effect known as *radiation damping*. The power loss of a simple harmonic oscillator is $P = -\langle\vec{F}\cdot\vec{v}\rangle = m\Gamma\langle\dot{x}^2\rangle$. For a simple harmonic oscillator, we can equate this to the scattered power.

$$\Gamma = \left[\frac{1}{4\pi\epsilon_0}\right]\frac{2e^2\omega^2}{3mc^3} \qquad \Gamma_0 = \left(\frac{\omega_0}{\omega}\right)^2\Gamma$$

This defines $\Gamma_0 = \Gamma(0)$, the resonant linewidth. This is the term that is usually quoted because it does not depend on the drive frequency.

As a brief aside, this is close to what you calculate in quantum mechanics. The multi-level nature of atoms makes these terms slightly more complicated. In particular, for each level j, the linewidth is

$$(\Gamma_{\mathrm{QM}})_j = f_j\Gamma_0$$

where f_j is the *oscillator strength*. The *sum rule* in quantum mechanics requires that $\sum_j f_j =$ number of electrons involved. The classical result is usually only a few percent off for the alkali atoms because $f \approx 1$ for the dipole transition.

A.2.2 Absorbed Power - Susceptibility

Above we calculate the power scattered by a dipole emitter. Now we will calculate the power absorbed by a dipole emitter. This section uses MKS units. In this context, we think of the atoms as a block of material and calculate the absorption through it. It is useful to connect this solution to the mechanics of electromagnetism. In a linear medium, we found

that the dipole moment $\vec{d} = e\vec{r}$ is induced by the electric field through the polarizability α as $\vec{d} = \alpha\vec{E}$. This can be connected to the susceptibility $\chi = \mathcal{N}\alpha/\epsilon_0$, a dimensionless number that includes the number density $\mathcal{N}$ and the complex index of refraction $n = \sqrt{1+\chi}$. In a block of material, the dipole moment is replaced by the polarization density $\vec{P} = \vec{d}\mathcal{N}$. The above definitions imply that $\vec{P}$ is induced in a material as $\vec{P} = \epsilon_0\chi\vec{E}$. These definitions link α, which describes an electron's reaction to an applied field, to the continuous parameter χ that defines the properties of a block of material.

To see how this effects light propagating through the medium, let's go back to the wave equation.

$$\nabla^2\vec{E} = \epsilon\mu\frac{d\vec{E}}{dt}$$

I have written the wave equation for a material with permittivity ϵ and permeability μ. The induced polarization density $\vec{P}$ can be taken into account by letting $\epsilon = \epsilon_0(1+\chi)$ and $\mu = \mu_0$.

By convention, the solution $\vec{E} = \hat{x}E_0e^{i(kz-\omega t)}$ propagates along $\hat{z}$ with the electric field oriented along $\hat{x}$. The equation requires that $k = \sqrt{\epsilon\mu}\,\omega$. In general, k is complex. It is easiest to understand this solution if we split k into real and imaginary components.

$$k = \frac{\omega}{c}n_{\text{index}} + ia/2 \quad \text{where} \qquad n_{\text{index}} = \text{Re}[\sqrt{1+\chi}] \qquad a = \frac{2\omega}{c}\text{Im}[\sqrt{1+\chi}]$$

Here, c is the vacuum speed of light. The solution can be rewritten

$$E = \hat{\epsilon}\,e^{i(k_0 n_{\text{index}}z-\omega t)}e^{-az/2}.$$

We call n_{index} the index of refraction and a the absorption length. The factor of 2 is so that the intensity falls off as $I = I_0e^{-az}$ for a homogeneous material or $dI/dz = -aI$ in general.

Consider one atom in a region with volume $V = Az$, where A is an area and z is the length along which the light travels. We'll make the density homogeneous to simplify the equations. Assume the absorption is small, so the numbers az, χ, and n are small. A laser of intensity I_0 and cross sectional area A is incident on this volume. The intensity $I_1 = I(z)$ after it passes the atom is slightly lower, which corresponds to an absorbed power of $P_{abs} = (I_0 - I_1)A$. The number density of one atom is $\mathcal{N} = 1/V$. Since $\chi = \alpha/(\epsilon_0 V)$, we find

$$n_{\text{index}} \approx 1 + \frac{1}{\epsilon_0 V}\text{Re}[\alpha] \qquad a = \frac{2\omega}{c}\text{Im}\sqrt{1+\frac{\alpha}{\epsilon_0 V}} \approx \frac{\omega}{c}\frac{\text{Im}[\alpha]}{2\epsilon_0 V} \tag{A.1}$$

The absorbed power is then

$$P_{abs} = (I_0 - I_1)A = I_0(1-e^{-az})A \approx I_0\frac{\omega}{c}\frac{\text{Im}[\alpha]}{\epsilon_0}$$

Notice that the volume has dropped out. We can again define the absorption cross section σ_{abs} as $P_{abs} = I_0\sigma_{abs}$.

$$\sigma_{abs} = \frac{\omega}{c\epsilon_0}\text{Im}[\alpha]$$

This expression is *not* the same as the σ_{sc}. The interpretation is straightforward: we simply put a damping rate Γ in the equation of motion but never mentioned where it came from. The critical assumption is that *all of the damping is radiative*, so $P_{abs} = P_{sc}$. We could have instead written Γ as the radiative damping given by the Larmor formula. Even though our model has two free parameters, ω and Γ, they are related through this expression.

$$\mathrm{Im}[\alpha] = \left[\frac{1}{4\pi\epsilon_0}\right]\frac{2}{3}\frac{\omega^3}{c^3}|\alpha^2|$$

which, again, can be derived by setting $P_{abs} = P_{sc}$. This expression is a special case of the optical theorem.

The solutions to the Lorentz model are as follows.

$$\begin{aligned}
\alpha &= \frac{e^2}{m}\frac{1}{\omega_0^2 - \omega^2 - i\omega\Gamma} \\
|\alpha|^2 &= \frac{e^4}{m^2}\frac{1}{(\omega_0^2-\omega^2)^2 + \omega^2\Gamma^2} \\
\mathrm{Re}[\alpha] &= \frac{e^2}{m}\frac{\omega_0^2-\omega^2}{(\omega_0^2-\omega^2)^2 + \omega^2\Gamma^2} \\
\mathrm{Im}[\alpha] &= \frac{e^2}{m}\frac{\Gamma\omega}{(\omega_0^2-\omega^2)^2 + \omega^2\Gamma^2}
\end{aligned}$$

Plugging these into the above solution, we can solve for Γ and $\sigma = \sigma_{sc} = \sigma_{abs}$. It is convenient to define the resonant cross section $\sigma_0 = \sigma(\omega_0)$.

$$\Gamma = \left[\frac{1}{4\pi\epsilon_0}\right]\frac{2}{3}\frac{e^2}{m}\frac{\omega^2}{c^3} \qquad \sigma = \frac{6\pi c^2}{\omega^2}\frac{\Gamma_0^2\omega^2}{(\omega_0^2-\omega^2)^2 + \Gamma^2\omega^2}$$

In particular, the resonant cross section $\sigma_0 = \sigma(\omega_0)$ is

$$\sigma_0 = 6\pi\frac{c^2}{\omega_0^2} = \frac{3}{2\pi}\lambda^2$$

Note that the resonant cross section is approximately the wavelength squared and is much larger than the typical electron orbit. While these formulas are identical to the ones derived in quantum mechanics by solving the Einstein A and B coefficients, it is worthwhile the emphasize that the current derivation is completely classical.

To connect these to quantum mechanics all we need to know is that a photon has energy $\hbar\omega$. The spontaneous emission rate $R(\omega) = P/(\hbar\omega)$ gives the number of photons scattered per unit time.

$$\begin{aligned}
R &= \frac{6\pi c^2 I}{\hbar\omega^2}\frac{\Gamma^2\omega^2}{(\omega_0^2-\omega^2)^2 + \Gamma^2\omega^2} \\
&= \frac{\Gamma_0}{2}\frac{I}{I_{sat}}\frac{\Gamma^2\omega_0^2}{(\omega_0^2-\omega^2)^2 + \Gamma^2\omega^2}
\end{aligned}$$

The classical treatment does not include saturation, but we can define the saturation intensity I_{sat} from this semiclassical argument.

$$I_{sat} = \frac{\hbar\omega_0\Gamma_0}{2\sigma_0}$$

The saturation intensity does require $\hbar$ and is not included in the classical theory.

A.2.3 Index of refraction and Stark Shift

From the atom's point of view, the energy of our dipole is $U = -\vec{d}\cdot\vec{E}$. Here we should be careful with our notation: $\vec{d}$ and $\vec{E}$ are phasors, so the proper way to combine them is $U = -\frac{1}{2}\mathrm{Re}[d^*E] = -\frac{1}{2}|E|^2\mathrm{Re}[\alpha]$. This energy can be positive or negative depending on the sign of $\mathrm{Re}[\alpha]$. In general, the energy is positive for $\omega > \omega_0$ (*blue-detuned*) and negative for $\omega < \omega_0$ (*red-detuned*).

$$U = -\left[\frac{1}{4\pi\epsilon_0}\right]\frac{4\pi I}{c}\mathrm{Re}[\alpha]$$

There is an intuitive way to understand whether the energy is higher or lower in the Lorentz model. When $\omega \ll \omega_0$, the electron responds in-phase with the electric field, so $\vec{d}$ points along $\vec{E}$ and the energy $-\vec{d}\cdot\vec{E}$ is lowered. However, if $\omega \gg \omega_0$, the electrons responds 180° with the drive and $\vec{d}$ points opposite $\vec{E}$, increasing the energy. Exactly on resonance, the electron is out-of-phase with the drive and $\vec{d}\cdot\vec{E}$ is zero.

For the Lorentz model,

$$U = -\left[\frac{1}{4\pi\epsilon_0}\right]\frac{4\pi I e^2}{mc}\frac{\omega_0^2-\omega^2}{(\omega_0^2-\omega^2)^2+\omega^2\Gamma^2} = -\frac{6\pi I c^2\Gamma}{\omega_0^2}\frac{\omega_0^2-\omega^2}{(\omega_0^2-\omega^2)^2+\omega^2\Gamma^2}$$

In the far-detuned limit $|\omega-\omega_0| \gg \Gamma$,

$$U = -\frac{3\pi I c^2\Gamma_0}{\omega_0^3}\left[\frac{1}{\omega_0-\omega}+\frac{1}{\omega_0+\omega}\right]$$

The second term we drop in the *rotating wave approximation*, and thus call it the *counter-rotating term*. In quantum mecanics, we often introduce the saturation intensity and again write this as

$$U = -\frac{\hbar\Gamma^2}{8}\frac{I}{I_{sat}}\left(\frac{1}{\omega_0-\omega}+\frac{1}{\omega_0+\omega}\right)$$

This is an essential feature of optical trapping. To optically trap atoms, we use lasers with an inhomogenous intensity, such as a focused laser or standing wave. If the laser is tuned to the *red* of the atom ($\omega_0 < \omega$), the potential is deepest at the points of highest intensity and can trap atoms. However, the trap is not exactly conservative. Scattering of photons from the laser will cause atoms to recoil and heat up. To minimize this, we usually use a very large detuting, $|\omega_0-\omega| \gg \Gamma_0$.

In the far-detuned limit, the scattering rate is

$$R = \left(\frac{\omega}{\omega_0}\right)^2 \frac{\Gamma^3}{8} \frac{I}{I_{sat}} \left(\frac{1}{\omega_0 - \omega} + \frac{1}{\omega_0 + \omega}\right)^2$$

$$\frac{\Gamma}{|U/\hbar|} = \Gamma \left(\frac{\omega}{\omega_0}\right)^3 \left(\frac{1}{\omega_0 - \omega} + \frac{1}{\omega_0 - \omega}\right)$$

A.2.4 Lorentz Model and the Rotating Wave Approximation

The dependence of these functions on ω are called the *Cauchy-Lorentz* or *Breit-Wigner* lineshape. In quantum mechanics we usually make the *rotating wave approximation*, where we assume that $|\omega - \omega_0| \ll \omega + \omega_0$. To simplify the notation we define the *detuning* $\delta = \omega - \omega_0$. In particular, the lineshape can be approximated as a Lorentzian.

$$\frac{\Gamma^2\omega^2}{(\omega_0^2 - \omega^2)^2 + \omega^2\Gamma^2} \approx \frac{1}{1 + [\delta/(\Gamma_0/2)]^2}$$

$$\frac{\omega_0^2 - \omega^2}{(\omega_0^2 - \omega^2)^2 + \omega^2\Gamma^2} \approx \frac{1}{\omega_0\Gamma} \frac{\delta/(\Gamma_0/2)}{1 + [\delta/(\Gamma/2)]^2}$$

We can rewrite the cross section and scattering rate as

$$\sigma = \sigma_0 \frac{1}{1 + [\delta/(\Gamma/2)]^2}$$

$$R = \frac{\Gamma}{2} \frac{I}{I_{sat}} \frac{1}{1 + [\delta/(\Gamma/2)]^2}$$

$$U = \frac{\hbar\Gamma^2}{4} \frac{I}{I_{sat}} \frac{\delta/(\Gamma/2)}{1 + [\delta/(\Gamma/2)]^2}$$

What is crucially missing the classical model is *saturation*. No matter how large the drive strength (i.e., electric field amplitude) is, the dipole will follow linearly as $\vec{d} = \alpha\vec{E}$. This is because we are dealing with a harmonic oscillator, and harmonic oscillators can have unlimited amounts of energy. If we instead consider an atom as a two-level system, a large drive strength saturates the atom, which can spend a maximum of half of the time in the excited state and thereby a maximum scattering rate of $\Gamma/2$. In order to take this into account, we add an extra term in the denominator.

$$R_{\text{two level}} = \frac{\Gamma}{2} \frac{I/I_{sat}}{1 + I/I_{sat} + [\delta/(\Gamma/2)]^2} \tag{A.2}$$

Another common approximation is the *far-detuned* or *dispersive* limit, where $\Gamma \ll |\omega_0 - \omega|$. In this limit, we can approximate

$$\frac{\Gamma^2\omega_0\omega}{(\omega_0^2 - \omega^2)^2 + \omega^2\Gamma^2} \approx \frac{\Gamma^2\omega_0\omega}{(\omega_0^2 - \omega^2)^2} = \frac{1}{(\omega_0 - \omega)^2/(\Gamma/2)^2} - \frac{1}{(\omega_0 + \omega)^2/(\Gamma/2)^2}$$

This limit is fairly uninteresting for the case of scattering but very important for refraction. This is the limit typically encountered in optical traps because a large detuning minimizes heating due to scattered light.

A.3 Absorption imaging

In absorption imaging, atoms scatters photons out of a resonant laser pulse. The wavefront is imaged onto a camera, and missing photons indicate the position of atoms. For this discussion, we will consider a resonant laser $\Delta = 0$, but allow for saturation of the atom. The decrease in intensity $I(z)$ from a dilute sample of atoms with thickness dz and cross sectional area A is attenuated by the ratio of the absorbing area to total area.

$$I(z) - I(z + dz) = I(z) N_{\text{atoms}} \frac{\sigma(I(z))}{A} = I(z)\sigma(I(z))n(z)dz$$

where $n(z)$ is the atom density and

$$\sigma(I) = \sigma_0 \frac{1}{1 + I/I_{sat}}.$$

Rewritten in differential form, we have $dI/dz = I\sigma(I)n$. For low intensities, $\sigma(I) = \sigma_0$ and we have the usual Beer-Lambert law $I = I_0 e^{-\sigma_0 n z}$. The correct form is a polylog, but the inverse problem (n given I_0 rather than I given n) is much simpler!

For thick samples, an absorption measurement probes the intensity of the light before it enters the sample, I_0, and the intensity after it passes through the sample, I_1. From this we can infer the column density $\tilde{n} = N/A$:

$$\tilde{n} = \int dz\, n(z) = -\int_{I_0}^{I_1} \frac{dI}{I} \frac{1}{\sigma(I)}$$

An atom that interacts with resonant light can be modeled very accurately as a two-level system with cross-section $\sigma(I) = \sigma_0/(1 + s)$, where $s = I/I_{sat}$, the intensity over the saturation intensity. Substituting I with sI_{sat},

$$\tilde{n} = -\int_{s_0}^{s_1} ds\, \frac{1+s}{s\sigma_0} = \frac{1}{\sigma_0} \left[\log(s_0/s_1) + (s_1 - s_0)\right]$$

The physical meaning of this formula is quite simple. At low intensities ($s \ll 1$), each atom scatters a fraction of the incident photons, and we measure the number of atoms by looking for what percentage of the photons are missing, $N \sim \log(s_0/s_1)$. At high intensities, each atom is completely saturated and scatters photons at a fixed rate $\Gamma/2$, hence the atoms scatter a fixed number of photons. We count atoms by counting the missing photons $s_0 - s_1$. Surprisingly, the crossover regime is simply the sum of the two extremes.

Our camera reads out the counts per pixel n_a in an absorption image (with atoms) and bright-field image n_b (without atoms)[1]. To find the number of atoms, we need to know the atomic cross-section σ_0, including errors due to polarization, magnetic field alignment, laser detuning and linewidth, etc., the area of each pixel sees $A = (\text{pixel size/magnification})^2$, the fraction of photons turned into electrons q (which is the camera's quantum efficiency times the optical losses *after* the atoms), the number of counts per electron g (also known as the camera gain), and the pulse length t.

[1] In addition, we need to subtract a dark-field image, which we ignore here.

$$N = \frac{A}{\sigma_0} \log \frac{n_b}{n_a} + \frac{A}{\sigma_0} \frac{I_b - I_a}{I_{sat}}$$

The light intensity at the atoms may by inferred as the number of photons $n_{a,b}/qg$ per area A times the intensity per photon $\hbar\omega/t$, where t is the pulse time. However, we do not care about the true intensity, only the intensity as compared to the saturation intensity.

$$\frac{A}{\sigma_0} \frac{I_b - I_a}{I_{sat}} = \frac{\hbar\omega}{I_{sat}\sigma_0} \frac{n_b - n_a}{qgt}$$

Note that $\sigma_0 = \hbar\omega\Gamma/2I_{sat}$.

$$N = \frac{A}{\sigma_0} \log \frac{n_b}{n_a} + \frac{2}{\Gamma tqg}(n_b - n_a) \tag{A.3}$$

These two terms provide a method of calibrating the imaging system. At low intensity, magnification, probe polarization, and magnetic field alignment contribute to a systematic error in the atom number. These do not effect the high-intensity term because, at high intensities, each atom scatters the name number of photons, regardless of polarization drifts, magnetic field alignment, laser linewidth, magnification, etc.. Instead, the chief error is in q, the overall quantum efficiency of the imaging system (g can be measured from the noise in the counts). By taking repeated images of similarly prepared samples, we can measure $(A/\sigma_0)/(2/\Gamma tqg)$. Since q can be independently measured by directly measuring the optical losses, this provides an absolute number calibration of the imaging system.

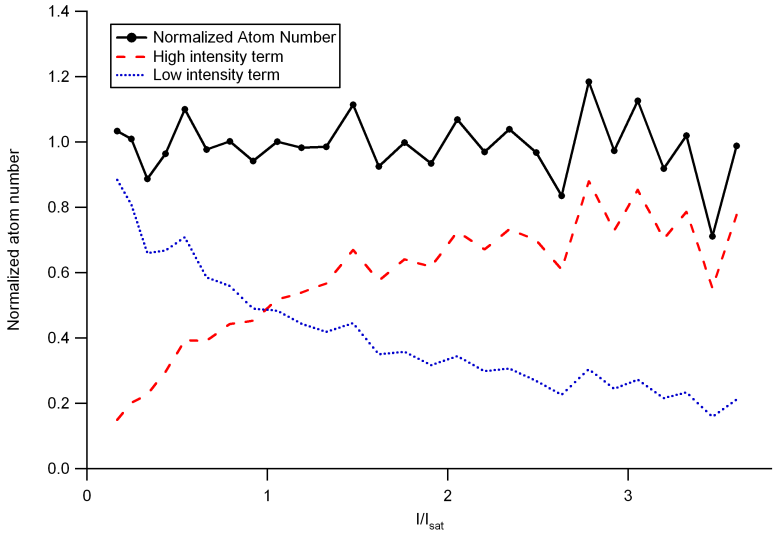

Figure A.1: Calculated number of atoms versus intensity

A.4 Noise limits in absorption imaging

For now we will summarize Eq. A.3 as:

$$N = A' \log \frac{n_b}{n_a s} + B'(n_b - n_a).$$

The optical pulses are accompanied by photon shot noise $\delta N_{\text{photon}} \geq \sqrt{N_{\text{photon}}}$, where the equality holds for photon shot noise. We will calculate the variance in atom number and assume photon shot noise.

$$\begin{aligned} \delta N^2 &= \left(\frac{\partial N}{\partial n_b}\delta n_b\right)^2 + \left(\frac{\partial N}{\partial n_a}\delta n_a\right)^2 \\ &= \left(\frac{A'}{n_b} + B'\right)^2 \delta n_b^2 + \left(\frac{A'}{n_a} + B'\right)^2 \delta n_a^2 \end{aligned}$$

The camera provides counts per pixel n, which typically show a sub-Poissonian distribution. The photons n_p arriving on the CCD are (typically) Poisson distributed, and the conversion to electrons $n_e = q_e n_p$ is binomial. Because the number of electrons (and photons) is typically very large, the electron distribution is very close to Poissonian, $(\delta n_e)^2 = n_e$. The electron conversion to counts (again, large numbers of electrons) is deterministic (plus some constant readout noise). The gain g is defined as the ratio of counts per electron, with $g < 1$.

$$\delta n^2 = \delta(g n_e)^2 = g^2 \delta n_e^2 = g^2 n_e = g n$$

$$\delta N^2 = g A'^2 \left(\frac{1}{n_b} + \frac{1}{n_a}\right) + g B'^2 (n_b + n_a) + 4 g A' B' \tag{A.4}$$

Note the important cross-term $4gA'B'$: the variance in atom number is *greater* than the sum of the variance of the low and high intensity terms because these terms are correlated. For fixed values of A and B, we can minimize the variance with respect to $n = n_b \approx n_a$.

$$0 = \frac{\partial \delta N^2}{\partial n_b} = \left(\frac{A'}{n_b} + B'\right)^2 g - 2\frac{A'}{n_b}\left(\frac{A'}{n_b} + B'\right) g \quad \Rightarrow \quad n_b = \frac{A'}{B'}$$

$$\delta N^2 \geq 8 g A' B'$$

Substituting in the original values of A' and B', we find

$$\delta N \geq \sqrt{\frac{16A}{q\sigma_0 \Gamma \tau}} \qquad I = I_{sat} \tag{A.5}$$

In addition, there is a small amount of noise from the camera read-out that increases the noise by $\delta n_{A/D}^2 = g n_{A/D} + e^2$. For our purposes (high photon counts), this noise source is negligible.

A.5 Dispersive Imaging

If the probe laser is far detuned ($|\Delta| \gg \Gamma$), the presence of atoms will phase-shift the probe ($\phi \sim \Delta^{-1}$) while only minimally attenuating the light ($R \sim \Delta^{-2}$). A strategy here is to interfere the laser that passes through the atoms with a reference laser. Typically, these two lasers are derived from the same probe, either the unscattered component of the laser (phase contrast imaging) or a different polarization (polarization contrast imaging).

Either way, the signal is typically an intensity shift linearly propotional to the phase shift and column density. Typically, the signal appears as $I = I_0(1 \pm 2\phi)$. The phase shift is $\phi = k(n_{\text{index}} - 1)z$, where we solved for the index of refraction in Eq. A.1. We are going to assume that the overall phase shift is small.

$$\phi = \int dz \, \frac{n(z)k}{\epsilon_0} \text{Re}[\alpha] = \frac{Nk}{A\epsilon_0} \text{Re}[\alpha]$$

In the Lorentz model, this simplifies to

$$\phi = N \frac{\sigma_0 \Gamma_0}{2A\Delta} \frac{1}{1 + \Gamma^2/4\Delta^2}$$

or

$$N = \frac{A}{\sigma_0} \frac{2\Delta}{\Gamma} \left(1 + \frac{\Gamma^2}{4\Delta^2}\right)$$

The last term can be neglected in the far off resonant limit.

Bibliography

[1] Gupta, S., Murch, K. W., Moore, K. L., Purdy, T. P., and Stamper Kurn, D. M. Bose-Einstein Condensation in a Circular Waveguide. *Phys. Rev. Lett.* **95**(14), 143201 (2005).

[2] Davis, K. B., Mewes, M. O., Andrews, M. R., van Druten, N. J., Durfee, D. S., Kurn, D. M., and Ketterle, W. Bose-Einstein Condensation in a Gas of Sodium Atoms. *Phys. Rev. Lett.* **75**(22), 3969 (1995).

[3] Lin, Y.-J., Perry, A. R., Compton, R. L., Spielman, I. B., and Porto, J. V. Rapid production of ^{87}Rb Bose-Einstein condensates in a combined magnetic and optical potential. *Phys. Rev. A* **79**(6), 063631 (2009).

[4] Choi, J.-Y., Kwon, W. J., Lee, M., Jeong, H., An, K., and Shin, Y.-I. Imprinting Skyrmion spin textures in spinor Bose-Einstein condensates. *New Journal of Physics* **14**(5), 053013 (2012).

[5] Guzman, J. S. *Explorations of Magnetic Phases in $F = 1$ ^{87}Rb Spinor Condensates.* Ph.D. thesis, University of California, Berkeley (2012).

[6] Watanabe, H. and Murayama, H. Unified Description of Nambu-Goldstone Bosons without Lorentz Invariance. *Phys. Rev. Lett.* **108**, 251602 (2012).

[7] Lewandowski, H., Harber, D., Whitaker, D., and Cornell, E. Simplified System for Creating a Bose-Einstein Condensate. *J. Low Temp. Phys.* **132**, 309 (2003).

[8] Fried, D. G., Killian, T. C., Willmann, L., Landhuis, D., Moss, S. C., Kleppner, D., and Greytak, T. J. Bose-Einstein Condensation of Atomic Hydrogen. *Phys. Rev. Lett.* **81**, 3811 (1998).

[9] Doret, S. C., Connolly, C. B., Ketterle, W., and Doyle, J. M. Buffer-Gas Cooled Bose-Einstein Condensate. *Phys. Rev. Lett.* **103**, 103005 (2009).

[10] Marti, G. E., Olf, R., Vogt, E., Öttl, A., and Stamper Kurn, D. M. Two-element Zeeman slower for rubidium and lithium. *Phys. Rev. A* **81**(4), 043424 (2010).

[11] Stan, C. A. and Ketterle, W. Multiple species atom source for laser-cooling experiments. *Rev. Sci. Instrum.* **76**(6), 063113 (2005).

[12] Stan, C. A. *Experiments with Interacting Bose and Fermi Gases.* Ph.D. thesis, Massachusetts Institute of Technology (2005).

[13] Günter, K. *Design and implementation of a Zeeman slower for 87Rb.* Master's thesis, Laboratoire Kastler-Brossel, Ecole Normale Superieure, Paris (2004).

[14] Guzman, J., Jo, G.-B., Wenz, A. N., Murch, K. W., Thomas, C. K., and Stamper-Kurn, D. M. Long-time-scale dynamics of spin textures in a degenerate ^{87}Rb spinor Bose gas. *Phys. Rev. A* **84**, 063625 (2011).

[15] Dushman, S. *Scientific Foundations of Vacuum Technique*, (John Wiley and Sons1962), 2nd ed.

[16] Steck, D. A. Rubidium 87 D Line Data (2008).

[17] Buck, U. and Pauly, H. Messungen des van der Waals-Potentials zwischen Alkaliatomen. *Zeitschrift fr Physik* **185**(2), 155 (1965).

[18] Croucher, D. J. and Clark, J. L. Total collision cross sections and van der Waals constants for alkali atom interactions with atoms and non-reactive diatomic molecules at thermal energies. *Journal of Physics B: Atomic and Molecular Physics* **2**(5), 603 (1969).

[19] Tiecke, T. G., Gensemer, S. D., Ludewig, A., and Walraven, J. T. M. High-flux two-dimensional magneto-optical-trap source for cold lithium atoms. *Phys. Rev. A* **80**(1), 013409 (2009).

[20] Moore, K. L. *Ultracold Atoms, Circular Waveguides, and Cavity QED with Millimeter-scale Electromagnetic Traps.* Ph.D. thesis, University of California, Berkeley (2007).

[21] Harold J. Metcalf and Peter van der Straten. *Laser Cooling and Trapping*, (Springer1999).

[22] Slowe, C., Vernac, L., and Hau, L. V. High flux source of cold rubidium atoms. *Rev. Sci. Instrum.* **76**(10), 103101 (2005).

[23] Joffe, M. A., Ketterle, W., Martin, A., and Pritchard, D. E. Transverse cooling and deflection of an atomic beam inside a Zeeman slower. *J. Opt. Soc. Am. B* **10**(12), 2257 (1993).

[24] Snadden, M. J., Clarke, R. B. M., and Riis, E. Injection-locking technique for heterodyne optical phase locking of a diode laser. *Opt. Lett.* **22**(12), 892 (1997).

[25] Bryan, G. On the Beats in the Vibrations of a Revolving Cylinder or Bell. *Proc. of Cambridge Phil. Soc. 1890* **7**, 101 (1890).

[26] Rozelle, D. M. The Hemispherical Resonator Gyro: From Wineglass to the Planets. In Alan M. Segerman, M. P. W. M. E. P., Peter C. Lai, ed., *Spaceflight mechanics*, vol. 134 of *Advances in the astronautical sciences.* American Astronautical Society, (Univelt, Inc.2009). Proceedings of the 19th AAS/AIAA Space Flight Mechanics Meeting.

[27] Ketterle, W., Durfee, D. S., and Stamper Kurn, D. M. Making, probing and understanding Bose-Einstein condensates (1999).

[28] Stringari, S. Collective Excitations of a Trapped Bose-Condensed Gas. *Phys. Rev. Lett.* **77**(12), 2360 (1996).

[29] Stringari, S. Dynamics of Bose-Einstein condensed gases in highly deformed traps. *Phys. Rev. A* **58**(3), 2385 (1998).

[30] Dalfovo, F., Giorgini, S., Pitaevskii, L. P., and Stringari, S. Theory of Bose-Einstein condensation in trapped gases. *Rev. Mod. Phys.* **71**(3), 463 (1999).

[31] Fedichev, P. O., Shlyapnikov, G. V., and Walraven, J. T. M. Damping of Low-Energy Excitations of a Trapped Bose-Einstein Condensate at Finite Temperatures. *Phys. Rev. Lett.* **80**, 2269 (1998).

[32] Cronin, A. D., Schmiedmayer, J., and Pritchard, D. E. Optics and interferometry with atoms and molecules. *Rev. Mod. Phys.* **81**(3), 1051 (2009).

[33] Gustavson, T. L., Bouyer, P., and Kasevich, M. A. Precision Rotation Measurements with an Atom Interferometer Gyroscope. *Phys. Rev. Lett.* **78**(11), 2046 (1997).

[34] Stockton, J. K., Takase, K., and Kasevich, M. A. Absolute Geodetic Rotation Measurement Using Atom Interferometry. *Phys. Rev. Lett.* **107**, 133001 (2011).

[35] Pierce, A. D. Wave equation for sound in fluids with unsteady inhomogeneous flow. *J. Acoust. Soc. Am.* **87**(6), 2292 (1990).

[36] Ho, T.-L. and Shenoy, V. B. Local Spin-Gauge Symmetry of the Bose-Einstein Condensates in Atomic Gases. *Phys. Rev. Lett.* **77**(13), 2595 (1996).

[37] Dalibard, J., Gerbier, F., Juzeliūnas, G., and Öhberg, P. *Colloquium* : Artificial gauge potentials for neutral atoms. *Rev. Mod. Phys.* **83**, 1523 (2011).

[38] Leanhardt, A. E., Görlitz, A., Chikkatur, A. P., Kielpinski, D., Shin, Y., Pritchard, D. E., and Ketterle, W. Imprinting Vortices in a Bose-Einstein Condensate using Topological Phases. *Phys. Rev. Lett.* **89**, 190403 (2002).

[39] Choi, J.-Y., Kang, S., Seo, S. W., Kwon, W. J., and Shin, Y.-i. Observation of a Geometric Hall Effect in a Spinor Bose-Einstein Condensate with a Skyrmion Spin Texture. *Phys. Rev. Lett.* **111**, 245301 (2013).

[40] Anderson, P. W. *Basic Notions Of Condensed Matter Physics*, (Westview Press / Addison-Wesley1997).

[41] Mukerjee, S., Xu, C., and Moore, J. E. Dynamical models and the phase ordering kinetics of the $s = 1$ spinor condensate. *Phys. Rev. B* **76**, 104519 (2007).

[42] Sadler, L. E., Higbie, J. M., Leslie, S. R., Vengalattore, M., and Stamper Kurn, D. M. Spontaneous symmetry breaking in a quenched ferromagnetic spinor Bose-Einstein condensate. *Nature* **443**(7109), 312 (2006).

[43] Feynman, R. P., Vernon, F. L., and Hellwarth, R. W. Geometrical Representation of the Schrdinger Equation for Solving Maser Problems. *J. Appl. Phys.* **28**(1), 49 (1957).

[44] Sakurai, J. J. *Modern quantum mechanics.*, (Addison-Wesley1994), Revised ed.

[45] Freilich, D. V., Bianchi, D. M., Kaufman, A. M., Langin, T. K., and Hall, D. S. Real-Time Dynamics of Single Vortex Lines and Vortex Dipoles in a Bose-Einstein Condensate. *Science* **329**(5996), 1182 (2010).

[46] Reinaudi, G., Lahaye, T., Wang, Z., and Guéry Odelin, D. Strong saturation absorption imaging of dense clouds of ultracold atoms. *Opt. Lett.* **32**(21), 3143 (2007).

[47] Stamper Kurn, D. M. *Peeking and Poking at a new quantum fluid: Studies of gaseous Bose-Einstein condensates in magnetic and optical traps.* Ph.D. thesis, Massachusetts Institute of Technology (2000).

[48] Higbie, J. M. *First Steps toward Precision Measurements using Multicomponent Bose-Einstein Condensates of* ^{87}*Rb.* Ph.D. thesis, University of California, Berkeley (2005).

[49] Girvin, S. M. The Quantum Hall Effect: Novel Excitations And Broken Symmetries. In *Topological aspects of low dimensional systems* (1999).

[50] Van Oosterom, A. and Strackee, J. The Solid Angle of a Plane Triangle. *Biomedical Engineering, IEEE Transactions on* **BME-30**(2), 125 (1983).

[51] Arora, B., Safronova, M. S., and Clark, C. W. Tune-out wavelengths of alkali-metal atoms and their applications. *Phys. Rev. A* **84**, 043401 (2011).

[52] Vengalattore, M., Higbie, J. M., Leslie, S. R., Guzman, J., Sadler, L. E., and Stamper-Kurn, D. M. High-Resolution Magnetometry with a Spinor Bose-Einstein Condensate. *Phys. Rev. Lett.* **98**(20), 200801 (2007).

[53] Lauter, H. J., Godfrin, H., Frank, V. L. P., and Leiderer, P. Ripplons in ^{4}He films observed by neutron scattering. *Phys. Rev. Lett.* **68**, 2484 (1992).

[54] Mazets, I. E. Waves on an interface between two phase-separated Bose-Einstein condensates. *Phys. Rev. A* **65**, 033618 (2002).

[55] Watanabe, H. and Murayama, H. Nambu-Goldstone bosons with fractional-power dispersion relations. *Phys. Rev. D* **89**, 101701 (2014).

[56] Mukerjee, S., Xu, C., and Moore, J. E. Topological Defects and the Superfluid Transition of the $s = 1$ Spinor Condensate in Two Dimensions. *Phys. Rev. Lett.* **97**, 120406 (2006).

[57] Stamper Kurn, D. M. and Ueda, M. Spinor Bose gases: Symmetries, magnetism, and quantum dynamics. *Rev. Mod. Phys.* **85**, 1191 (2013).

[58] Ho, T.-L. Spinor Bose Condensates in Optical Traps. *Phys. Rev. Lett.* **81**, 742 (1998).

[59] Ohmi, T. and Machida, K. Bose-Einstein Condensation with Internal Degrees of Freedom in Alkali Atom Gases. *J. Phys. Soc. Jpn.* **67**(6), 1822 (1998).

[60] Phuc, N. T., Kawaguchi, Y., and Ueda, M. Beliaev theory of spinor BoseEinstein condensates. *Annals of Physics* **328**(0), 158 (2013).

[61] Bouchendira, R., Cladé, P., Guellati Khélifa, S., Nez, F., and Biraben, F. New Determination of the Fine Structure Constant and Test of the Quantum Electrodynamics. *Phys. Rev. Lett.* **106**, 080801 (2011).

[62] McPeake, D. *Superfluidity, collective excitations and nonlinear dynamics of Bose-Einstein condensates*. Ph.D. thesis, Queen's University Belfast (2002).

[63] Jin, D. S., Matthews, M. R., Ensher, J. R., Wieman, C. E., and Cornell, E. A. Temperature-Dependent Damping and Frequency Shifts in Collective Excitations of a Dilute Bose-Einstein Condensate. *Phys. Rev. Lett.* **78**, 764 (1997).

[64] Stamper Kurn, D. M., Miesner, H.-J., Inouye, S., Andrews, M. R., and Ketterle, W. Collisionless and Hydrodynamic Excitations of a Bose-Einstein Condensate. *Phys. Rev. Lett.* **81**, 500 (1998).

[65] Watanabe, H., Brauner, T., and Murayama, H. Massive Nambu-Goldstone Bosons. *Phys. Rev. Lett.* **111**, 021601 (2013).

[66] Eto, Y., Saito, H., and Hirano, T. Observation of Dipole-Induced Spin Texture in an ^{87}Rb Bose-Einstein Condensate. *Phys. Rev. Lett.* **112**, 185301 (2014).

[67] Kawaguchi, Y., Saito, H., and Ueda, M. Can Spinor Dipolar Effects Be Observed in Bose-Einstein Condensates? *Phys. Rev. Lett.* **98**, 110406 (2007).

[68] Vengalattore, M., Leslie, S. R., Guzman, J., and Stamper Kurn, D. M. Spontaneously Modulated Spin Textures in a Dipolar Spinor Bose-Einstein Condensate. *Phys. Rev. Lett.* **100**, 170403 (2008).

[69] Panofsky, W. K. and Phillips, M. *Classical electricity and magnetism*, (Addison-Wesley1962).

[70] Shammass, I., Rinott, S., Berkovitz, A., Schley, R., and Steinhauer, J. Phonon Dispersion Relation of an Atomic Bose-Einstein Condensate. *Phys. Rev. Lett.* **109**, 195301 (2012).